Theoretical and Experimental Studies on Some Oxide Based Dilute Magnetic Semiconductors

Thesis

Submitted by

HARI SHANKAR KAUSHIK

(Registration No. YMCAUST/PH02/2011)

Under the Guidance of

Dr. ANURADHA SHARMA
Supervisor
Associate Professor
Department of Physics
J.C. Bose University of Science
& Technology, Faridabad

Dr. MAMTA SHARMA
Co-Supervisor
Assistant Professor
Department of Materials &
Metallurgical Engineering
PEC Chandigarh

Submitted in fulfilment of the requirement of the degree of

DOCTOR OF PHILOSOPHY

To

Department of Physics
J.C. Bose University of Science & Technology, YMCA, Faridabad

DECLARATION

I hereby declare that this thesis entitled **Theoretical and Experimental Studies on Some Oxide based Dilute Magnetic Semiconductor** by **HARI SHANKAR KAUSHIK,** submitted in fulfilment of the requirement for the Degree of Doctor of Philosophy in **DEPARTMENT OF PHYSICS** of J.C. BOSE University of Science & Technology, YMCA Faridabad, during the academic year 2019-2020, is a bonafide record of my original assigned work carried out supervision of Dr. Anuradha Sharma, Associate Professor, Department of Physics, J.C. Bose University of Science & Technology, Faridabad & Mamta Sharma, Assistant Professor, Department of Materials & Metallurgical Engineering, PEC Chandigarh & it has not been presented elsewhere.

I further declare that to the best of my knowledge, the thesis does not contain any part of any work which has been submitted for the award of any degree either in this university or in any other university.

HARISHANKAR KAUSHIK
(Registration No. YMCAUST/PH02/2011)

CERTIFICATE BY SUPERVISORS

This is to certify that this thesis entitled **Theoretical and Experimental Studies on Some Oxide based Dilute Magnetic Semiconductor** by **HARI SHANKAR KAUSHIK,** submitted in fulfilment of the requirement for the Degree of Doctor of Philosophy in **DEPARTMENT OF PHYSICS** of J.C. BOSE University of Science & Technology, YMCA Faridabad, during the academic year 2019-2020, is a bonafide record of work carried out under my guidance and supervision.

We further declare that to the best of my knowledge, the thesis does not contain any part of any work which has been submitted for the award of any degree either in this university or in any other university.

Dr. ANURADHA SHARMA

Supervisor
Assistant Professor (Physics)
Department of Humanities &
Applied Sciences
YMCA University of Science
& Technology Faridabad

Dr. MAMTA SHARMA

Co-Supervisor
Assistant Professor
Department of Materials &
Metallurgical Engineering
PEC Chandigarh

ACKNOWELGMENTS

It is my extreme pleasure to acknowledge those peoples who helped and supported me in many ways during my entire Ph.D. research work. Hence first of all, I would like to convey my sincere thanks to my supervisor Dr. Anuradha Sharma & co-supervisor Mamta Sharma for giving me a chance to work under their guidance. I am extremely grateful and also indebted to my supervisor & co-supervisor, as this thesis could not have completed without their constant encouragement, help, support and active guidance.

I sincerely acknowledge the support from Director of university, other faculty members, staffs and technical assistants of Department of Physics, J.C. Bose University of Science & Technology (Erstwhile YMCA University), YMCA Faridabad during entire course of my research work.

Finally, I love to express to my gratitude to my family members. It is all for their constant support, encouragement, to fulfill my aim and to step forward.

ABSTRACT

Oxide based dilute magnetic semiconductors are also the prime candidates for various multifunctional applications such as in transparent electronics, UV light emission, gas sensing, varistors and surface acoustic wave (SAW) devices etc. Oxide based dilute magnetic semiconductors can be used to in various spintronic devices such as magnetic FETs or low threshold spin-lasers etc. The main objective of present investigation was to study theoretical aspects of dilute magnetic semiconductors and perform experimental studies on and transition metal (Mn and In) doped oxide based DMS (ZnO). In theoretical study, various mechanisms for understanding origin of ferromagnetism in dilute magnetic semiconductors were studied & relationship between magnetization, curie temperature, doping & carrier concentration for TM doped DMS was simulated. Further mechanism of ferromagnetism in Mn doped zinc oxide was studied for exploring room temperature ferromagnetism. Subsequently a theoretical study on optically induced ferromagnetism in DMS was performed for understanding effects of optical radiation on TM doped DMS.

As a part of experimental study, transition metal (Indium & Magnanese) doped zinc oxide thin films synthesized using sol-gel method. The thin films were subjected to structural, electrical, optical & magnetic characterization using XRD, SEM, UV-Visible spectroscopy & SQUID techniques.

The Indium-doped ZnO thin films having different doping concentrations were synthesized for transparent conducting oxide applications and their electrical, structural & optical properties were studied. The full width half maximum (FWHM) observations from XRD spectra revealed deterioration of crystallinity at higher doping concentrations (>5%). But the thin films show a very good transmittance within the visible wavelength region which suggests that In doped ZnO thin films can be very good candidates for transparent conducting oxides

Subsequently the Mn doped ZnO thin films were synthesized for spintronic & optical applications. The XRD patterns reveal good quality with minor deviation from pure ZnO films. The samples shows gradually increase in in transmittance in visible region. Also the optical transmittance of samples increases with doping concentrations. The magnetic measurements revealed possibility of room temperature ferromagnetism in Mn doped ZnO thin films.

Keywords : Dilute Magnetic Semiconductor, ZnO, sol-gel, Ferromagnetism, Indium, Manganese

Table of Contents

1. INTRODUCTION

1.1. Background of Dilute Magnetic Semiconductors

The field of magnetism has fascinated humans over a span of several centuries. It started with the observation of the attraction of lodestone to a piece of iron. Since then mankind has come a long way to understand magnetism as one of the quantum mechanical phenomena and also to control and commercialize the processes to produce state of the art devices like hard disks and magnetic random access memories which are based on metallic multilayers.

Presently, magnetic devices utilize only the spin degree of freedom of the electrons to bring about these functionalities. Conventional electronics utilizes only the charge degree of freedom of the carrier. Recently, a new field named *Spintronics* [1] has emerged wherein it is envisioned that novel functional devices can be fabricated if the charge as well as the spin degrees of freedom can be combined. It is envisaged that such a technology will give rise to devices which have improved efficiency and less power consumption. Some devices that have been conceptualized are Spin LEDs, Spin FETs, Spin valves, magnetic recorders (based on Giant Magnetoresistance effect), Non-volatile memories and many ultra-low power devices [2]. Futuristic developments include using ferromagnetic contacts to inject spin polarized electrons into semiconductors and bring about GMR effects. The development of such devices also promises to reduce the fabrication cost as it would mean combining two different steps in one.

One of the ingenious ways to combine the spin and charge of the carriers in a material and achieve these effects, is by synthesizing a material with both semiconducting as well as magnetic properties. Since, conventionally used semiconductors such as Si and GaAs are diamagnetic and possess a very small g-factor (measure of the interaction strength with an applied magnetic field), there must be a way to integrate the semiconducting and magnetic property by some other means. These were the ideas that prompted the evolution of a new class of materials known as “Dilute Magnetic Semiconductors” (or DMS, in short), where a fraction of a host semiconductor material’s atoms is substituted by ferromagnetic atoms. Typically, use of magnetic metal contacts to make GMR devices has resulted in poor efficiency due to conductivity mismatch and lattice mismatch that exists at the interface of metal / insulator or metal / semiconductor junction. Development of

DMS materials can help reduce both of these deleterious effects if one can realize spin polarized current injection using DMS materials.[3]

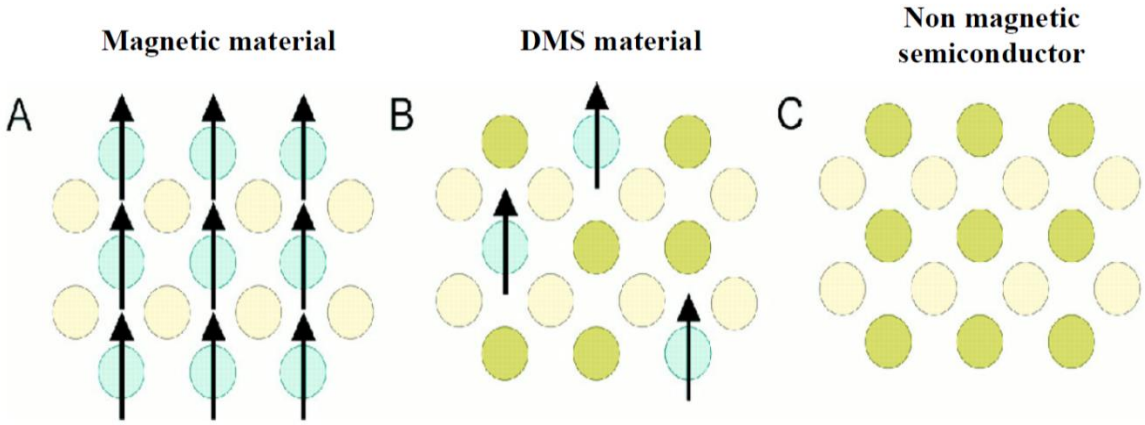

Figure 1-1: Dilute Magnetic Semiconductors

The most studied system in this area was the compound semiconductor systems doped with transition metal ions. The interest in the field started with the possibilities to probe many interesting properties, such as the ability to control lattice parameter, band gap and electrical properties. In addition, the magnetic properties which stem from the random presence of d-ions for the substituted cations, gives rise to new effects which manifest in terms of magneto-transport and magneto-optical properties. The field has progressed since then, to presently include many more compound semiconductors to date. Some widely studied systems are GaAs, GaN and ZnO doped with various transition elements.

Simultaneously, interest started to evolve in the areas of thin film DMS materials with the realization that any device application would require epitaxial thin films. It was demonstrated then InAs/GaAs could also be used to make a DMS material. This was very important then because GaAs was already widely being used for fabricating semiconductor lasers, compact discs and microwave transistors. More recently, there have been works in new materials such as wideband gap nitrides and oxides. Particular interest exists in the area of transition metal doped GaN and oxide semiconductors (for example, ZnO, TiO_2, SnO_2, etc.) can be the promising candidate to have Curie temperatures well above room temperatures.

1.2. Oxide Based Dilute Magnetic Semiconductors

Unlike the non-oxide semiconductors, oxide semiconductors are generally known to have wide energy band-gap which is greater than 3.0 eV. Having blessed with such large semiconducting band-gap, they are optically transparent in the visible region and suitable for short wavelength light applications. The most common examples of such oxide semiconductors are ZnO, TiO_2, SnO_2, In_2O_3 etc. The DMS which are derived from oxide based semiconductors, have following advantages;

(1) wide bandgap makes them suited for applications with short wavelength light,
(2) transparency and dye-ability with pigments,
(3) high *n*-type carrier concentration,
(4) capability to be grown at low temperature even on plastic substrate,
(5) ecological safety and durability,
(6) low cost, etc.

Oxide based dilute magnetic semiconductors are also the prime candidates for various multifunctional applications such as in transparent electronics, UV light emission, gas sensing, varistors and surface acoustic wave (SAW) devices and after adding the spin functionality, they can be used to produce magnetic FETs [4] or low threshold spin-lasers [5]. Some of the most popular oxide based semiconductors are as follow.

1.2.1 Zinc Oxide

ZnO belongs to category of group II–VI semiconductors and it is a very potential candidate for many electronic devices due to its wide range of useful properties. Zinco Oxide (ZnO) is compound semiconductor having very wide optical band-gap (>3.3 eV) , which enables some applications in optoelectronics such as light-emitting diodes, laser diodes and photodetectors. ZnO can also be used for sensors, transducers and actuators. In addition, it is a biocompatible and bio-safe. Moreover, TM-doped ZnO useful for spintronic applications due to intrinsic donor defects which contributes in enhanced optical & ferromagnetic properties at room temperature [6]. Some physical parameters of Zinc oxide semiconductor have been listed in table-1.

Crystal structure and chemical binding

ZnO is one of the compound semiconductors which have their ionicity lying between covalent and ionic semiconductor. The zinc oxide crystallizes in form of hexagonal wurtzite (B4), zinc blende (B3), and rocksalt (B1) crystal structures. However, under ambient conditions, the thermodynamically stable phase is the wurtzite. ZnO crystallizes usually in the hexagonal wurtzite-type structure shown in Figure 1.2. In this phase, the ZnO has a polar hexagonal axis called the c-axis that is parallel to the z-axis. The basic translation vectors a and b have equal length and lie in x-y plane and makes 120°angle with each other and the translation vector c is parallel to the z-axis [3]. The wurtzite structure of ZnO has a hexagonal unit cell in lattice with

$$a = b \approx 0.3249 \text{ nm}$$

$$c \approx 0.5206 \text{ nm}$$

The ratio c/a value for ZnO wurtzite structure is around 1.602, which is slightly different from the ideal value of c/a = 1.633 for hexagonal structure. Every Zn^{2+} ion (cation) is surrounded by four O^{2-} ions (anions) and each O^{2-} ions is surrounded by four Zn^{2+} ios. The lattice structure is formed by arrangment of alternating planes of Zn^{2+} ions (tetrahedrally surrounded by O^{2}) stacking along the *c-axis*, due to it lacks of symmetry. The unit cell surfaces can have either Zn^{2+} or O^{2-} ions, caused ZnO lattice to have positive or negative charges on the surfaces [7].

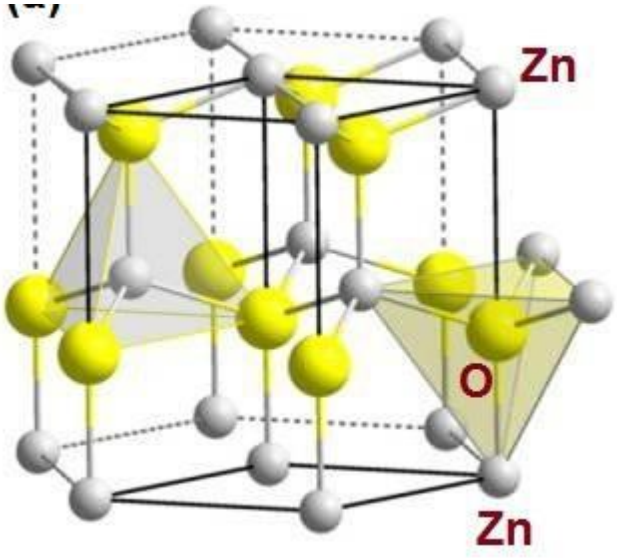

Figure 1-2 : Crystal Structure of ZnO

Table 1 : Some basic physical parameters for wurtzite ZnO.

Parameter	**Value**
Density	5.606 g/cm^3
Stable phase at 300 K	Wurtzite
Melting point	2248 K
Linear expansion coefficient (/C)	a_0: 6.5×10^{-6}
	c_0:3.9 x 10^{-6}
Static dielectric constant	8.656
Refractive index	2.008, 2.029
Energy gap (300 K)	3.37 eV (direct band gap)
Intrinsic carrier concentration	<10^6 cm^{-3}
Ionicity	62%

1.2.2 Tin Oxide (SnO2)

Like ZnO, tin (IV) or stannic oxide (SnO2) is another very important wide band transparent oxide semiconductor and possess special properties, such as transparency, remarkable chemical and thermal stabilities, with direct application for photodetectors, catalysts for oxidation and hydrogenations, solar cells, semiconducting gas sensors, liquid crystal displays and protective coatings. In the bulk, SnO2 has a direct optical energy band gap of the order of 3.67 eV at 300 K. As a mineral, stannic oxide is also called Cassiterite which has a rutile crystal structure. The rutile structure has a tetragonal unit cell, as shown in Fig. 1-3. The lattice constants are a = b = 4.7374 Å and c = 3.1864 Å [8]. In the bulk, all Sn atoms are six-fold coordinated to three-fold coordinated oxygen atoms.

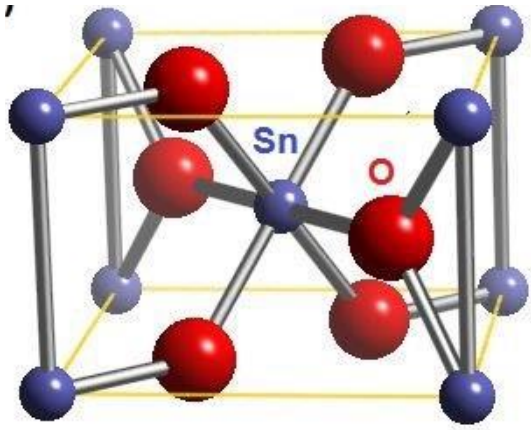

Figure 1-3 : Crystal Structure of Tin Oxide (SnO2)

1.2.3 Titanium dioxide (TiO2)

Titanium dioxide (TiO2) is also belongs to the groups of wide-band oxide semiconductors and widely used as photocatalyst under UV-light. It crystallizes in several forms, such as rutile, anatase and brookite (see the diagrams of the most stable phases in Fig. 1.4). Rutile structure has a tetragonal unit cell (a = 4.59 Å and c = 2.96 Å) with a bandgap of 3 eV while the anatase phase also crystallizes in a tetragonal structure (a = 3.78 Å and c = 9.52 Å) with a bandgap of 3.2 eV. The brookite has orthorhombic structure with lattice parameters a = 5.4558 Å, b = 9.1819 Å and c = 5.1429 Å and is rare compared to anatase and rutile. Brookite has a larger cell volume than either anatase or rutile, with 8 TiO_2 groups per unit cell, compared with 4 for anatase and 2 for rutile.[9]

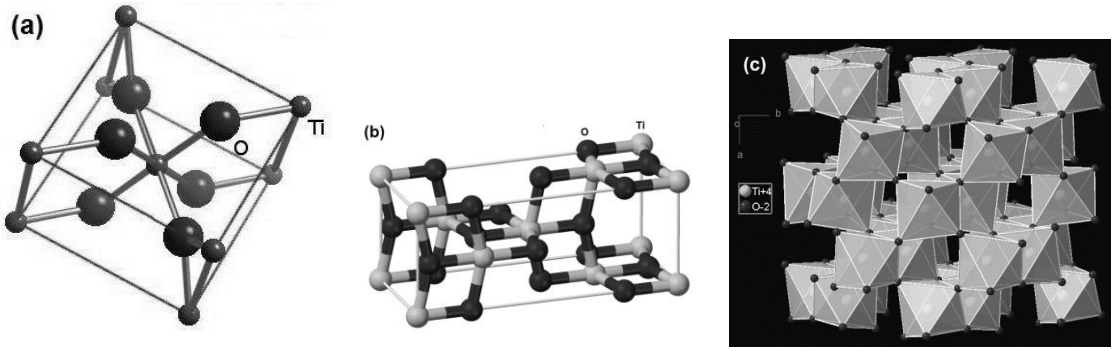

Figure 1-4: Crystal Structure of Titanium Oxide

1.3. Problem Statement

Since from the last decade, the search for oxide based DMS with high curie temperature has been continued even up to still now, for the development of new class of semiconducting electronics or spin-based electronics. In this regard, the presence or absence of intrinsic ferromagnetism in TM-doped wide band oxides has become a debatable issue; which should be overcome through a series of systematic and careful study. Our motivation is to investigate the origin of magnetism in TM - doped wide band transparent oxide semiconductors & studying their magnetic, optical, structural & electrical properties. Zinc oxide has been very popular among oxide based DMS because of it's large bandgap & high solubility for TM ions.

Although many researchers have predicted room temperature ferromagnetism in TM doped ZnO but experimental observations are still contradicting. Our study presents technique for preparing ZnO thin films & doping of TM ions such as (Mn, Co, In etc.) and experimental measurement & analysis of the samples.

1.4. Study Objectives

The prime objectives of this thesis are as follows:

- To Study origin of ferromagnetism in Transition metal ion doped Dilute magnetic semiconductors (DMS) & relationship between curie temperature & carrier/doping concentration
- To Study effects of optical radiation on Dilute magnetic semiconductors (optically induced ferromagnetism) in DMS
- To prepare Transition Metal (Mn /In) doped ZnO thin fims using sol-gel method
- To determine & analyze effects of variations of doping concentration on structural, morphological, optical, electrical and magnetic properties of Indium & manganese doped ZnO thin films
- Exploration of prepared nanostructures for various technological applications.

1.5. Plan of Thesis

The thesis is composed of six chapters and organized as follows:

Chapter 1 gives the general introduction about Dilute Magnetic Semiconductors & oxide based dilute magnetic semiconductors. It gives brief description about the problem statement & study objectives.

Chapter 2 describes the fundamentals of magnetism & theories for origin of ferromagnetism in DMS. This chapter also provides introduction about various magnetic interactions which are responsible for ferromagnetism & theoretical models describing magnetic behavior of Transition metal doped DMS.

Chapter 3 provides a brief review of structural, magnetic, electrical & optical properties of Transition metal doped DMS system. This chapter also provides details of general theoretical study, simulation & analysis of relationship between curie temperature & doping/carrier concentrations in TM doped DMS & further this study is extended to Mn doped ZnO system. Subsequently study on optically induced ferromagnetism is also presented in this chapter.

Chapter 4 describes various experimental techniques for synthesis of TM doped DMS thin films, process of selecting candidate materials & suitable technique for growing TM (Mn/In) doped ZnO thin films. This chapter also provide brief explanation of the working principles of structural the characterization techniques such as X-Ray Diffraction (XRD), Scanning Electron Microscope (SEM), Transmission Electron Microscopy (TEM) etc; optical characterization techniques such as Ultraviolet-visible (UV-vis) spectroscopy, Photoluminescence (PL) spectroscopy etc. and magnetic characterization techniques such as Vibrating Sample Magnetometer (VSM) and Superconducting Quantum Interference Devices (SQUID) used for the analysis of samples.

Chapter 5 describes details of procedure for synthesizing Indium doped ZnO thin films for transparent electronics applications. This chapter also presents results & analysis of structural electrical & optical properties of the samples with different doping concentrations.

Chapter 6 describes details of procedure for synthesizing Manganese (Mn) doped ZnO thin films. This chapter also presents results & analysis of structural electrical & optical properties of the samples with different doping concentrations.

Chapter 7 concludes the research work

2. LITEATURE REVIEW OF TRANSITION METAL DOPED DMS

2.1. Origin of Magnetism

Magnetic fields are created by the movement of charge through space. In atoms, it is the movement of electrons that produce the magnetic fields. The strength of the magnetic field produced is known as magnetic moment (μ). Magnetic moments are associated with both the spin (s) and orbital (l) angular momentum of each electron. The magnetic moment of an individual electron is the Bohr magneton given by Equation (2.1).

$$\mu_B = \frac{eh}{2\pi m_e} \quad (2\text{-}1)$$

Where

e is the charge of the electron;

h is the Planck constant, and

m_e is the mass of an electron.

According to Pauli exclusion principle; pair of electrons within an atom can never have the same quantum numbers. A direct consequence of this is that paired electrons must have opposite spins. Hund's rule states that before any two electrons occupy an orbital in a subshell, other orbitals in the same subshell must first each contain one electron. Also, the electrons filling a subshell will have parallel spin before the shell starts filling up with the opposite spin electrons. This means that the net magnetic moment of a fully filled electron shell is zero, and thus only partially filled orbitals can contribute towards a net magnetic moment. The exchange energy removes the degeneracy of the spin-up and spin-down half bands (Figure 2.1), creating an imbalance of spins and thereby allowing for a net magnetic moment. The larger the exchange energy the greater is the energy difference between the two half bands. As can be seen in the figure, electrons fill up the band by occupying the lowest energy states available. In cases of a smaller exchange energy (Figure 2.1a), there will be some degeneracy of the energy of the available spin states. Typically, this will result in a non-integral number of magnetic moments per atom. Where there is a large exchange energy

(Figure 2.1b), complete separation between the half-bands will result in an integral number of magnetic moments per atom

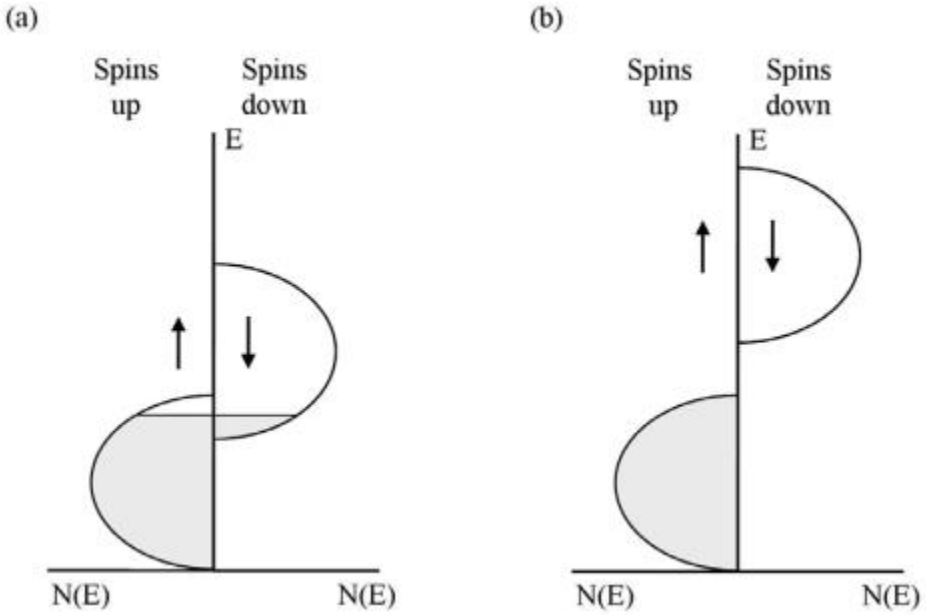

Figure 2-1 : Density of States showing exchange splitting of spin-up and spin-down half bands for (a) small exchange splitting, (b) larger exchange splitting

In solids the overall magnetic moment consists almost entirely of that contributed by electron spin. This phenomenon is called the quenching of the orbital moment. It occurs because the electron orbitals are fixed in the crystal lattice, and cannot change their orientation when a magnetic field is applied. In practice it will be sufficient to regard the magnetic moment of solids as being due to the spin only. Thus, most of the time the terms spin and magnetic moment can be used interchangeably. However, it should be noted that in rare earth atoms and ions the orbital moment is not quenched, even in crystalline solids. This is due to the 4f electrons being more effectively shielded by the outer electrons than the 3d electrons are in transition metals [10]. When a material consisting of several atoms is subjected to an applied magnetic field (H), the net magnetic moment per unit volume of the material is defines as the magnetization (M). The response of a material upon application of a magnetic field is known as magnetic induction or magnetic flux density (B). Inside a magnetic material, the relationship between B and H due to the magnetization is given by Equation (2.2).

$$B = \mu_0(H + M) \tag{2-2}$$

One of the most important properties of magnetic materials is susceptibility (χ) which is the degree of magnetization induced in a material per unit applied magnetic field. It is given by Equation (2.3).

$$\chi = M/H \tag{2-3}$$

2.1.1. Classes of Materials

Materials are divided into different classes of magnetism based on how the atoms interact collectively. These classes are discussed in this section and depicted schematically in Figure 2.2.

Diamagnetism

The magnetic response of the materials belonging to this category is opposite in direction to the external magnetic field. There are no unpaired electrons in outer orbits of atoms/molecules of such materials and hence their net magnetic moment is zero. The susceptibility of diamagnetic materials have negative sign which can be explained with the help of Lenz's law which states that "the direction of induced magnetic moment is opposite to an applied external magnetic field [11]. The response signal of diamagnetic materials is independent of temperature. The moment vs. magnetic field graphs of these materials represented by a straight line with a negative slope (Figure 2.2a).

Paramagnetism

The Paramagnetic behavior is possessed by the materials whose atoms/molecules have unpaired electrons in the outer orbits which leads to some net non-zero moments. But for bulk material, the moments are aligned in random directions and cancel out each other which results in zero magnetization. However, when an external magnetic field is applied, the moments align with the direction of the magnetic field & leading to net non-zero magnetic moment

The susceptibility for paramagnetic materials can be given by Curies-Weiss law in Equation (2.4).

$$\chi = \frac{N\mu_0 m^2}{3K_B T} \tag{2-4}$$

where μ_0 is the magnetic permeability , N is number of dipoles per unit volume, T is temperature & K_B is Boltzmann's constant.[10,11]

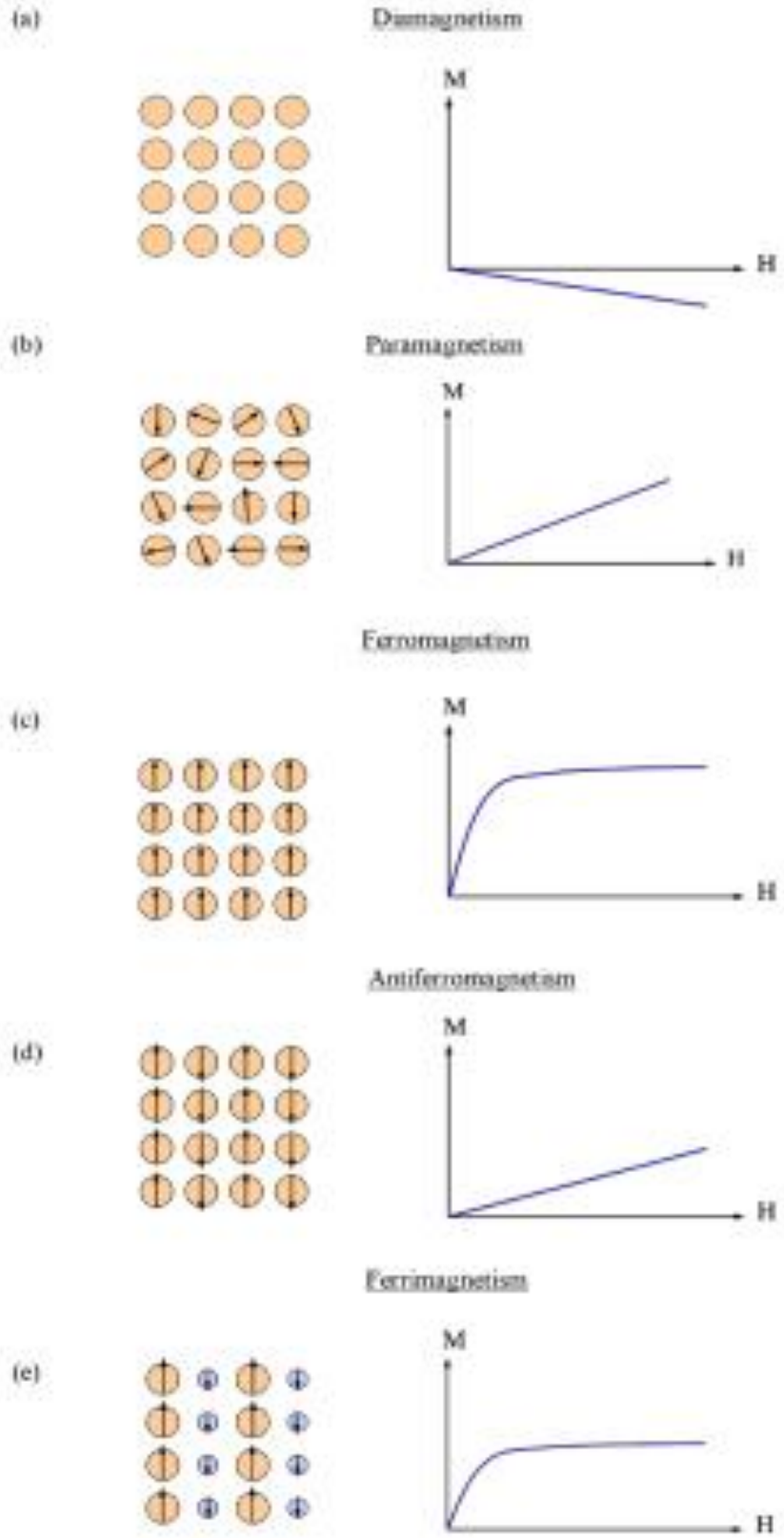

Figure 2-2: Atom/Molecular spins and M vs H Graph for (a) diamagnetic, (b) paramagnetic, (c) ferromagnetic, (d) anti-ferromagnetic and (e) ferromagnetic materials

Because of the approximation used in the Curie-Weiss law, it can be used for explaining magnetic behavior of the materials having low magnetization strengths. The magnetic susceptibility of paramagnetic materials is very small (~10^{-4}). The moment vs. magnetic field graphs of these materials represented by a straight line with a positive slope (Figure 2.2b). The strength of magnetization decreases with temperature which may be due to the more random thermal mis-alignment of the magnetic domains.

The most common form of paramagnetic behaviour includes Pauli and Van-Vleck paramagnetism. Metals which are having large concentrations of electrons exhibits Pauli behavior. Whereas Van-Vleck behaviour is observed in materials having even number of unpaired electrons. The susceptibility in Van-Vleck materials is independent of temperature, unlike other forms of paramagnetism.

Ferromagnetism

The materials having unpaired electrons exhibits ferromagnetism. The unpaired electrons cause the material to have a net magnetic moment. When an external field is applied to such, the electron spins aligns in the direction of the external magnetic field. These spins remain aligned even after removal of the magnetic field as shown in Figure 2.2c. The alignment is not disturbed even due to the effect of thermal agitation (KT). The electron spins interact with each other through various exchange mechanisms in an energetically favorable way. These interactions may occur through itinerant electrons are exchanged between nearest neighbor atoms & will be described in more detail later.

Many ferromagnetic materials contain large number of magnetic domains consisting 10^{12} to 10^{15} atoms & aligned in same direction which results in large magnetization. It can also be visualized as presence of large number of individual crystals in a bulk polycrystalline material. The magnetic moment of the magnetic domains aligns in a specific axis the ferromagnetic material, which is also known as the easy axis. It happens due to coupling between the electronic spin and the angular momentum of the atomic orbit. The easy axis also makes the magnetic moment is anisotropic to the magnetization. When the direction of the applied magnetic field is not parallel to the specific axis, the magnetic field has to overcome the energy barrier for pulling all the moments away from the easy axis and align towards magnetic field. This energy barrier is known as the magneto crystalline anisotropy E_a and it is the atomic origin of hysteresis behavior in magnetic materials.

Some of the most common examples of ferromagnetic materials include Iron (Fe), nickel (Ni), and cobalt (Co) etc. Ferromagnetism have strong relationship on temperature. The magnetization of the ferromagnetic material is inversely proportional to temperature. The maximum temperature at which a ferromagnetic material retains its magnetization is known as the Curie temperature (T_c). When Temperature is more than curie temperature, the atomic spins orientations tends to misalign due to thermal agitation and leading to reduced magnetization similar to paramagnetic materials The magnetic susceptibility of ferromagnetic materials can be explained by Curie-Weiss law (Equation 2.4), the magnetization becomes zero for temperatures more than Curie temperature.

Hysteresis

Ferromagnetic materials have a special property of retaining the memory of an applied magnetic field event when it is removed. This behavior is known as hysteresis, and a plot of the variation of magnetization with respect to magnetic field reveals the hysteresis loop. This phenomenon occurs due to the presence of magnetic domains. Hysteresis is a very important property and is extremely useful for making magnetic memory devices. The hysteresis loop is measured by measuring the magnetization (M) of a ferromagnetic material while the applied magnetic field (H) is changed (Figure 2.3). Initially ferromagnetic material will follow the dashed line as H is increased. [12]

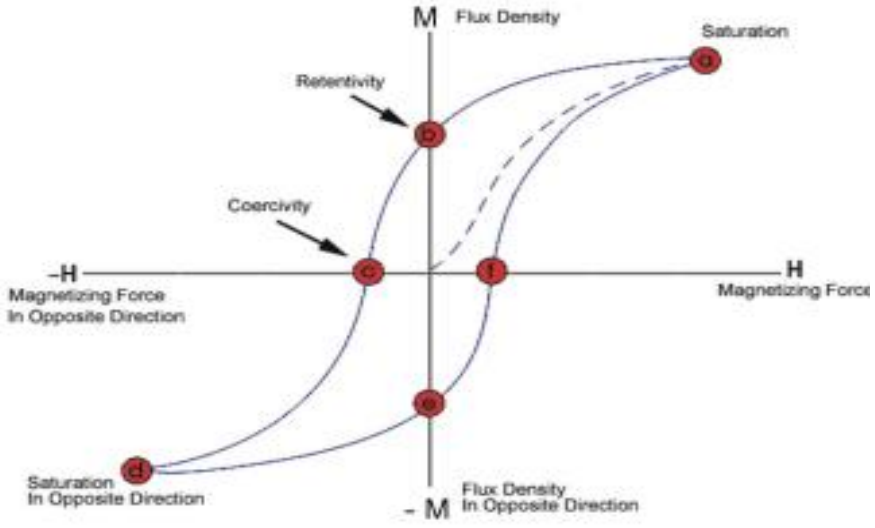

Figure 2-3 : Hysterisis Curve for ferromagnetic material

At point “a” almost all of the magnetic domains are aligned parallel to magnetic field. This point is known as the saturation magnetization as the application of an additional magnetic field will produce very little increase in magnetization strength. When magnetic field H is reduced to zero, the curve will move from point “a” to point “b”. It is apparent from non-zero value of

magnetization at point b, that at point “b” the material possesses magnetization even though the applied field is zero. This point also indicates the level of residual magnetism in the material. (i.e. some of the magnetic domains are aligned while many of them have lost their alignment). As the magnetic field is further reduced, the curve moves to point “c”, where the magnetization finally becomes zero (which means all the magnetic domains in the material are flipped). This point is called the coercivity.

The magnetic field required to reduce the residual magnetization to zero in the material is called the coercivity of the material. As the applied magnetic field is further increased in the negative direction, the material will become magnetically saturated but in the opposite direction indicated by point “d” in figure. Finally, reducing the field to zero brings the curve to point “e” which means presence of residual magnetism in the material which have similar magnitude as point “b”. When the applied magnetic field further increased, the magnetic moment becomes zero. As shown in figure (2-3) zero magnetization is achieved at some non-zero magnetic field, which is required to remove the residual magnetism. When the applied magnetic is further increased, the curve then moves to point “f” and back to the saturation point resulting in the completion of the loop. M vs. H plots are used to analyze the magnetic properties of dilute magnetic semiconductors DMS.

Following primary magnetic properties of a material can be determined using hysteresis loop.

1. **Retentivity** – Retentivity can be defined ability of a material to retain a certain residual magnetization even when external magnetic field is removed after achieving saturation. (Indicated by the value of Magnetization at point b on the M vs H curve (fig-2-3))
2. **Residual Magnetism or Residual Flux -** Residual Magnetism is defined as the magnetic moment that remains in a material when the external magnetic field force is removed. However it is same as retentivity when the material is magnetized to the saturation point. But it may be lower than retentivity when magnetic field did not reach the saturation level.
3. **Coercivity**- Coercivity represents the amount of reverse magnetic field that must be applied to a magnetic material to make the magnetic moment equal to zero. (The value of magnetic field at point c on the M vs H curve (fig-2-3).)
4. **Permeability** – Permeability is a property of a material that describes the easiness with which a magnetic moment can be induced in a material.

5. **Reluctance** – Reluctance represents the opposition that a ferromagnetic material shows to the establishment of a magnetic field. It is analogous to the resistance in an electrical circuit.

Antiferromagnetism

The antiferromagnetic materials have both kind of magnetic moments i.e. parallel and antiparallel . These moments tends to cancel out each other which leads to overall zero magnetization (Figure 2.2d). This effect is normally observed in transition metal oxides such as Nickel Oxide (NiO) and Cobalt Oxide (CoO). The temperature above which antiferromagnetic order vanishes is known Néel temperature (T_N). Above this temperature T_N, antiferromagnetic materials behave like ferromagnetic materials and their magnetic susceptibility can be explained by Curie-Weiss theory. But they have a negative intercept in negative exchange interactions in M vs H curve.[11]

Ferrimagnetism

The Ferrimagnetic behavior is similar to ferromagnetism and it is usually observed in ferrites and garnets. In ferrimagnetic materials, the interactions between nearest neighboring magnetic domains (atomic sublattices) are antiferromagnetic, but these magnetic domains have unequal magnetic moments and which results into a resultant net non-zero magnetic moment (Figure 2.2e). Such materials are generally consist of two or more different type of elements/ions for example Fe^{2+} and Fe^{3+} . The atomic sub-lattices of these atoms/ions are ferromagnetic & they have unequal magnetic moments. Ferrimagnetism is usually mediated by indirect exchange or superexchange interactions. Ferrimagnetic materials exhibits all the characteristics of ferromagnetic behavior: spontaneous magnetization, Curie temperatures, hysteresis, and remanence etc..[11]

Superparamagnetism

Superparamagnetism is observed in materials which are made of small crystallites which can randomly flip direction due to thermal fluctuations. As a result the material is not magnetic without applying any external magnetic field. But when an external applied magnetic field and these materials behave similar to paramagnetic materials. In such kind of materials, the moment of the complete crystallite tries to align with the external magnetic field which leads to strong magnetic moment. The energy required to change the direction of magnetization of a

crystallite is called the crystalline anisotropy energy (E_a). The crystalline anisotropy energy depends on properties of the material and the crystallite size (Equation 2.5). Thus

$$E_a = KV \tag{2-5}$$

E_a represents magneto-crystalline anisotropy energy, K is the net energy density & V is the crystellite volume. As the crystallite size decreases, the crystalline anisotropy energy also decreses, resulting in a decrease in the temperature at which the material becomes superparamagnetic. With a decrease in particle size to a point below a critical diameter, E_a becomes comparable to the thermal activation energy K_BT (where K_B is the Boltzmann constant, and T is temperature). [12] As the nanoparticles have small anisotropy energy barrier the magnetization direction of the nanoparticles can be easily moved away from the easy axis by thermal activation energy or the applied magnetic field. If the thermal activation is sufficient to overcome E_a then the magnetic moment may point in any direction and behave like paramagnetic atoms. Thus magnetic order still exists in the nanoparticles but each particle behaves like a paramagnetic atom with a large moment, this behavior is known as super-paramagnetism. Instead of aligning in a certain direction, there are rapid fluctuations in the magnetic moment alignment direction of the nanoparticles. The temperature at which thermal activation energy overpower the magnetic barrier of nano-particles is known as blocking temperature (T_b), given by Equation (2.6).

$$T_b = \frac{KV}{k_b \ln(\frac{\tau_{exp}}{\tau_0})} \tag{2-6}$$

where V is the particle volume, K is the anisotropy constant, τ_{exp} is the measurement time (usually 100 seconds), and τ_o is the lifetime due to the natural gyromagnetic frequency of the particles. Hence the typical value of the term $\ln(t_{exp}/t_o)$ is 25. The critical variables that affects blocking temperature T_b are the anisotropy constant (K), and the volume of the magnetic particle (V). At temperatures $T < T_B$, the moments of some of the particles are blocked: they do not possess sufficient magnetic energy to overcome the energy barriers in the timescale of the experiment. The energy barriers near zero magnetic field point (H = 0) cannot be overcome without increasing the thermal energy or external magnetic field. When temperature T is greater than blocking temperature T_b, the thermal energy is high enough to overcome the coupling forces and randomize the spins and hence the magnetic signal reduces. Since there is no longer any magnetic order, the internal magnetic field no longer exists and the material exhibits paramagnetic behavior. If the

material is non-homogeneous, a mixture of ferromagnetic and paramagnetic clusters of atoms exists at the same temperature.

2.2. Magnetic interactions in solids

The fundamental property of an electron which gives rise to its magnetic properties is its spin. No two electrons with the same spin can occupy the same energy state. This determines the orientation of spins of electrons in the various energy states, and is also responsible for properties such as polarization-dependent optical selection rules.

Although spin is a quantum-mechanical property, it can be understood via a semi-classical approach in terms of an electron orbiting along a circular orbit. Electronic spin angular momentum only contributes in part to the total magnetic moment of an atom. In addition, electrons around the atom also have orbital angular momentum associated with them. The interaction of the spins on the different electrons as well as their coupling with the angular momentum plays an important role in determining whether the spins on individual electrons have any form of collective order. Furthermore, application of an external magnetic field also contributes to the magnetic moment of the atom by changing the orbital momentum and resulting in a diamagnetic moment.

Diamagnetic behavior is exhibited by all materials to some extent. When an external magnetic field is applied on an electron orbiting an atom, it travels in a direction that induces an orbital magnetic moment, opposing the external field. The moment associated with such an electron is the diamagnetic moment. In addition, most materials exhibit a paramagnetic or a ferromagnetic contribution which far exceeds that of the diamagnetism. Para-magnetism is seen in materials with an unpaired number of electrons. This includes transition metals with incomplete inner shells, lattice defects, atoms or molecules with an uneven number of electrons as well as metals.

Although orbital moment of the electrons changes to oppose the external field, the unpaired electrons have a spin moment, which points in a direction parallel to that of the applied field. This results in a net positive paramagnetic moment, when a field is applied. There is no collective order in paramagnetic materials, which means that while the spins on the individual electrons are dependent on the external magnetic field, they do not interact strongly with each other.

Any collective magnetic order in a material is brought about by energy considerations. In other words, if there exists a spin configuration that would allow the entire system to lower its energy by aligning the spins in a specific orientation with respect to each other in the absence of an

external field, then some kind of ferromagnetic order will persist. The dominant interaction between two spins is the exchange interaction. The interaction between two magnetic dipoles $\boldsymbol{\mu_1}$ and $\boldsymbol{\mu_2}$ separated by r is defined by the energy that the system has respective to the values of the separation of the dipoles and the angles that the dipoles make. It is given by the Equation

$$E = \frac{\mu_0}{4\pi r^3}\left[\boldsymbol{\mu_1}.\boldsymbol{\mu_2} - \frac{3}{r^2}(\boldsymbol{\mu_1}.\boldsymbol{r})(\boldsymbol{\mu_2}.\boldsymbol{r})\right] \quad (2\text{-}7)$$

and is known as magnetic dipolar interaction. Two magnetic moments of size $\mu \approx \mu_B$ separated by $r \approx 1$Å would have energy of the order of $\frac{\mu^2}{4\pi r^3} \approx 10^{-23}J$ which translates to around 1K, meaning that the magnetic dipolar interaction cannot be the sole responsible for the high temperature ordering effects of ~ 1000 K.

The exchange interaction originates in the fermionic nature of the electron based on Pauli exclusion principle: no two fermions can occupy the same quantum state at the same time. As electrons are fermions, they are distinguishable, and the wave function of the system of two electrons has to be antisymmetric to the exchange of two electrons. This leaves two possible spin states: an antisymmetric singlet state χ_s with S=0 (in the case of the symmetric spatial state) and a symmetric triplet state χ_T with S=1 (in the case of the antisymmetric spatial state).

$$\psi_s = \frac{1}{\sqrt{2}}[\psi_a(\boldsymbol{r_1})\psi_b(\boldsymbol{r_2}) + \psi_a(\boldsymbol{r_2})\psi_b(\boldsymbol{r_1})]\chi_s$$

$$\psi_T = \frac{1}{\sqrt{2}}[\psi_a(\boldsymbol{r_1})\psi_b(\boldsymbol{r_2}) - \psi_a(\boldsymbol{r_2})\psi_b(\boldsymbol{r_1})]\chi_T \quad (2\text{-}8)$$

With the energies of the two possible spin states given by

$$E_s = \int \psi_s^* \widehat{H}\psi_s dr_1 dr_2 \quad E_T = \int \psi_T^* \widehat{H}\psi_T dr_1 dr_2 \quad (2\text{-}9)$$

The difference in energies of the singlet and triples state is given by

$$E_s - E_T = 2\int \psi_a^*(\boldsymbol{r_1})\psi_b^*(\boldsymbol{r_2})\widehat{H}\psi_a(\boldsymbol{r_2})\psi_b(\boldsymbol{r_1})dr_1 dr_2 \quad (2\text{-}10)$$

From this one can define the exchange integral

$$J = \frac{E_s - E_T}{2} = \int \psi_a^*(\boldsymbol{r_1})\psi_b^*(\boldsymbol{r_2})\widehat{H}\psi_a(\boldsymbol{r_2})\psi_b(\boldsymbol{r_1})dr_1 dr_2 \quad (2\text{-}11)$$

The basic properties of the spin operator require that, for a singlet state $\boldsymbol{S_1}.\boldsymbol{S_2} = -\frac{3}{4}\hbar^2$ while for a triplet state $\boldsymbol{S_1}.\boldsymbol{S_2} = \frac{1}{4}\hbar^2$. The effective Hamiltonian can hence be defined as[13,14]

$$\widehat{H} = \frac{1}{4}(E_s + 3E_T) - (E_s - E_T)\boldsymbol{S_1}.\boldsymbol{S_2} \quad (2\text{-}12)$$

The effective spin Hamiltonian is then

$$H_{spin} = -2J\boldsymbol{S_1}.\boldsymbol{S_2} \quad (2\text{-}13)$$

If $J > 0, E_s > E_T$ the triplet **S** = 1 state is the lower energy, stable one. In the case of $J < 0, E_s < E_T$ and the singlet **S** = 0 state is the lower energy one. The generalization of Eq. 2.7 to more than 2 spins is not trivial, yet by assuming that Eq. 2.7 still holds in many-body systems we arrive at Heisenberg Hamiltonian

$$\widehat{H}_{heisenberg} = -\sum_{ij} J_{ij}\boldsymbol{S_i}.\boldsymbol{S_j} \quad (2\text{-}14)$$

In systems where the electrons are localized on magnetic atoms, the interaction depicted by the Eqs. 2.7 and 2.8 is referred to as direct exchange. It requires, however, the strong overlap of the orbitals to be of considerable magnitude. As the electronic orbitals often extend less than one tenth of an interatomic spacing it is rarely a dominant magnetic interaction. Even in Fe, Co and Ni, that have 3d magnetic orbitals that extend quite far from the nucleus the interaction is not strong enough to explain the observed magnetic properties.

2.2.1 Exchange Interactions

Exchange interaction is the balance between magnetostatic and electrostatic energies. It can be understood by Pauli's exclusion principle, which states that no two fermions (electrons, in this case) can have the exact same quantum state. Consequently, two electrons with the same spin are spatially separated, thereby decreasing their electrostatic energy. This makes up for the increase in their magnetostatic energy, which is caused by the magnetic repulsion of the like spins.

The orientation of a small enough magnetic particles is governed predominantly by this exchange interaction. However, in a crystal lattice, other longer range interactions such as dipole interactions or anisotropy also begin to affect the magnetization direction. Dipole energy causes the moments at the surface of a magnetic material to get oriented along antiferromagnetic directions. On the other hand, anisotropy tends to orient the magnetic moment along certain crystallographic axes, known as easy axes. This comes about as a result of spin orbit coupling that results in different coupling energies along different crystallographic axes. The magnetic behavior of a material is a result of the sum total of all these interaction energies. In a ferromagnet, the energy bands are spin-split at the fermi level even when there is no external magnetic field present. The exchange

interactions in dilute alloys of magnetic elements are somewhat complex, and are usually understood in terms of hybridization between the localized spin-split atomic orbitals of the element with the energy bands of the rest of the lattice.

The orbitals of the magnetic atoms do not have sufficient overlap to develop ferromagnetism through direct exchange, which means indirect exchange mechanisms are more significant in magnetic semiconductors.

Indirect Exchange Interactions

Various exchange mechanisms have been evolved for explaining magnetism in transition metal (TM) and rare earth (RE) doped semiconductors. The three main classical indirect exchange mechanisms are

1. RKKY exchange
2. Double exchange
3. Super exchange.

In recent years based on the observations of ferromagnetism in II-VI and III-V DMS several other indirect exchange mechanisms have been developed. This discussion begins with the explanation of the theoretical models for indirect exchange interactions.

RKKY Exchange Interactions

RKKY is an indirect exchange mechanism which has been named after scientist who discovered it: Ruderman, Kittel, Kasuya, and Yosida. This mechanism explains the coupling of magnetic moments using Coulomb exchange interactions through energy bands electrons over large distances. This theory was formulated for investigating ferromagnetism phenomenon in metals, and is an efficient mechanism when a high concentration of free carriers are present (Figure 2.4a) [15-17]. The RKKY theory explains the spin polarization of the conduction band electrons as a function of the distance from localized moments it is also known as Friedel oscillations. The interactions can be either ferromagnetic or antiferromagnetic based on distance between atoms involved in interactions. This theory also explain the ferromagnetic behaviors for materials having 4f electrons. In transition metals 4f shells partly overlaps with 5d shells, there is an indirect exchange mechanism between the outer 5d electrons & 4f electrons . RKKY or carrier mediated exchange has been found to be the ferromagnetism mechanism in $Ga_xMn_{1-x}As$. This mechanism occurs because Mn acts as an acceptor in GaAs lattice and introduces a hole in to $Ga_xMn_{1-x}As$

system, hence also contributes a localized spin [18, 19]. The carrier-mediated exchange theory predicts a T_C that is dependent on the localized spin concentration as well as carrier concentration in these materials. However, the defect energy levels of transition metals lie in middle of bandgap and do not contribute any free carriers for supporting exchange interaction [20]. Overall, this indirect exchange mechanism provides flexibility for modifying magnetic properties by changing concentration of holes.

Double Exchange Mechanism

Double exchange is a term that was coined by Clarence Zener and this mechanism involves the coupling of magnetic ions in different charge states by the hopping of an electron from one ion to another through interacting with the p-orbital (Figure 2.4b) [21]. Spin flips are not allowed in this model and it is energetically favorable if both the ions have a similar magnetic structure. This mechanism explains magnetism in spinel magnetite, manganites, and Mn perovskites. This model has been used to describe the ferromagnetism in $In_{1-x}Mn_xAs$ [22]. In GaN, the TM *d* states split into a triply degenerate t_{2g} and a doubly degenerate e_g level (Figure 2.7b). In GaN the calculated levels sit at 1.44 and 0.22 eV (respectively) above the valence band maximum (VBM). The majority of t_{2g} levels have one electron in the case of Cr, two electrons in the case of Mn, and three in the case of Fe.

Superexchange

The exchange interaction which is resulted from the coupling of nearest neighbor transition metals through a shared cation, known as super-exchange intraction (Figure 2.4c). The mechanism was first pointed out by Kramers in 1934 and then developed in detail by Anderson in 1950 [23, 24]. It results from the virtual hopping of carriers between the completely filled p-orbitals of anions and the d orbitals of the magnetic TM cations. In order for electrons from both adjacent atoms to occupy the same p-level, they must be opposite in spin, a result of Pauli exclusion principle considerations.

This leads to an antiferromagnetic coupling of nearest-neighbor cations through a shared anion. This mechanism has more importance in ionic solids such as transition metal oxides and fluorides, where the bonding orbitals are formed by 3d electrons in the TM atoms and the 2p valence electrons of the diamagnetic oxygen or fluorine atoms. Superexchange interaction is also present

in the Nitrides. However the magnitude of strength of the exchange integral is roughly one order less than in the oxide-based materials [25]

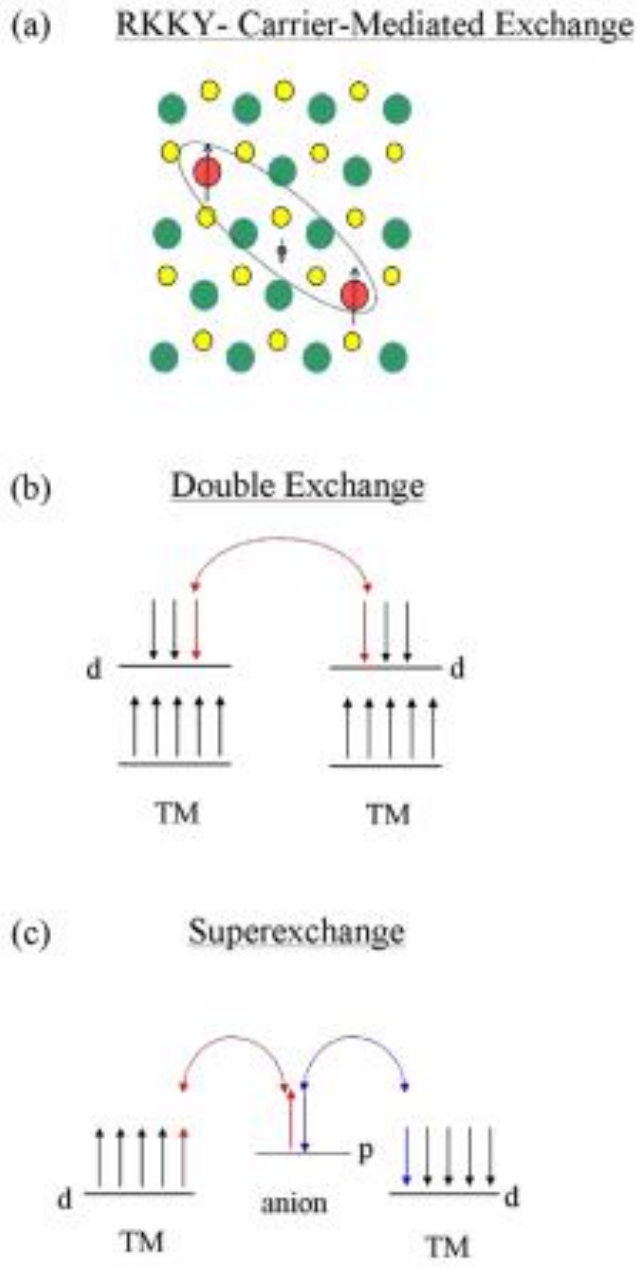

Figure 2-4: Classical indirect exchange mechanisms

Spin-Dependent Coupling Mechanism

Before proceeding further, it should be noted that there are two main spin-dependent coupling mechanisms in magnetic semiconductors that control the magneto-optical phenomenon. The first

is the coupling between the conduction-band electrons (s-character) and localized spins (d-character) this is denoted by $N_0\alpha$. The other main mechanism is hole exchange coupling: coupling between the valence band holes (pcharacter) and localized spins (d-character), denoted by $N_0\beta$. This generally increases with decreasing lattice constant [26]. In the tetrahedrally coordinated DMS, if the TM (d orbitals) or RE (d or f orbitals) ions substitute the host cation the resultant electronic structure will be affected by hybridization of the d or f orbitals of the magnetic ion and the p or s orbitals of the neighboring atoms. In RE ions both the d and f states can participate in spin-coupling, but the f-states are more localized and thus their coupling is expected to be weak.

2.2.2.Additional Exchange Mechanisms

In addition to the classical direct and indirect mechanism, additional exchange mechanisms have been proposed to explain the observation of dilute magnetic semiconductors in DMS. These additional exchange mechanisms are described below.

Bound Magnetic Polarons

In magnetic semiconductors the magnetic moments are polarized to form sizeable magnetic moments at the vicinity of the donor/acceptor impurities. These are known as bound magnetic polarons (Figure 2.8) [27]. Decreasing temperatures result in an increase in the polaron interaction distance, leading to overlap between neighboring polarons and so allowing them to interact through the magnetic imputers, forming correlated polaron clusters. When size of these clusters becomes equal to the size of samples the material starts behaving as a ferromagnetic material.

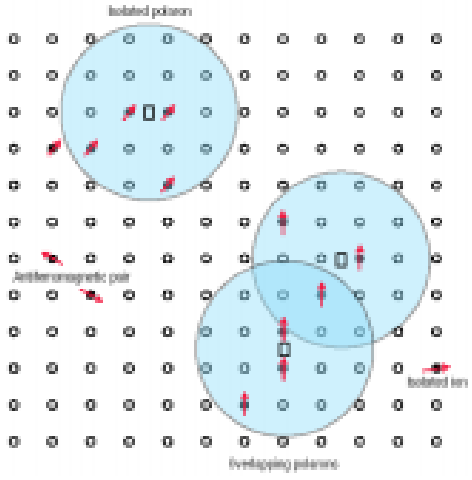

Figure 2-5 : Bound Magnetic Polaron Interactions

The direct interaction between these localized carriers is antiferromagnetic. However, the interaction between the bound magnetic polarons can be ferromagnetic for large concentrations of magnetic impurities. This model has been used to describe the origin of magnetism in semiconductor systems with low carrier density, such as electronic oxides.

Donor Impurity Band Exchange

A donor impurity band exchange model, proposed by Venkatesan, Coey et al., suggests that defect centers mediate ferromagnetism and are responsible for the magnetization seen in TM doped ZnO [27, 28]. Three scenarios for TM doping in ZnO were evaluated in this model (Figure 2.9). In the first scenario of a light 3d element (e.g. TM = Ti), the 3d spin-up states lie high in the 2p (O) and 4s (Zn) gap, overlapping the spin split donor impurity band. For the next element (TM = Mn) there is no overlap with the 3d level and the exchange is weak, and towards the end of the series (TM = Co) the 3d down states overlap with the impurity band which then has the opposite spin splitting for the same occupancy. High T_C are found when the unoccupied 3d states overlap the impurity band. The origin of the donor impurity band has been attributed to oxygen vacancies (F centers) in ZnO and it has been proposed that this model can be used to explain ferromagnetism in GaN, which can be caused by the d^0 centers.

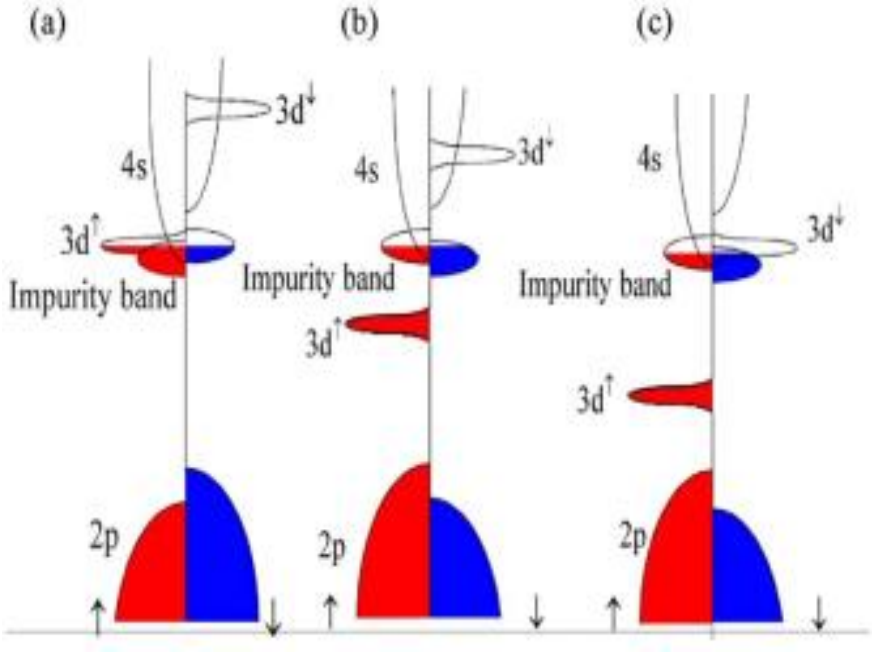

Figure 2-6 : Density of States for TM doped ZnO (a) TM = Ti, (b) TM=Mn, and (c) TM=Co

The higher magnetization that is seen in ZnO at the interfaces is due to the defects that are present in the region. Thus in order for long range magnetization to occur it is essential to have high carrier concentration and a large number of vacancies. Once the donor concentration increases significantly, the donors merge with the conduction band and then RKKY exchange mechanism begin to dominate.

The Litvinov and Dugaev model is used to explain ferromagnetism in both degenerate and non degenerate films. This model proposes an indirect exchange mechanism in which virtual electrons transition from the magnetic impurity acceptor level to the valence band [29]. This model applies to semiconductors in which there is a low concentration of magnetic ions and in which magnetic dopants do not introduce any free carriers. In this model the T_C depends on p-d exchange interactions and the energy between the TM impurity level and the band electron levels. This model has been applied to explain the ferromagnetism in $Ga_{1-x}Mn_xAS$ and $Ga_{1-x}Mn_xN$ films.

The next section reviews the underlying mechanisms of magnetism in dilute magnetic semiconductors.

2.3. Models describing magnetism in DMS

The basic model for DMS is of a magnetically inert host semiconductor doped with localized spins, which may then be doped with electrons or holes. In some cases such as that of Mn-doped III-V materials, the magnetic ion itself is an acceptor and acts as a source of holes. The magnetic spins are localized on much smaller scales than the carriers. The magnetic interactions seen in DMS are governed by an sp-d exchange, which allows carrier mediated magnetic order and leads to such effects as a giant Faraday rotation and the formation of bound magnetic polarons. Several mechanisms have been suggested that explain the origin of magnetism in DMS. Most theories attempt to identify the various spin coupling energetic concurrent in a system, and by plugging in the material parameters, attempt to estimate if the energetics lead to ferromagnetic, antiferromagnetic or spin-glass like interactions between individual atomic spins.

2.3.1.Mean Field Theory

Zener originally proposed a model for ferromagnetism in dilute alloys of transition metals, driven by the exchange interaction between carriers and localized spins [21]. The three important ideas behind the model are:

1. In an isolated atom, the lowest energy state is given by the electronic state where an incomplete d-shell has the highest spin - meaning that all the spins are aligned.

2. The exchange integral between d-shells of adjacent atoms always leads to anti-ferromagnetic order

3. The spin of an incomplete shell is strongly coupled to the conduction electrons. When this coupling dominates over the direct exchange, ferromagnetism is made possible.

The net spin coupling energy in such a system is a combination of three terms. The first one is the direct exchange between incomplete d-shell electrons while the second is the exchange between the d-shell electrons and the conduction electrons. The third interaction is the Fermi kinetic energy of the conduction electrons. This is at a minimum (0) when there is an even number of spin up and spin down electrons, since the spin distribution at the Fermi level is balanced. A combination of these three terms are given by :

$$E_{spin} = \frac{1}{2}\alpha S_d^2 - \beta S_d S_c + \gamma S_c^2 \qquad (2\text{-}15)$$

Here, $S_d \ \ and \ S_c$ are the net spin polarizations of the conduction electrons and the d-shell electrons respectively. The sign of E_{spin} determines the nature of magnetic order. While a positive value is indicative of antiferromagnetic order, a negative sign implies ferromagnetism.

This model was later modified by Dietl et al [30] to understand ferromagnetism in p-type DMS materials such as GaMnAs. The theory considers ferromagnetic correlation mediated by holes originating from shallow acceptors in the ensemble of the localized spins in doped magnetic semiconductors. For instance, in GaMnAs, Mn, which occupies the cation (Ga) sub-lattice in zinc-blende GaAs provides a localized spin and at the same time acts as an acceptor. Dietl's theory can be extended to several such p-type DMS, and has been used to estimate Curie temperatures of various candidates.

Dietl et al. proposed Zener Mean field model for describing ferromagnetism in various various zinc-blende semiconductors, it has also been used to determine the curie temperature T_C [31]. This model is based on the combination of the Zener and RKKY interaction models. It also accounts for the anisotropy associated with the spin-orbit coupling in RKKY interactions. The mean field theory also calculates the ferromagnetic interactions which are mediated through holes introduced by doping of transition metal ions (shallow acceptors). It was found that curie temperature (T_C) can be determined by computing the competition between the ferromagnetic and antiferromagnetic

interactions. The T_C values calculated by the mean field model for different materials were performed using following Equations.

$$T_c = T_{FM} - T_{AFM}$$

$$T_c(x) = A_F\left(\frac{x_{eff}}{0.05}\right)(\beta N_0[eV])^2[N_0(GaAs)/N_0]T_F - T_{AF}(\mathrm{x})$$

where A_F is the Fermi liquid parameter, x_{eff} is the effective spin concentration, β is the p, d exchange integral, N_0 is the concentration of cation sites, T_F is the ferromagnetic ordering temperature, and T_{AF} is the anti-ferromagnetic ordering temperature. The curie temperature T_C depends on the doping concentration of transition metal ions (x_{eff}) and concentration of holes. Usually Curie temperature of lighter elements is higher as compared to heavier elements. The SO coupling in the VB electrons is crucial for determining the curie temperature (T_C) and the direction of easy axis. Based on this model, GaN and ZnO are predicted to have a T_C higher than room temperature as they have smaller lattice constants and allow for greater p-d hybridization and reduced spin-orbit coupling.

2.3.2. Impurity Band Model

Sato and Katayama-Yoshida et al. performed ab initio calculations on GaN doped with 5 % of various TM [32]. Their model shows that the $Ga_{1-x}Mn_xAs$ exhibits a spin splitting of the density of states in the valence band, while GaN possess a spin-split density of states in the middle of the bandgap. Therefore, TM in GaN forms deep levels and does not generate free carriers [33]. It was shown that for half filled (or less) d shells such as in Mn, Cr, and V the ferromagnetic state is stable in GaN. For high Mn concentration the spin glass state is favored (Figure 2.10). Additionally, it was found that Fe, Co, and Ni doping are stable in the spin glass state in GaN. Furthermore, first principle calculations show that TM forms an impurity band and the ferromagnetism in the Nitrides is stabilized by a double exchange mechanism and broadening of the impurity band . Mean field approximations predicted a high T_C of 500 K and 350 K for 5 % Cr and Mn doped GaN respectively [34,35]. The double exchange mechanism in this system favors short range interaction between nearest neighbors. For a high T_C, the model requires a large concentration of TM (~ > 20 %) [56]. Further Monte Carlo simulations revealed that the T_C of Mn doped GaN is on the order of tens of Kelvin and so RT ferromagnetism is not feasible. This suggests that the mean field approximation

overestimates the T_C significantly. It has been suggested that any RT ferromagnetism found experimentally is due to the presence of MnN clusters or secondary phases [36].

2.3.3. Bound Magnetic Polaron

An important attribute of diluted magnetic semiconductors is the sp-d exchange coupling between spins of magnetic ions and those of the impurity electrons in the semi-conductor band. This results in phenomena such as valence band splitting under magnetic field and polaron effects. A bound magnetic polaron (BMP) can be described as group of electrons/holes which are bound to impurity atoms through orbital exchange interactions. These interactions can render carriers parallel or anti-parallel to the magnetic impurity, depending upon the system. These two configurations differ in energy, and this results in a non-zero spin flip energy that is a characteristic of BMPs. The net energy of the system can be lowered if the ions are aligned parallel to each other, since they all interact with carriers the same way. At low temperatures, where the s-d exchange energy exceeds K_BT, mutual alignment of the ions and carriers results in a ferromagnetic. At higher temperatures however, the spins of the magnetic ions are not constant anymore. A nonzero magnetization results from the spin fluctuations within any carrier orbit. While the former instance comprises the collective regime, the latter is a characteristic of the fluctuation regime.

The temperature up to which a BMP can facilitate magnetic order depends upon the nature of the interactions between the atomic spins and the charge carriers. The net exchange has been computed by Durst et al [32] based on the polaron-pair model. This model considers the interaction between a pair of BMPs via a shared interstitial area, where the magnetic ions interact with carriers belonging to both the polarons.

Such an area is crucial for carrier mediated ordering of the individual polarons. Fig. 2-7 shows a schematic of the polaron-pair model. The Hamiltonian that results from this model is given by :

$$H_m = [s_1.S_1 + s_2.S_2] + K'(s_1 + s_2).S_3 + Js_1.s_2 \quad (2\text{-}16)$$

where K is the intrapolaron ion-carrier exchange constant, K' is the interstitial ion- carrier exchange constant, J is the direct carrier-carrier exchange constant, s_1 and s_2 are the carrier spins, S_1 and S_2 are the net polaron spins, and S_3 is the collective spin of the interstitial region. Donor bands are relatively large and s-d interactions, weak. Therefore, in cases where these are involved in the formation of BMPs, the collective phase is observed only at low temperatures. On the other

hand, when the more localized valence bands are involved, the p-d interaction is strong enough to sustain collective order even at higher temperatures.

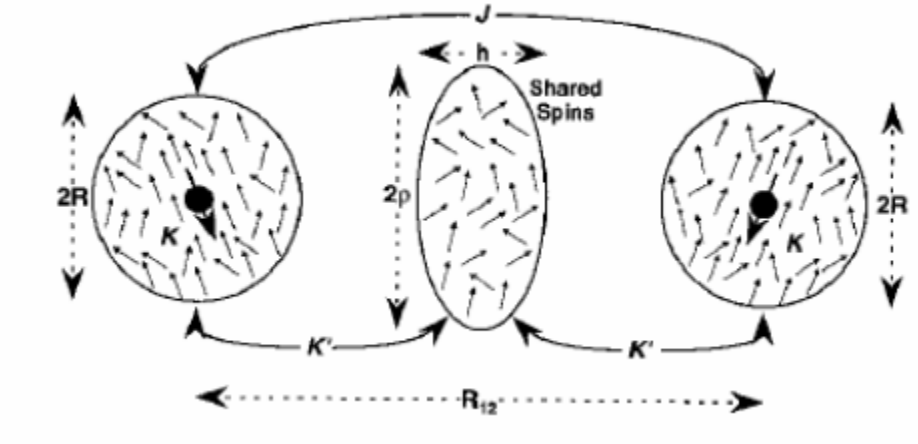

Figure 2-7: Schematic of Bound Magnetic Polaron Model

Coey et al [27] have proposed a model for n-type DMS materials based on exchange interaction between highly correlated narrow impurity bands and the atomic spin moment on the dopant ions. Figure 2.3 shows a schematic of the interaction in oxides, where defects such as oxygen vacancies act as a source of electrons. These electrons lie in hydrogenic orbitals with characteristic Bohr radii. As their concentration increases, their individual orbits extend out into narrow impurity bands. The electrons interact with all the magnetic ions that lie within their orbit. Each electron has an exchange interaction with all the magnetic ions lying within its orbital or sphere of influence. If there are a large enough number of magnetic spins within the orbital, the electron is completely spin polarized. Furthermore, the atomic magnetic moments have an indirect exchange interaction mediated by the carriers, that results in their ferromagnetic ordering.

2.4. Literature Review on Transition metal doped DMS

Extensive research works has been done on magnetic semiconductors for searching DMS which exhibit room temperature ferromagnetism. At initial stage, the work were mainly on focused on Mn–doped Group II-VI compound semiconductors (eg. CdSe, CdTe, ZnSe, ZnTe) [131] and then it was gradually shifted to Group III-V (GaAs, GaP, GaN, GaSb, InAs, InP, InSb) [19,30], Group IV-IVc compounds (PbS, PbSe, PbTe) [132] and even elemental semiconductors (Si, Ge). Ferromagnetism was reported to appear in such many systems but their Curie temperature (T_C) lies well below the room temperature which has limited technological interest [19]. In II-VI semiconductors divalent (2+) magnetic ions (Mn, for example) can easily occupy the group-II

cation sites of the host lattices, resulting in antiferromagnetic or spin glass ordering at higher concentrations . Evidence of ferromagnetism was observed in highly p-type doped ZnTe films with T_C ~ 30 K. In case of III-V DMS's, the highest reported T_C is 110 K for 5.3% Mn doped GaAs [19,30]. Therefore, the search for high T_C ferromagnetic semiconductors was still on.

The major breakthrough in the field of DMS was appeared in the year of 2000, when the groups of T. Deitl et. al. [30] successfully explained the ferromagnetic ordering in Mn-doped GaAs. They showed that substitution of Mn^{2+} at trivalent Ga site can introduce holes within the host lattice and the ferromagnetic interaction between the localised Mn ions was mediated through these holes; giving rise to long range ferromagnetism. Besides this, they also estimated the values of probable T_C for a variety of TM-doped semiconductors and predicted that TM-doped wide band-gap oxide semiconductors (for example, ZnO, TiO_2, SnO_2, In_2O_3, HfO_2, etc.) can be the promising candidate to exhibit required high T_C ferromagnetism. Their calculations also have shown that ferromagnetism is stable in a DMS which is based on a wide bandgap semiconductor. In addition to that, ab initio calculations based on local density approximation (LDA) was also performed for TM-doped ZnO-based semiconductors that showed it is very possible to stabilize ferromagnetism in such oxides [72]. These theoretical studies were the first step to oxide-diluted magnetic semiconductors (O-DMS) and several groups started to work in this field. The experimental observation of RT FM in Co:TiO2 thin-films [133] has obviously encouraged experimental studies and intensive experimental work has begun in the condensed matter community on O-DMS.

Initially Dietl et al.. based on their theoretical study using zener model predicted that room temperature ferromagnetism should exist in heavily p-type doped ZnO [30,43]. Since magnetic Co is highly soluble in ZnO, ZnO-Co system soon became one of most studied DMSs for applications requiring ferromagnetism near room temperature. Some subsequent theoretical studies using Density Functional Theory (DFT) and experimental works show that n-type Co-doped ZnO also possesses room temperature ferromagnetism. ZnO doped with other transitional metals (V, Mn, Fe and Cu) also have been studied. Recently many researchers try to study various characterstics like electronic spin, magneto-transport properties etc, of ZnO based by theoretical or experimentation techniques. Some of these researches are as followed.

Lee et al., [134] have claimed that Co-doped ZnO DMS thin films prepared by using sol-gel method exhibits room temperature ferromagnetism. For Cobalt doping concentrations of 25%, they reported existence of secondary phase which may be due to Co_2O_3 /Co_3O_4. Even for lower

concentrations of Co there was no extra peak was detected by XRD. However, the authors still concluded that there is some possibility that clusters formations might have caused the ferromagnetic behavior.

Ando et al., [135] have presented the presence of strong magneto-optical effect in Co doped ZnO DMS near the optical band gap. They observed Magnetic circular dichorism (MCD) and Faraday rotation for 1.2% & 1.6 % Co doping at 5 K. Also as per their observation the above effects were much higher than that of pure zinc oxide (ZnO) and these effects became negligible at room temperature.

Jin et al., [136] also evaluate the effect of TM doping on ZnO thin films prepared by molecular-beam epitaxy (MBE) technique. They discovered that dopant solubility behavior can be determined by ionic radius and valence state. They also reported that Mn^{2+} and Co^{2+} have a high solubility among all other 3d Transition Metal ions. From the observations it was suggested that there is a strong coupling interactions between s-p bands of zinc oxide with valence electrons of Mn^{2+} and Co^{2+}.

Saeki et al., [137] have reported the room temperature ferromagnetism in Vanadium doped ZnO samples fabricated through pulsed laser deposition. The Curie temperature was found to be more than 300 K for dopant concentrations 5% to 15%. Samples having very high carrier concentration of the order of 10^{18} cm^{-3} only showed ferromagnetism, while the insulating samples were not ferromagnetic.

Schwartz et al., [138] also observed room temperature ferromagnetism in Nickel doped Zinc Oxide nanocrystals synthesized by using colloidal precursor solution. The curie temperature was found to be more than 300K.. In addition to the ferromagnetism, significant super-paramagnetism was also observed from the Zero Field Cooled (ZFC) and Field Cooled (FC) magnetization data.

Han et al., [139] have also reported ferromagnetism in Fe & Cu doped ZnO samples. The curie temperature was found to be 550 K . They have also reported increase in magnetic moment of ZnO samples due to copper (Cu)- doping. Also they observed large magneto resistance for temperatures below 100 K.

The mechanism of origin of ferromagnetism in Fe & Cu doped ZnO samples was studied by Shim et al., [140] using zero field nuclear magnetic resonance (NMR) and neutron diffraction. Their measurements revealed the existence of the room temperature ferromagnetism at low

concentration Cu doping into ZnO samples with 5% Fe doping. They reported that it might be due to formation of $ZnFe_2O_4$ nano-clusters.

Yen-Fa Liao et al., [141] have also investigated ferromagnetism in Cobalt doped ZnO nanoparticles prepared by thermal hydrolysis. The ferromagnetic moment per Co^{2+} ion was found to be about 0.02 m_B at room temperature. The electronic structure of the samples was also studied. The study revealed that ferromagnetism might have been originated due to the interaction of moments happens through the impurity band.

Yi Wang et al., [142] have also reported the existance of room-temperature ferromagnetism in Co-doped zinc oxide samples synthesized by the solid state reaction method. The magnetic properties of the hydrogenated samples were measured at 10K and 300K by using SQUID magnetometer. Their observations confirmed existence of room temperature ferromagnetism in Co-doped ZnO samples & the saturation magnetization was found near to $0.056\mu_B$ per Co atom at coercive field of about 310Oe. Fukumura et al., [143] have conducted a study on Mn doped ZnO samples prepared using pulse laser deposition & they confirmed the predictions made by Dietl et al., [30] using mean filed theory. They reported that Mn ions can be doped in ZnO (up to 35%) beyond equilibrium solubility limit of approx. 13% without phase segregation. They observed significant change in ZnO lattice parameters & bandgap due to increased solubility. However, they also investigated ferromagnetism using SQUID measurement for field cooled (FC) and zero field cooled (ZFC). Their measurements revealed existence of a spin-glass behavior which was attributed to higher value of the temperature corresponding to a stronger antiferromagnetic exchange coupling.

Jung et al., [145] also studied structural & magnetic properties of Mn-doped Zinc Oxide films synthesized by molecular-beam epitaxy & reported existence of ferromagnetism. The analysis of XRD spectra revealed that the position of the diffraction peak shifted to lower angle on increasing the concentration of Mn doping which may be due to Mn ions substituting Zn ions. The curie temperature was also calculated from magnetization measurement (at 0.1 T) & it was found to be 30 K for 10% doping and 45 K for 30% doping. On the other hand, the composition study using secondary ion mass spectrometer revealed the existence of Zn^{2+} at the surface and Mn_2O_4 phase & which should be responsible to the magnetism of the Mn doped ZnO nanostructure. The existence of secondary phase may be responsible for low curie temperature.

Zinc oxide nano-crystals, pure and doped with transition metal ions, have been synthesized using colloidal techniques; after purification and concentration protocols, the ZnO solutions are mixed with mono-disperse Au colloidal suspensions and used for thin film depositions. The dopant presence has been found to affect the Carbon Mono-oxide (CO) optical sensing properties of the nano-composite ZnO–Au films: compared to pure ZnO, an increase in sensitivity up to 80% and 55% has been detected for Co-doped and Mn-doped ZnO respectively, while Ni-doped ZnO films show only minor improvements [146].

Absorption spectra of Mn^{2+}-doped ZnO quantum dots have been studied with the linear-response time-dependent density functional theory. The excitonic transition maximum shifts to higher energy and decreases in intensity with increasing Mn^{2+} concentration. The lowest excitonic transitions split in the spin-up and spin-down manifolds due to sp–d magnetic exchange between the Mn^{2+} and ZnO conduction and valence band carriers. Increased Mn^{2+} concentration leads to a broadening and increase in the intensity of the mid gap charge-transfer electronic absorption band, which results from excited-state splitting arising from double exchange magnetic interactions involving Mn^{2+} ions and the photo-generated hole. [147]

The modulation of the distribution of magnetic ions embedded in the host is crucial for the functionality of dilute magnetic semiconductors. Through an element-specific structural characterization, we observe the formation and enhancement of an unrevealed Co-doped ZnO phase and consequently magnetic properties from paramagnetism to ferromagnetism are controlled by surface-modification. [148]

Undoped and Ni-doped ZnO micro-rod arrays were successfully synthesized by the spray pyrolysis method on glass substrates. Analysis of the samples with X-ray diffraction and scanning electron microscopy showed that these micro-rod arrays had a polycrystalline wurtzite structure with a highly c-axis preferred orientation. Photoluminescence studies at both 300 and 10 K show that the incorporation of nickel leads to a relative increase in the visible blue light band intensity. Magnetic measurements indicated that Ni-doped ZnO samples exhibit ferromagnetic behavior at room temperature, which is possibly related to the presence of point defects. [149]

Recently an experimental research study was conducted to calculate the nature of magnetic interactions in transition-metal doped ZnO using the local spin density approximation and Local Spin Density Approximation (LSDA+U)method of density functional theory with (i) single transition metal ion types (Cr, Mn, Fe, Co, Ni and Cu) substituted at Zn sites, (ii) substitutional

magnetic transition metal ions combined with additional Cu and Li dopants, (iii) substitutional magnetic transition metal ions combined with oxygen vacancies and (iv) pairs of magnetic ion types (Co and Fe, Co and Mn, etc.) [150]

3. THEORETICAL STUDIES ON DILUTE MAGNETIC SEMICONDUCTORS

The critical temperature in the DMSs is still low to have significant substantial practical impact, fuelling the quest for room-temperature ferromagnetism which has been reported in most of magnetically doped nitrides and oxides semiconductors as reviewed in the subsequent section. It should be mentioned that the process is rather complex and the experiments are not quite as clear cut as one would like them to be which breeds some degree of controversy. Recent theoretical treatments have yielded useful insight into fundamental mechanisms involved in ferromagnetism, but there is still inconsistency between the theoretical and experimental results, and also among the various theories as well as among the experiments. From both the theoretical and experimental points of view, this field is still at the beginning of the road toward understanding and controlling magnetism in these systems.

Mean-field theory assumes ferromagnetic correlations mediated by holes from shallow acceptors in a matrix of localized spins. Dietl *et al*. have applied the Zener model with a proper description of the valence band structure to determine the value of the Curie temperature in GaAs:Mn. The model takes into account the anisotropy of the carrier-mediated exchange interaction related to the spin-orbit coupling in the host material. The Curie temperature is proportional to the density of Mn ions and hole density.

3.1. Theoretical Studies on magnetism TM doped DMS

Consider DMS of the type $A_{1-x}Mn_xB$, where the parent material AB is assumed to be a non-magnetic compound and both of the exchange interaction between carrier and impurity spins, and the direct exchange interaction between magnetic impurities are taken into account

$$H = \sum_{ij\sigma} t_{ij} a_{i\sigma}^{+} a_{j\sigma} + \sum_{i} u_i - J \sum_{<ij>} \overrightarrow{S_i}\,\overrightarrow{S_j} \qquad (3\text{-}1)$$

where u_i is either u_i^A or u_i^M depending on the ion species occupying the i site

$$u_i = \begin{cases} E_A \sum_\sigma a_{i\sigma}^+ a_{i\sigma} & i \epsilon A \\ E_M \sum_\sigma a_{i\sigma}^+ a_{i\sigma} - \Delta \sum_\sigma a_{i\sigma}^+ a_{i\sigma}(\sigma S_i) & i \epsilon Mn \end{cases} \quad (3\text{-}2)$$

Here $a_{i\sigma}^+(a_{i\sigma})$ is the creation (annihilation) operator for a carrier with spin σ at i site; S_i denotes the spin of localized impurity at i site ; Δ is the effective coupling constant between the localized spin and itinerant spin; J is the coupling constant between the neighboring localized impurity spins, which depends on their distance and for the anti-ferromagnetic exchange interaction case J < 0. To consider the effect of the direct exchange interaction between magnetic impurities on Tc, dividing equation (3-1) into the impurity term and the itinerant carrier term

$$H_{imp} = -\sum_i h S_i^Z - J \sum_{<ij>} S_i^Z S_j^Z \quad (3\text{-}3)$$

$$H_{carr} = \sum_{ij\sigma} t_{ij} a_{i\sigma}^+ a_{j\sigma} + \sum_i u_i \quad (3\text{-}4)$$

where h is the field induced by the polarization of the carrier spins. Where $S_i^Z = \pm S$ is the localized spin also known as Ising spin and H_{imp} is the molecular field approximation as $S_i^Z S_j^Z = \langle S_i^Z \rangle S_j^Z + \langle S_j^Z \rangle S_i^Z - \langle S_i^Z \rangle \langle S_j^Z \rangle$ Within this mean approximation, the Hamiltonian (3-3) become

$$H_{imp}^{MF} = NxJ\gamma m^2 - \sum_i S_i^z (h + 2J\gamma m) \quad (3\text{-}5)$$

where N is the number of lattice sites, *x* is Mn density, $m = \langle S_i^z \rangle$ refers to the average magnetization per lattice site, γ is the effective number of surrounding impurities a given impurity interacts with.

We apply CPA to the Hamiltonian (3-4). In CPA the carriers are described as independent particles moving in an effective medium of spin-dependent coherent potentials. The coherent potential $\sum_\sigma (\sigma = \uparrow, \downarrow)$ is determined by demanding the scattering matrix for a carrier at an arbitrarily chosen

site embedded in the effective medium vanished on average. By using a bare semicircular non-interacting density of states (DOS) with half bandwidth W : $\rho_o(z) = \frac{2}{\pi W^2}\sqrt{W^2 - z^2}$ we obtain a quadratic equation for $G_\sigma(\omega)$ and it is solved analytically by using Farrari method [37,38]. Throughout this work, we assume that the carriers are degenerate. Then the carrier energy can be expressed as

$$E_{carr}(m) = \int_{-\infty}^{\mu} \omega\big(\rho_\uparrow(\omega) + \rho_\downarrow(\omega)\big)d\omega \tag{3-6}$$

where μ is the chemical potential and $\rho_\sigma(\omega) = -\frac{1}{\pi}\tilde{S}G_\sigma(\omega)$ is the DOS with spin σ . The free energy per site of the system (1) at temperature T is given as

$$F(m) = E_{carr}(m) + hmx + xJ\gamma m^2 - xk_BTln\left(\sum_{S^z=\pm S} e^{\beta(h+2J\gamma m)S^z}\right) \tag{3-7}$$

By minimizing F with respect to m we obtain the following equation for h

$$h = -\frac{1}{x}\frac{dE_{carr}(m)}{dm} \tag{3-8}$$

By using the Weiss molecular field theory, each impurity spin feels an effective field $\bar{h} = h + 2J\gamma m$ and the local magnetization is then calculated by

$$m = SB_S\left(\frac{\bar{h}S}{k_BT}\right) \tag{3-9}$$

where $B_S(x) = \frac{2S+1}{2S}\coth\left(\frac{2S+1}{2S}x\right) - \frac{1}{2S}\coth(\frac{1}{2S}x)$ is the conventional Brillouin function and for Ising spin $S = \frac{1}{2}$

The Curie temperature is determined by differentiating both sides of Eq. (3-9) with respect to m at m = 0. This leads to the formula

$$k_BT_C = \frac{S(S+1)}{3}\left(-\frac{1}{x}\frac{d^2E_{carr}(m)}{dm^2}\bigg|_{m=0} + 2J\gamma\right) \tag{3-10}$$

So, we have

$$T_c = T_{c0} - T_{AF}$$

where $T_{c0} = -\frac{S(S+1)}{3xk_B}\frac{d^2E_{carr}(m)}{dm^2}\Big|_{m=0}$ is the Curie temperature of the system in the absence of antiferromagnetic interaction between magnetic impurities; and $T_{AF} = \frac{2S(S+1)}{3k_B}J\gamma$ describes the contribution of the antiferromagnetic interaction to the Curie temperature. Above equation has been derived in some early studies within the Weiss mean field theory, implies that the Curie temperature is determined by competition between the ferromagnetic and antiferromagnetic interactions [39].

Curie temperature is complicated function of carrier density, magnetic impurity density, carrier mean free path etc.

Curie temperature has been plotted against different carrier concentrations for different values of magnetic dopant (Mn) concentration and mean free path using equation (3-10) and compared against predictions from standard Virtual Crystal Approximation (VCA) method .

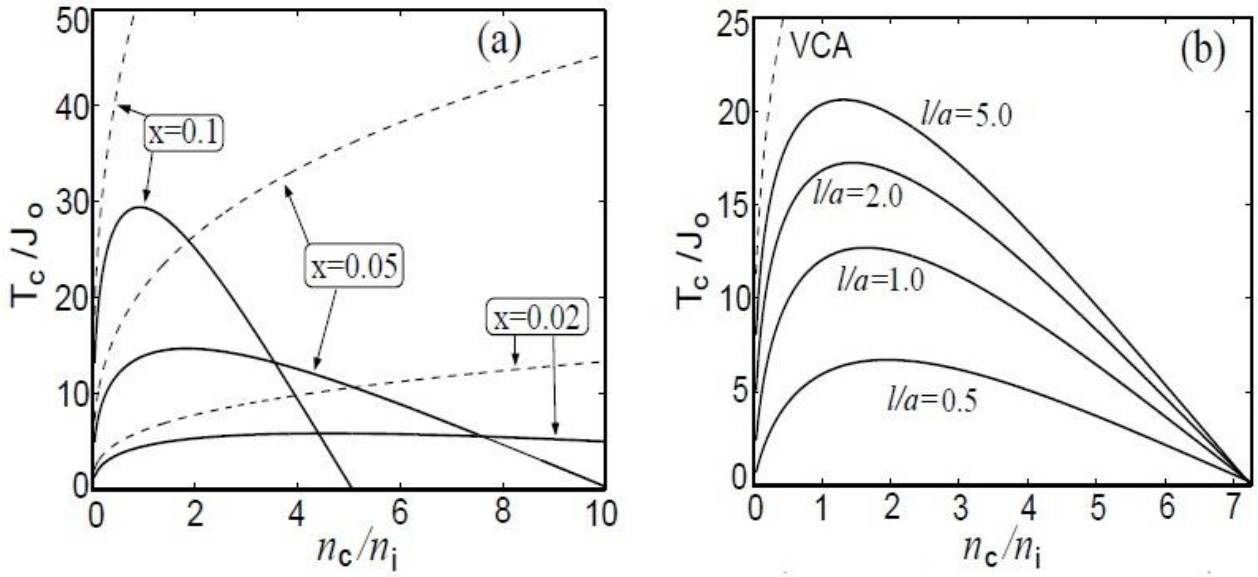

Figure 3-1 : (a) Calculated Curie temperature as function of normalized carrier density (n_c/n_i) for different values of x & fix MFP. *(b)* Calculated Curie temperature as a function of normalized carrier density (n_c/n_i) for different values of MFP & fix x. VCA computations has been shown in dashed line.

Upon analyzing the above results from theoretical calculations it is apparent that maximum Curie temperature is obtained for optimum carrier density n_c/n_i ~ 0.5 - 2 and also T_c first increases with concentrations for very low values of x after attaining it's maximum values it starts decreasing. T_c

cannot be increased by just increasing magnetic impurity concentration for optimum carrier density (n_c/n_i) actually we have to maximize mean free path for obtaining maximum curie temperature. Also curie temperature depends upon type of magnetic impurity being doped however it affects amount of magnetization below curie temperature also. The elements with large number of unpaired valence electrons shows lager magnetization as well as curie temperature as compared to those which have less unpaired valence electrons as shown in the figure below

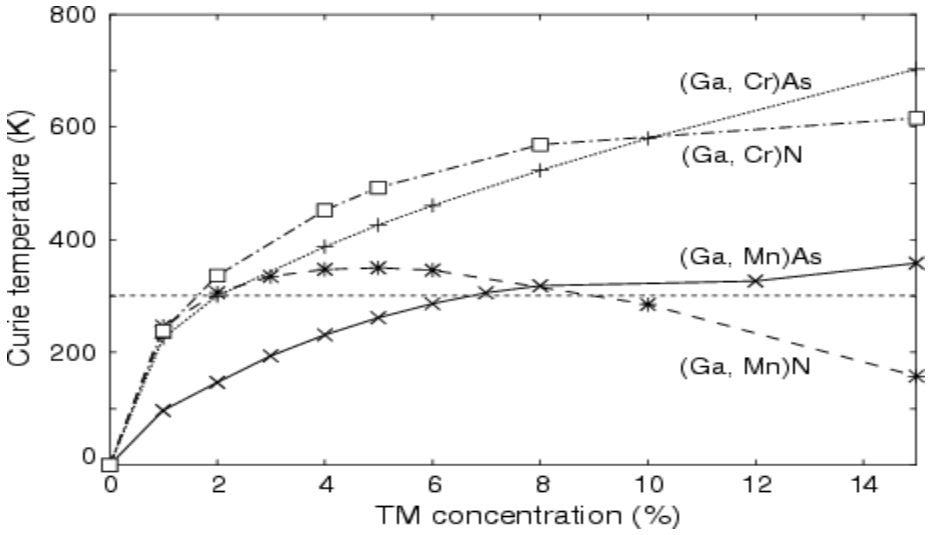

Figure 3-2 : Curie temperature as function of Magnetic impurity doping concentrations for Mn & Cr doped in GaAs & GaN

From figure 3-2 it is apparent that curie temperature of Cr doped GaAs/GaN is more as compared to Mn doped GaAs/GaN because Cr has one more unpaired valence electron as compared to Mn which contribute to higher net spin of Cr ions in the lattice which give rise to large amount of magnetization and also contribute to higher ferromagnetic interactions as compared to Mn in the host semiconductor lattice.

This model suggests that GaN and ZnO might exhibit critical temperatures above 300 K due to the small spin-orbit coupling, provided that a sufficiently high hole density can be achieved (10^{20} cm^{-3}), which is much higher than that achieved so far or achievable in both semiconductors. The source of holes does not necessarily have to be the TM ions. However, the need to incorporate as many magnetic ions as possible is not consistent with adding other acceptor like impurities as both compete for the same cation site and end up reducing the magnetic ion concentration. According to mean-field theories it is difficult to achieve ferromagnetism in n-type semiconductors due to the

generally smaller s-d interaction. Mean-field theory usually overestimates the stability of ordered phases, which may lead to overly optimistic predictions of the critical temperature [40].

3.2. Theoretical Studies on Photo-Induced Ferromagnetism

In recent years extensive research work is being done towards realizing Dilute Magnetic Semiconductors with room temperature ferromagnetism for realizing a new class of spintronics devices. These devices include spin valve, spin Light Emitting Diodes (spin LED), spin transistors, high density non-volatile memory, magnetic sensors, optical isolators, logic devices, and ultra-fast optical switches. These devices offer potential advantages in terms of higher speed, greater efficiency by manipulating the electrons spin in addition to its charge. The best-known successful spin-based devices at present are the magnetoresistance (MR) sensors made of multilayer's containing metal ferromagnetism, showing giant magneto-resistance (GMR) or tunneling magneto-resistance (TMR), which is currently used in the read heads of a hard disk drive. [41,42]

Conventionally II-VI based DMSs are difficult to dope by Transition metal ions to create p- and n type, which makes the materials less attractive for applications. The III-V semiconductors such as GaAs are already in use in a wide variety of electronic equipment in the form of electronic and optoelectronic devices, including cellular phones (microwave transistors), compact disks (semiconductor lasers), and in many other applications. However, these semiconductors are nonmagnetic but using Molecular Beam Epitaxy Technique Transition Metals ions can be doped to create III-V DMS.[43-48].

Many researchers have reported possibility of room temperature ferromagnetism in transition-metal-doped semiconducting oxides like ZnO and TiO_2. Although many contradictory experimental results, debating the success versus failure of obtaining a Tc above room temperature based on such dilute magnetic oxide systems, have injected much excitement about the origin of ferromagnetism in these systems. Among all these systems, ZnO belongs to the list of the most suitable candidates for spintronics application due to its abundance and environment-friendly nature and also due to its potential as a suitable optoelectronic material with a wide band gap (~ 3.3eV). However, the experimental success with < 4% Mn doped ZnO thin film has posed a challenge to the theoretical understanding of ferromagnetism for such systems. Further experimental studies reveal the importance of defects such as interstitial zinc and oxygen vacancies

for the magnetic ordering in such systems. Regarding the experimental studies, it can be commented that the presence of long-range ferromagnetic ordering, especially the magnetic moment per cation and Tc depend largely on critical details of the sample. [49,50]

The optical properties of Dilute Magnetic semiconductors are capturing attention of researchers because laser radiation can control both charge and spin dynamics. The influence of the laser field on the electronic system is reactive rather than dissipative and follows ultimately from a change in the effective electronic Hamiltonian equations. [51-53]

In the DMS material $Ga_xMn_{1-x}As$ (typically x ≈ (1 - 10%)) the Mn ions can serve dual purpose, acting both as dopants(acceptors in this case) and as magnetic impurities, whose spins align at the ferromagnetic transition In a sample with a fraction x of Mn randomly located at the cation sites is the fraction of sites containing Mn atoms without a magnetic first neighbor. Consequently, samples with a low Mn concentration (x ' 0.01) and no band carriers are paramagnetic. It has been shown that two localized spins in a semiconductor can interact via the virtual carriers created in the (otherwise empty) bands by a laser of frequency smaller than the band gap as shown in figure 3-5. The effective interaction is a ferromagnetic Heisenberg coupling which we shall call optical RKKY (Ruderman-Kittel-Kasuya-Yosida). [54-56]

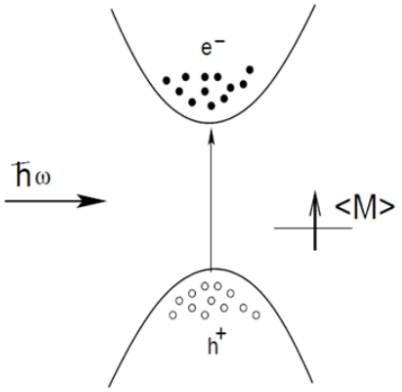

Figure 3-3 : A schematic picture of light induced ferromagnetic in diluted magnetic semiconductor

Photo induced magnetization was first demonstrated by Krenn et al. [57] who found a magnetization signal in $Hg_{1-x}Mn_xTe$ which depends characteristically on the degree of polarization of exciting radiation. The measured photo-magnetization increase linearly with photon power to certain value of photo power, but saturates on increasing the photon power. Photoinduced magnetic effects have been extensively studied in a variety of systems, including

cyanometallate-based magnets, spin crossover complexes, diluted magnetic semiconductors, doped manganite and spinel.

A number of early experiments regarding the photo induced magnetization have been reported for the diluted magnetic semiconductors system. Photo induced magnetization in ferromagnetic (Ga,Mn)As thin films caused by spin polarized holes generated optically also has been observed. The observed result suggest that a small amount of non-equilibrium carrier spins can cause collective rotation of Mn spins presumably p-d exchange interaction. The realization of ferromagnetism in a semiconductor results in many unique phenomena which have no analogy in the standard of magnetism. For instance, the hole-mediated ferromagnetic exchange that occurs in this semiconductor opens the possibility to change the magnetic properties of (Ga,Mn)As by modulation of the hole concentration and a huge photoinduced magnetization of about 15% of the saturation magnetization in ferromagnetic (Ga,Mn)As films. This opens the way to ultra-fast manipulation of the magnetic state of (Ga,Mn)As. The photoexcited non equilibrium spin polarization in (Ga,Mn)As relaxes with a decay time of 30 ps, which is related to the spin relaxation of electrons in the conduction band. So weak interaction between the spins of the electrons in the conduction band and the spins of the Mn ions take place, which may have consequences for the application of (Ga,Mn)As in spintronic devices.[58-63].

3.2.1.Theory of Optically Induced Ferromagnetism in DMS

In the DMS system the free electrons and holes induced by incident light, interact with the localized moments anti-ferromagnetically and there by induce a ferromagnetic interaction between impurity magnetic moments. Behavior of such kind of high-dimensional random systems is studied by using simple approximate models which are averaged over different degrees of freedom. Mean field approximation for spin interactions in a DMS system by calculating free energy in terms of magnetization and then minimizing it with respect to magnetization.

In this article photo induced ferromagnetism in diluted magnetic semiconductors has been studied with the help of Hamiltonian model. Hamiltonian describing diluted magnetic semiconductor where electrons and holes generated by a light field are spin-split through an exchange interaction with the magnetic ions within mean field approximation. The Coulomb interaction includes electron-electron, hole-hole and electron-hole interactions. The semiconductor-light interaction is

considered such that an electron-hole pair is created by absorption of light or an electron-hole pair recombines by emitting light. The overall Hamiltonian of the DMS systems is obtained by solving Schrodinger equations for different interactions. [63-74]

The free energy of the system can be obtained by using magnetic analogue of thermodynamic identity

$$F = H - \mu N_h \tag{3-11}$$

Where H is Hamiltonian & $\mu = \hbar\omega$ and N_h is hole density.

Since the system of electrons and holes in contact with the photons has been considered in a steady state, hence the minimized free energy of the DMS system can be calculated as [25,26]

$$F_0 = \left(\frac{2m^*}{\hbar^2}\right)^{\frac{3}{2}} \frac{1}{2\pi^2} \Bigg(\left((\mu' - J\langle M\rangle)^{\frac{5}{2}} + (\mu' + J\langle M\rangle)^{\frac{5}{2}} \right)/5 + \left(\left((\hbar\omega - \mu' + J\langle M\rangle)(\mu' - J\langle M\rangle)^{\frac{3}{2}} \right) + \left((\hbar\omega - \mu' - J\langle M\rangle)(\mu' + J\langle M\rangle)^{\frac{3}{2}} \right) \right)/3 - \hbar\omega \left((\mu' - J\langle M\rangle)^{\frac{3}{2}} + (\mu' + J\langle M\rangle)^{\frac{3}{2}} \right)/3 \Bigg) \tag{3-12}$$

Where $\mu' = \hbar\omega - E_g$ and $2m^*/\hbar^2 = 2m_e\tilde{m}/\hbar^2$ =0.1/3.81 eV.A2 . [67,68,69]

3.2.2.Calculation of Photo-Induced Magnetization

Using Mean-field theory effective magnetic field experienced by a single magnetic moment M due to the rest of the moments is given as

$$H_{eff} = -\frac{\partial F_0(M)}{\partial M} \tag{3-13}$$

Thus, the self-consistent equation for magnetization to be solved is

$$\langle M(T)\rangle = g\mu_B \frac{\sum_{S=-5/2}^{5/2} S e^{-\beta H_{eff} S}}{\sum_{S=-5/2}^{5/2} e^{-\beta H_{eff} S}} \tag{3-14}$$

Where $\beta = 1/kT$ and S=5/2 because Ga has 5-d electrons. The above equations are solved self-

consistently for a given temperature using the free energy expression and calculated magnetic field. By expanding the magnetization near Tc, the analytical expression of Tc in the limit of $V_O \rightarrow 0$ is given by

$$kT_c = \frac{4J^2cS(S+1)}{3g\mu_B}$$

Where S is carrier spin, c is carrier concentration g is Lande-factor, μ_B is bohr magnetron and J is coupling coefficient.

3.2.3.Simulation Parameters

In this article calculations for photo-induced ferromagnetism has been carried out by using free energy expression and mean field theory. Subsequently numerical simulation has been carried out for understanding dependence of various physical quantities such as doping concentration, temperature, light energy etc.

Various parameters which have been considered for calculation of free energy & magnetization are [66,67,69]

$\mu' = \hbar\omega - E_g$ Net Chemical Potential

λ is strength of light coupling to electron or holes which has been varied between 0.1eV – 2.5eV covering visible & IR region

$J = J_e - J_h = 34eV.\text{Å}^3$

$x\ is\ concentration\ of\ Mn\ atoms\ \approx 0.1$

Lattice constant of GaMnAs (a)= 5.65 Å

Concentration of Mn atoms = $\frac{x}{a^3/4} = 0.022x\ /\text{Å}^3$

Apparent mass of interacting carriers $m^* = \frac{m_e m_h}{m_e + m_h} = 0.1m_e$

Strength of contact interaction between photo-generated carriers (U_0) = 1200 eVÅ^3 [67,70].

3.2.4.Results & Discussion

The effect of light coupling λ on free energy as a function of magnetic moment, other parameters of the system remaining constant has been shown in Figure 3-4. For particular light coupling the free energy decrease as a function of the average Mn magnetic moment and free energy increased as function of magnetic moment if the light coupling decreased. When λ = 0(no coupling of light to particles) or when energy of light is below the energy gap there is no excitation of electron and hole.

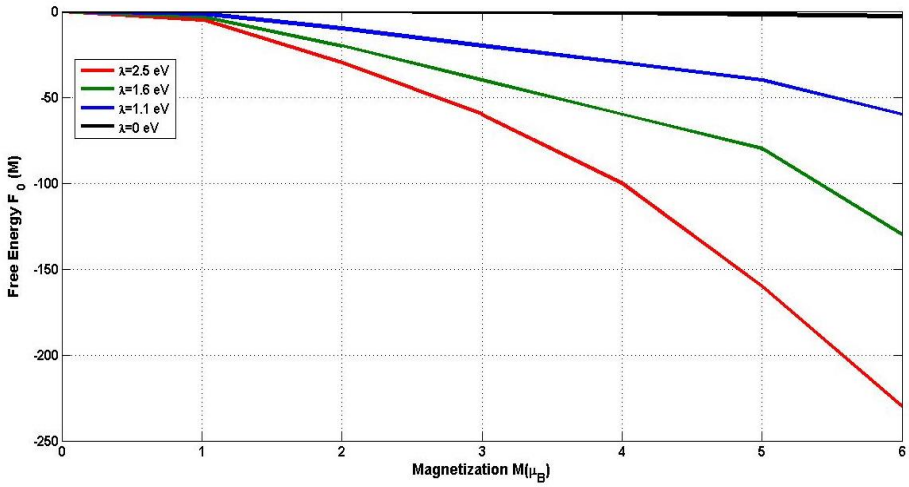

Figure 3-4: Free energy as a function of magnetic moments(M) for different values of light coupling λ (in eV)

The variation of the magnetic moment as a function of temperature for different values of λ and magnetic concentration as keeping other parameters fixed shown in Figure 3-5. The figure shows a phase transition from paramagnetic to ferromagnetic state as temperature decrease. With increase in the light coupling more and more electron- hole pairs are created, thereby increasing the magnetization and hence the critical temperature is increased. But more increasing light coupling there is decrease in the critical temperature. This is due to the competition between particle-particle interaction and the light energy of the system.

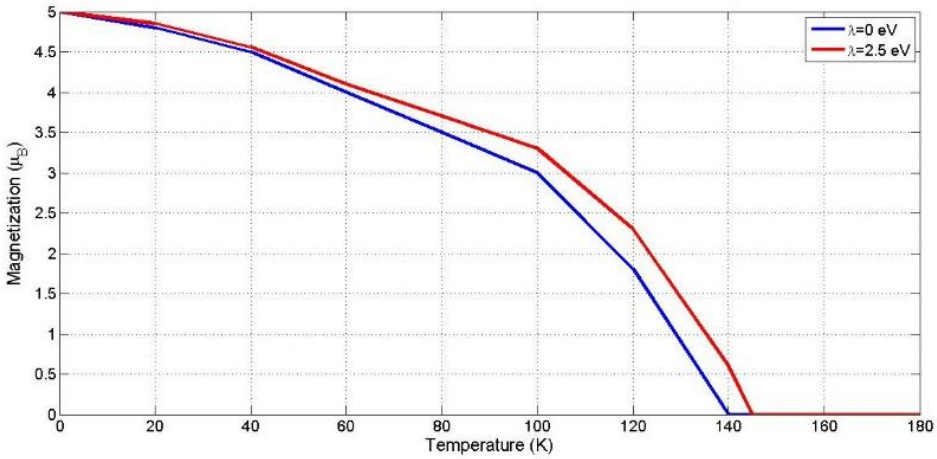

Figure 3-5: Magnetization M(T) as a function of temperature T for different values of light coupling (in units of eV) keeping concentration of magnetic impurity fixed

A small amount of Mn ions incorporated into GaAs/ZnO provides itinerant holes that modify the valence–band structure of the host material and mediate the coupling between the localized spins, giving rise to ferromagnetism. Recently, strongly ferromagnetic GaMnAs/ZnMnO films are being grown using MBE at low temperatures with concentrations up to 9% and despite steady progress, T_C of only up to 173 K . However theoretical critical–temperature calculations based on the kinetic–exchange model predict room–temperature ferromagnetism in (Ga,Mn)As/ZnMnO with 10% substitutional Mn content[69-71]. However, the current T_C record cannot be broken until DMS material with a higher concentration of substitutional Mn ions can be grown.

3.2.5.CONCLUSION

The analysis of Photo-Induced Magnetization in Transition Metal doped Group III-V Dilute Magnetic Semiconductors using Mean Field theory revealed that free energy of TM doped DMS system decreases with magnetization when energy of incident light is increased. The simulation results for magnetization of Mn doped GaAS based DMS system revealed that curie temperature is increased when energy of coupling light & doping concentration of Mn is increased.

3.3. Theoretical study on magnetism in Mn Doped ZnO

The magnetism in the ZnO-based DMSs under both *n*- and *p*- type carrier doping treatment has been investigated using calculations based on the local density approximation [72, 73]. With the exception of Mn, transition metals Cr, Co, and Ni-doped ZnO show ferromagnetism with concentration ranging from 5 to 25%,. The results show that ferromagnetism was induced by hole doping in the Mn-doped ZnO, but found no effect of electron doping. In (Zn,Mn)O, the Mn impurity has a d^5 electron configuration due to the substitution of Zn^{2+} by Mn^{2+} ion, so that there is no itinerant carrier. In this case, it is suggested that the antiferromagnetic super-exchange interaction between Mn ions stabilizes the spin glass state. On the other hand Cr^{2+}, Co^{2+}, and Ni^{2+} have d^4, d^7 and d^8 electronic configurations, respectively. In the case of Cr, one 4*s* electron and one 3*d* electron precipitate in bonding in the II–VI divalent environment and is therefore left in the $Cr^{2+}(d^4)$ state. Therefore, the 3*d*-band of up-spin states or downspin states in these elements is not fully occupied. In mean-field theory and other theories, ferromagnetism arises from a competition between the double exchange interaction and the antiferromagnetic super exchange interaction in these materials. When ZnO:Mn is doped with nitrogen ($1s^2 2s^2 2p^3$), holes are itinerant in keeping with their *d*-character due to the large hybridization of the N-2*p* states with the Mn-3*d* states. Therefore, the kinetic energy is lowered so efficiently that the ferromagnetic state is stabilized by the double exchange mechanism. On the other hand, when the system is doped with donors, the doped electrons never go into the Mn-3*d* states but into the host conduction band, therefore, the double exchange mechanism does not act to stabilize the ferromagnetism in (Zn,Mn)O. As suggested by other principle calculations the curie temperature of Co & Ni doped ZnO can be increased by *n*-type doping when the effects of disorder are taken into account by the coherent potential approximation (CPA) [73]. Considering that the *n*-type ZnO is readily available and the intrinsic defects such as O vacancies and Zn-interstitials form donor states, it is concluded that (Zn,Co)O and (Zn,Ni)O are promising candidates for high-TC ferromagnets & may show carrier induced ferromagnetism with electron doping by tuning the ratio of Mn to Co or Ni. This point might warrant experimental investigations and requires specific designs for ferromagnetism. The ferromagnetism above room temperature was also observed experimentally in both bulk and thin film forms of Zn1-*x* Mn*x*O with $x < 4\%$ [74]. The local spin density approximation and coherent potential approximation used in the first principles calculation may not be adequate to

handle the strong correlation and lattice relaxations. This is particularly so for thin films prepared by different deposition techniques under non-equilibrium conditions.

Based on the first-principles spin-density functional calculations, Lee and Chang [75] also found that electron doping stabilizes the ferromagnetic ordering in Co-doped ZnO, but the ground state is spin glass without doping due to the short range interactions between the transition metal atoms. High electron concentrations and high Co concentrations are necessary to induce ferromagnetism in (Zn,Co)O.

Wang *et al*. [76, 77] used first principles calculations based on the density functional theory and GGA for exchange and correlation to calculate the total energies of a (Zn,Mn)O (1010) thin film with Mn substituted at the Zn site. The thin film was modeled by a slab consisting of eight layers. Different configuration of Mn substitution of Zn sites were chosen so that the Mn-Mn separation as well as their nearest neighbor environment vary. In the dilute limit when Mn atoms are far apart, the system will display paramagnetic behavior. As the Mn concentration increases, Mn atoms tend to come close to each other and cluster around the O atom. This leads to exhibition of antiferromagnetic behavior. The ground state of Mn doped ZnO (1010) thin film changes from antiferromagnetic to ferromagnetic when codoped with N. The calculation of the density of states (DOS) showed the distinct overlap between Mn 3*d* and N 2*p* states in the spin-up bands which leads to significant DOS at the Fermi energy and hence to the half-metallic character of N codoped (Zn,Mn)O system. Doping with N atoms introduces carriers, and Mn and N atoms prefer to exist as nearest neighbors in ZnO. The magnetic moment of Mn polarizes the spins at the neighboring N sites antiferromagnetically, which results in a ferromagnetic coupling between the Mn atoms. The spin alignments of the Mn atoms and the interlocking N atoms can be shown as Mn(↑)–N(↓)–Mn(↑), indicating that ferromagnetism is mediated through the *p-d* exchange interaction between the carriers and Mn atoms. The energy difference between the antiferromagnetic state (AFM) and ferromagnetic (FM) state due to N doping is shown in Fig. 3-6. The maximum energy difference for 25% N doping is ~0.10 eV/Mn atom. The high N concentration used in the model, i.e., from 6.25 to 25%, however, may be a challenge from a synthesis standpoint.

Our work is focussed toward study of ferromagnetism in Mn doped ZnO at high temperatures. However, there is still much debate about origin of the room temperature ferromagnetism in $Zn_{1-x}Mn_xO$. The doping of ZnO with Mn does not introduce carriers into the system so the system is expected to be antiferromagnetic, because Mn spin-up and spin-down electrons have equal DOS at Fermi energy. With the addition of holes into the system the system becomes ferromagnetic because strong hybridization of the spin-up 3d states of Mn hybridize with the N 2p (hole) states at Fermi energy, exchange splitting of the spin-down 3d states no hybridization with the p states of N.

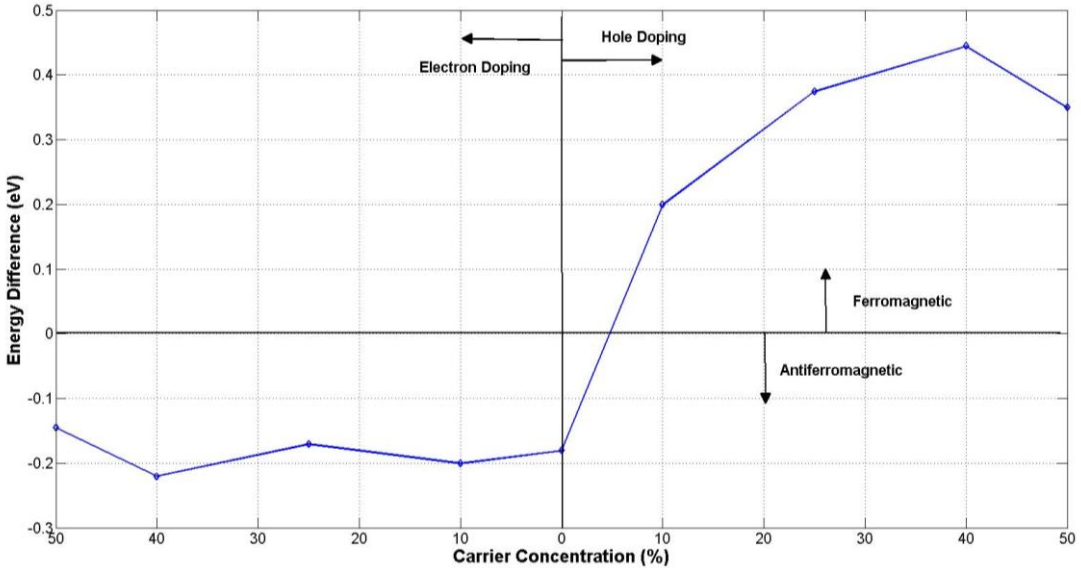

Figure 3-6 : Plot for Energy Level Difference (E(Hole Doping)-E(Electron Doping) (eV)) vs carrier concentarion

The curie temperature for Mn doped ZnO is calculated by Coey's two sub-lattice model [27-28] for TM doped ZnO

$$T_c = \frac{\left[\frac{S(S+1)s^2 x\delta n}{3}\right]^{\frac{1}{2}} J_{sd}\omega_c}{k_B} \qquad (3\text{-}16)$$

ω_c is the product of cation/anion volume ratio, **S**=5/2, **s**=1/2 & n = 1, n_O = 6.1028 m^{-3}, x = 0.1, J_{sd} is ferrormagnetic exchange coupling coefficient which is calculated by blue-shift in ZnO bandgap for Mn Doping. Curie tempearture for Mn doped ZnO is found to be near 250K.

3.4. Band structure of ZnO

The band structure is a very important property of a semiconductor, because many important properties and parameters are derived from it, e.g. band gap and effective masses of electrons and holes. Complete understanding of band structure of ZnO is very important for explaining the electronic properties & exploring its usage in semiconductor devices. The study of band structure helps to establish the relationship between the energy and the momentum of the carrier. Bandgap calculation involves solution of the Schrödinger equation using the crystal Hamiltonian [78,79]. Determination of crystal Hamiltonian requires calculation of energy of electrons & nuclear structure. The Schrödinger equation can be solved in many ways some of which are listed below

a. perturbation theory:
b. tight binding approximation for linear combinations of atomic/molecular orbital's [80];
c. using pseudo potentials [79];
d. using Green's function techniques [81].

Using Perturbation theory, the final energy solution can be computed by using the smaller Hamiltonian terms. The major parameters associated with Coulomb interaction with the nuclei can be used for determining the basic states for perturbation. However in present time, there are many experimental techniques which can be used for determining the band structure of ZnO.

UV & X- ray absorption /reflection /emission techniques can be used for calculating the electronic core levels in solids. The basic principle of these methods is energy difference measurement by induced electron transistions such as transition from the upper VB states to the CB states etc.. Secondly the energy difference can also be measured by excitation of collective modes. Photoelectron spectroscopy is another method for the investigating band structure & it is based on the photoelectric effect [30]. Recently, angle-resolved PES technique has been used [72], in conjunction with excitation from synchrotron radiation, which can be used as a powerful tool for computation of electronic band-structure for bulk and surface.

The electronic band structure (E(k)) of bulk ZnO has been shown in figure 3.2. It has been generated using theoretical models using an empirical tight-binding Hamiltonian. It has high symmetry lines in the hexagonal Brillouin zone [82,83]. In the band gap (energy difference between the full and empty electron states) of bulk ZnO the most important thing which can be

noticed is the optical band gap between the occupied bands and the empty bands. The value of this band gap, Eg, is approximately 3.3eV. The energy states which are completely filled are known as valence band . The conduction band includes energy states which are empty & lie above the band gap. The lowest energy point of conduction band (conduction band edge) lies at k = 0. The highest energy point at top side of valence band is known as Γ point, which is also the k-value. Since the valence band and the conduction band edges occur at the same k-values for ZnO, hence it is known as a direct band gap semiconductor [84-85].

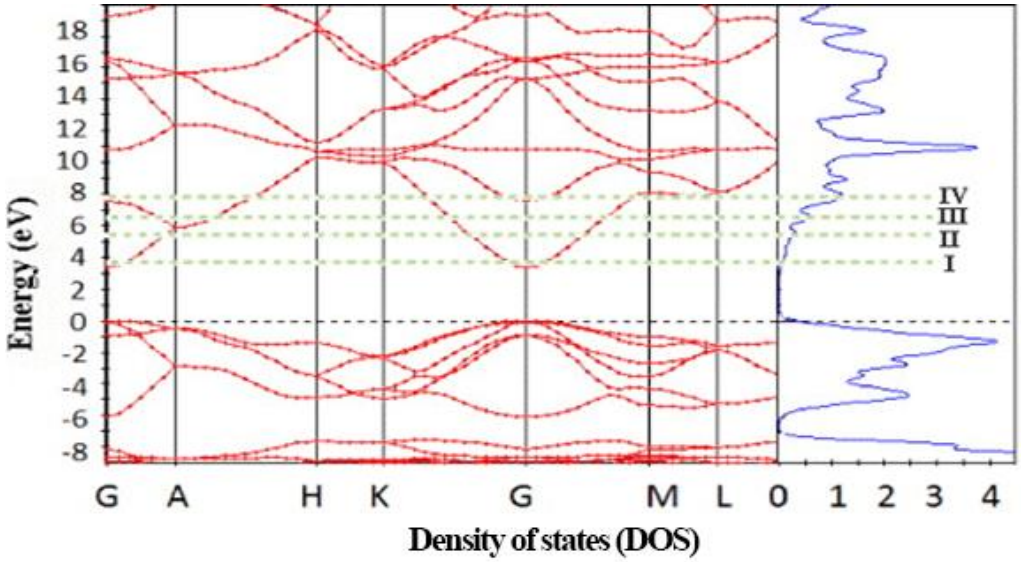

Figure 3-7 : Band structure of ZnO. (The zero in a graph is taken as the valence band)

The lowest CB is formed from the empty 4s states of Zn^{2+} or the anti-binding sp^3 hybrid states and the VB originates from the occupied 2p orbitals of O^{2-} or the binding sp^3 orbitals. Under the crystal field and spin orbit interaction, the valence band is split into three sub-VB of symmetries, which are labelled in all wurtzite-type semiconductors from high to low energies as A, B, and C bands. In most cases, the ordering of the bands is $A\Gamma_9$, $B\Gamma_7$, $C\Gamma_7$. However, for ZnO there is a long debate whether the ordering as usual. The relation between the band gap and temperature dependence up to 300K is given by

$$E_g(T) = E_g(T=0)\frac{5.05 \times 10^{-4} \times T^2}{(900 - T)}$$

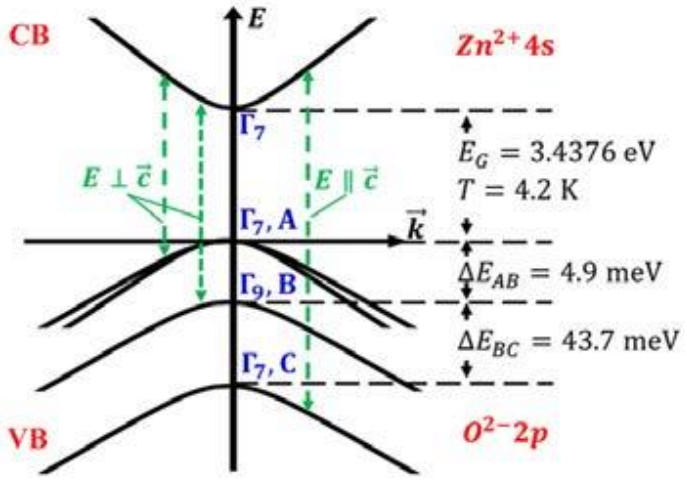

Figure 3-8: *The valence band (VB) and conduction band (CB) of ZnO in the vicinity of the fundamental band-gap.*

3.5. Electrical properties

The pure ZnO semiconductor exhibits n-type conductivity which may be attributed to lattice defects (vacancies and interstitials). As described earlier, ZnO is a direct wide band gap semiconductor having large exciton binding energy, which make it very attractive for many electronic and optoelectronic applications. This is because of the fact that wide band gap semicond may have high breakdown voltages, ability to sustain very high electric fields, lower noise generation, and ability for high power operation. However the electron flow in zinc oxide is very low even at high electric fields. Whereas at low electric fields the energy gained by the electrons is tiny as compared to the thermal energy. Hence, the energy distribution of electrons in the ZnO lattice is unaffected by applying low electric field. Therefore, the it obeys the ohms law because the electron mobility remains independent of electric fields. When magnitude of electrical field is increased upto the point where energy gained by electrons from the applied electrical field becomes comparable to the thermal energy. Then the distribution of electrons changes significantly and these electrons now become hot electrons because they have higher temperature than the lattice temperature. Hence, there is no energy dissipated to the lattice during critical time and when drift velocity of an electron is more than its steady-state value, a higher frequency device can be fabricated [86, 87].

3.6. Optical properties of ZnO

The optical properties of a semiconductor are closely related to the intrinsic and extrinsic parameters. The intrinsic optical properties depends on the interactions between electrons & holes from valence band (VB) & conduction band (CB). They also includes excitation effects caused by the electrostatic interaction. The extrinsic optical properties are mostly related to dopants or defects present in the semiconductor lattice structure. The dopants or defects generate discrete electronic states between conduction band (CB) and Valance Bands (VB). Optical properties in ZnO have been investigated by different experimental techniques which include optical transmission & absorption, reflection, photoluminescence (PL) & cathodoluminescence (CL) etc. The photoluminescence (PL) technique have been used much extensively for studying the optical properties of ZnO based semiconductors. The room temperature PL spectrum of ZnO exhibits emission of Ultra Voilet (UV) light & some visible emissions which might be induced by defects, vacancies due to missing atoms in some lattice positions, interstitials (extra atoms occupying interstices in the lattice), antisites (a Zn atom swaps it's location with an O vice versa) and complex defects [88]. Zinc oxide (ZnO) exhibits a direct wide band-gap of 3.3 eV with very high exciton energy of 0.06 eV at room temperature. The exciton binding energy of ZnO is much larger than that of GaN (25 meV), and the thermal energy at room temperature (26 meV), due to which an efficient exciton emission occurs at room temperature. Hence, ZnO can be a promising photonic material in the blue-UV wavelength region . For ZnO nanorods, photoluminescence spectroscopy has been widely used to investigate the optical properties, which provides information such as band gap, defects, and crystal quality. The photoluminescence (PL) investigation of ZnO nano particles revealed a near band edge (NBE) UV emission and a deep level emission (DLE) which may be attributed to deep level defects. Single UV emission have been observed in pure ZnO nanorods with very low impurity concentrations. This emission can be attributed to the NBE emission of ZnO .The DLE emission in visible range can be attributed to lattice defects in the ZnO nanostructure such as vacancy, interstitial and impurities. The optical quality of the ZnO can be indicated by relative intensity between the NBE emission and DLE emission. A large ratio of the INBE/IDLE means a lower concentration of the deep level defect [88-89].

4. EXPERIMENTAL TECHNIQUES FOR SAMPLE PREPARATION & CHARACTERIZATION

In this chapter, we will describe various techniques for sample preparation and their characterization. The structural as well as morphological properties of pure as well doped oxide samples can be characterized by scanning electron microscopy (SEM), field emission SEM (FESEM), transmission electron microscopy (TEM) and X-Ray Diffraction (XRD). Chemical composition of the materials can be analyzed by using energy dispersive electron diffraction (EDX) and x-ray photoelectron spectroscopy (XPS). Optical properties are measured by ultraviolet-visible (UV) absorption spectroscopy and photoluminescence (PL) spectroscopy. Magnetic properties are measured using vibrating sample magnetometer (VSM) and superconducting quantum interference devices (SQUID) and magnetic force microscope (MFM) attached with atomic force microscopy (AFM) unit. Resistivity of the thin films is measured by four probe method and carrier concentration is estimated from hall measurement.

4.1. Synthesis of ZnO and doping with Transition Metal Ions

Thin films can be grown using physical as well chemical deposition techniques. Physical Vapor Deposition (PVD) methods are based on the formation of a vapor phase from a solid source material, and the following condensation on a substrate surface. Atoms and/or molecules making the vapor phase are physically extracted from the source material. This extraction process can be pursued by using various sources of energy, each one characteristic of the particular deposition method. For example, the presence of plasma is required for sputtering process, while high-energy photons coming from a laser source are exploited in the case of pulsed laser deposition (PLD). The formation process of thin films may be roughly summarized into the adsorption, nucleation and coalescence steps. The first one deals with the adsorption of atoms and/or molecules, coming from the vapor phase, on a substrate surface (adatoms). This process is driven by physisorption, i.e., weak electrostatic interactions due to Van der Waals forces, and/or chemisorption, i.e., formation of strong chemical bonds between atoms and the surface. After adsorption, nucleation and coalescence steps take place. In such situations, different adatoms start to aggregate together (nucleation), resulting in the formation of islands. These can further increase in dimensions and

coalesce together, finally leading to the formation of a continuous thin film network that cover the whole substrate surface, if desired. Depending on the specific deposition parameters, each of the abovementioned steps can be properly influenced to promote the growth of island separately, avoiding the formation of a compact film.

4.1.1 Sputtering

Sputtering and sputter deposition are widely used techniques for the erosion of surfaces and the deposition of films. Sputtering is a plasma-assisted PVD process where collisions between high-energy ions and the source material (target) are exploited for the formation of a vapor phase. Plasma is obtained by injecting a noble gas (usually argon) into the deposition chamber which is ionized by the application of a proper direct-current (DC)/radio-frequency (RF) signal voltage between a cathode, where the target is clamped, and the rest of the chamber. The impinging of ions on the target surface allows the extraction of atoms. Once the vapor phase is formed, condensation on the substrate surface takes place and thin-film formation may be pursued by the following nucleation and coalescence steps. Sputtering technology has been widely investigated because of its multiple advantages, as it is a high-yield production technology, compatible with integrated-circuit processing, and allows for the homogeneous deposition of materials on wide-area substrates. Substrates are placed in a vacuum chamber and are pumped down to a prescribed process pressure. Prior to the sputtering coating process, a vacuum of ~ 10^{-5} mbar was achieved. Once the appropriate pressure has been reached, a controlled flow of an inert gas such as argon is introduced. Sputtering starts when a potential difference is applied between the target and substrate holder causing a plasma or glow discharge. The negative terminal is connected to the target material. Positively charged gas ions generated in the plasma region are attracted to the negatively biased target plate at a very high speed. This collision creates a momentum transfer and can eject atomic size particles from the target. If the energy transferred to a lattice site is greater than the binding energy, primary recoil atoms can be created which can collide with other atoms and distribute their energy via collision cascades. A surface atom becomes sputtered if the energy transferred to it normal to the surface is larger than about three times the surface binding energy (approximately equal to the heat of sublimation). These particles are deposited as a thin film on the surface of the substrates. A Schematic diagram of the mechanism of sputtering process is shown in Fig. 4.1.

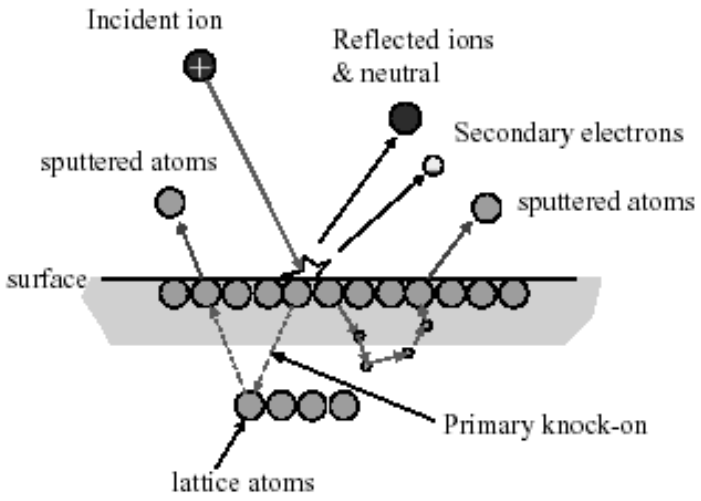

Figure 4-1 : Diagram showing mechanism of Sputtering

When the atomic weight of the sputtering gas is close to the atomic weight of the target, the momentum is transferred efficiently. Hence, Neon gas is preferred for sputtering of light elements, whereas krypton or xenon are used for heavy element targets. Reactive gases can also be used to sputter compounds. The thin film compound can be grown on the target surface or on the substrate, based on the selected process parameters.

Magnetron sputtering can be done either in DC or RF (radio frequency) modes. DC sputtering is done with conducting materials. If the target is a non conducting material, the positive charge will build up on the material and it will stop sputtering. In such a situation, RF sputtering is employed [90]. In magnetron sputtering which has almost no restrictions on target materials, magnets are used to increase the length of the electron path, thereby increase the probability of electrons striking the Argon atoms, and hence increase the ionization efficiency significantly. A schematic diagram for RF magnetron sputtering deposition technique is shown in Fig. 4-2

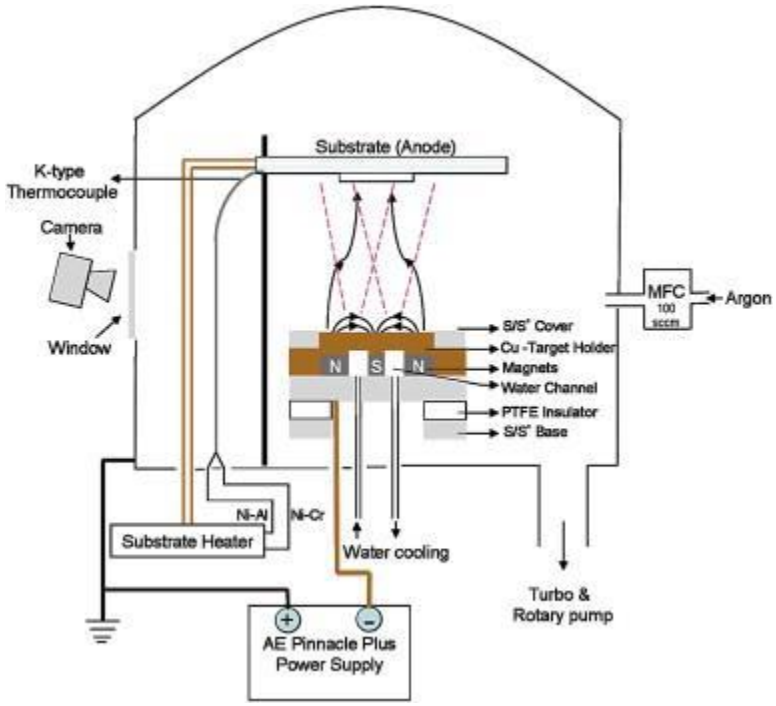

Figure 4-2: Diagram of RF Magnetron Sputtering Unit

4.1.2. Pulsed Laser Deposition

The technique of PLD has been used to deposit high quality films of materials for more than a decade [92]. In the pulse laser deposition technique very high power laser pulses with power of the order of ~10^8 Wcm^{-2} are used for melting, evaporation & ionization of the material from the surface of a target. This process is known as "ablation" & it produces a highly luminous plasma plume which rapidly expands away from the target surface. The plasma plume carrying material is collected on suitable substrate which is place at appropriate location. At the substrate, the plasma plume condenses and the thin film starts growing. Applications of the technique range from the production of superconducting and insulating circuit components to improved wear and biocompatibility for medical applications.

In principle PLD is an extremely simple technique, which uses pulses of laser energy to remove material from the surface of a target, as shown schematically in Fig. 4-3. The vaporized material, containing neutrals, ions, electrons etc., is known as a laser-produced plasma plume and expands rapidly away from the target surface (velocities typically ~10^6 cms^{-1} in vacuum). Film growth occurs on a substrate upon which some of the plume material re-condenses. However, the

condensation process is not that simple. In a practical scenario large number of process variables affects the properties of the film, such as laser flux, pressure of background gas and temperature of the substrate. These variables can be manipulated upto some extent for controlling the properties of thin film according to application requirements. However, optimization can require a considerable amount of time and effort. Indeed, much of the early research into PLD concentrated on the empirical optimization of deposition conditions for individual materials and applications, without attempting to understand the processes occurring as the material is transported from target to substrate.

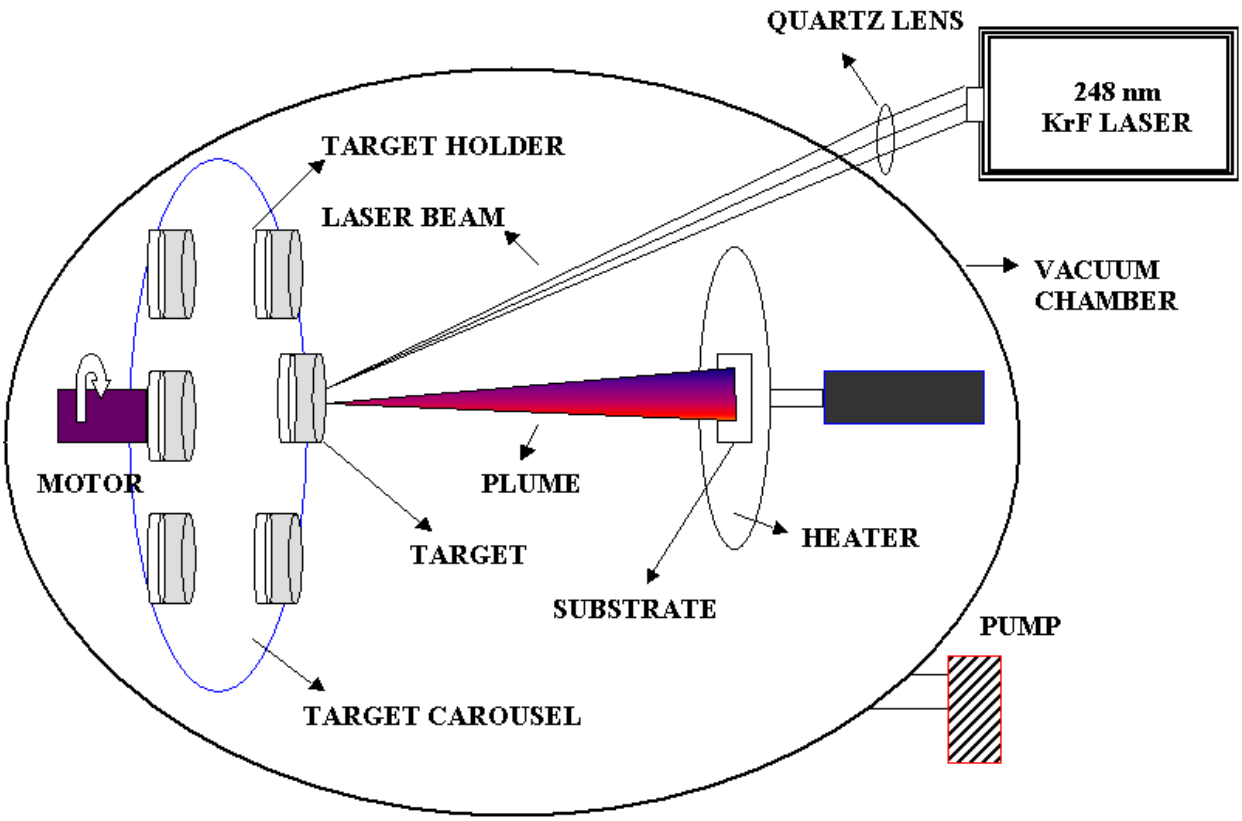

Figure 4-3 : Schematic Diagram of PLD

The Pulsed Laser Deposition technique have significant benefits over other film deposition methods, which include

(i) It have capability of transferring exact stoichiometry (chemical composition) of material from target to substrate

(ii) This technique has high deposition rates as compared to other techniques which are of the order of ~100s Å/min. These deposition rates can be achieved at moderate laser flux & thickness of thin films can be controlled in real time by turning the laser on/off.

(iii) Aslaser is used as an external energy source & inert gas in background due to which this process is very clean without need of filaments.

(iv) This technique provides the flexibility of growing multilayer thin films.

4.1.3. Spray Pyrolysis

Spray pyrolysis is a well-established technique used for preparing high-quality thin and thick ZnO films in a very simple, cheap and easy way. This synthetic approach allows for growing both dense and porous films, as well as powdered materials. The process roughly consists in three steps: atomization of a metal salt precursor solution, transportation of the resulting vapors, condensation of the drops and their thermal decomposition on a heated substrate. The formation of a thin film network is then obtained by the superimposition and overlap of the metal salt drops over the substrate surface, and their conversion into oxides by heating of the substrate. The main parameters affecting the final thin-film structure and properties are the solvent, type of salt and concentration, and additives present in the precursor solution. Porous crystalline ZnO films obtained by spray pyrolysis have been reported in numerous cases. The precursor solution generally consists of zinc acetylacetonate , zinc nitrate , or zinc acetate dehydrate salts dissolved in aqueous solution. In all the cases it was found that both the use of different precursor concentrations, substrate temperatures or post-deposition thermal annealing treatments strongly influenced the resulting film morphology, photoconductive and photoluminescent properties. The porous ZnO structures resulting from spray pyrolysis method generally showed good electrical conductive properties and light transparency. These aspects, coupled to optimal dye absorption properties, demonstrated their promising use as photoanodes in DSSCs fabrication . Moreover, their application as blocking layer (BL) in standard TiO2-based solar cells has been successfully reported; the presence of spray-pyrolysis derived porous ZnO BL effectively reduced charge carrier recombination phenomena, improving the cell efficiency more than 20% with respect to cells efficiencies obtained without the BL . Most of the applications based on ZnO films obtained by spray pyrolysis also rely on the fabrication of gas sensors. Several works gave evidence of their promising use as gas sensors for the detection of various gas species, including acetaldehyde, ammonia and H_2S. In these cases, the room temperature sensing characteristics showed that gas concentrations ranging from

hundreds of ppm up to few ppm could be successfully detected with good selectivity and fast response/recovery times. In addition, other gases like methanol, ethanol, 2-propanol, benzyl alcohol and acetone were considered, further proving the best selectivity of such porous ZnO structures towards those abovementioned gases [93-94].

4.1.4. Electrodeposition

Electrochemical deposition, also called electrodeposition, is a versatile, low cost, easy and scalable method, particularly useful for growing highly porous ZnO thin films at relatively low working temperatures generally lower than 100 ^{o}C). This method deals with the use of charged reactive species diffusing through a solution, under the application of an external electric field. Electrodeposition is carried out in a three-electrode electrochemical cell, composed by a reference electrode (Ag/AgCl), the counter electrode (platinum wire or sheet), the working electrode and the electrolyte solution. The application of a constant voltage between the electrodes allows the diffusion of reactive species within the electrolyte solution.

Depending on several deposition parameters, like the applied voltage, deposition time, charge density and solution precursor, the porosity and morphology of electrodeposited ZnO films may be tuned, accordingly. For example, it has been reported that the growth rate of ZnO films showing different porosities and morphologies prepared by cathodic electrodeposition was influenced by sodium lauryl sulfate concentration. This surfactant was added to the growth solution, made of aqueous oxygen saturated zinc chloride and other organic acids. If sodium laurylsulfate concentration was high enough, formation of micelles and their assembly on the charged electrode surface could be achieved, allowing for the formation of the porous structure, but also leading to a strong increase in the current density and finally, to the growth rate . The promising optical and electrical properties of porous ZnO films obtained by electrodeposition have been reported in numerous cases. In particular, it was found that enhanced photocurrent values were due to a combination of multiple effects dealing with improved visible absorption properties, optimization of oxygen defects within the crystal structure, and finally the presence of an appropriate porous surface morphology, allowing for the incoming light to more effectively generate multiple reflections and diffusion scattering effects before being emitted, finally increasing the ZnO solar light absorption properties. Such a pronounced photocurrent, coupled with a porous morphology, was successfully exploited for the fabrication of sensors and DSSCs [95]. Also in this case, the

addition of surfactants during ZnO electrodeposition turned out to be an effective way for inducing high porosities and fast growth rates. The resulting porous samples displayed a persistent photoconductive behavior, which conductivity transients of several hours in dry atmosphere, independently of illuminating conditions. More interestingly, the photoconductive behavior was observed even when illuminating with low-bandgap energy light. This property was explained in terms of lattice relaxation processes involving surface states within the ZnO bandgap, which favored capture of electrons immediately after photoexcitation phenomena.[96]

4.1.5.Chemical methods

Chemical vapor deposition is one of the most popular techniques which is used for growing high-purity, high-performance thin films of solid materials. This technique is often used in the VLSI industry to produce thin films of semiconductors etc.. In the chemical vapor deposition technique, the substrate wafer is exposed to one or more volatile precursors chemical compounds, and the precursors react & decompose on the surface of the substrate thin film is produced. In the deposition process by-products are removed by gas flow from chamber. The main differences in these processes are the mechanism by which chemical reactions are initiated and process conditions. The classifications of chemical vapor deposition based on operating pressure, physical characteristics and plasma as follows.

1. **Classification by operating pressure:**
    - Low-pressure chemical vapor deposition (LPCVD) – in this technique deposition processes is performed at low pressures.
    - Atmospheric pressure chemical vapor deposition (APCVD) – in this technique deposition processes is performed at atmospheric pressure.
    - Ultrahigh vacuum chemical vapor deposition (UHVCVD) – in this technique deposition processes is performed in vacuum.
2. **Classification by physical characteristics:**
    - Atomic layer chemical vapor deposition (ALCVD) – In this technique multiple thin layers of different substances are deposited for synthesizing crystalline films.
    - Combustion chemical vapor deposition (CCVD) – It is chemical flame-based technique which is used for depositing pure & crystalline thin films in presence of air.

- Hot wire chemical vapor deposition (HWCVD) – this technique uses hot filament for decomposing the source gases & thin film deposition. Hence it is also known as hot filament chemical vapor deposition. [10].
- Hybrid Physical-Chemical Vapor Deposition(HPCVD) – this is a chemical process in which solid source is vaporized & precursor gas is decomposed for thin film deposition.
- Metal organic chemical vapor deposition (MOCVD) – this technique is used for depositing high purity thin films of materials using metal organic precursors.

4.1.6. Chemical Bath Deposition (CBD) method

The chemical bath deposition technique is another popular technique for thin films deposition. It is one of the cheapest methods, as it does not require any saphosticated equipments. It can be easily scaled for large scale production. This technique was first introduced by Bruckman for depositing Lead sulphide (PbS) thin film in 1933.

The chemical bath deposition technique is cheapest because it requires only solution containers and substrate mounting devices. However, in this technique lot of solution gets wasted after every deposition process which is among one of its major drawback. The thin film produced by this technique are uniform, stable and adherent. However, the growth quality depends on environmental conditions, such as time duration of deposition, composition of solution and temperature of the solution, and substrate topography and chemical nature.

The chemical bath deposition involves four steps.

(1) Equilibrium between complexing agent & water.
(2) Formation/dissociation of ionic metal-ligand complexes.
(3) Hydrolysis of the chalcogenide source
(4) Solid thin film formation

The chemical kinetics of the hydrolysis process is very sensitive to the pH value and temperature of the solution. Also the catalytic effects of solid materials control the rate of deposition. However, rate of deposition may be controlled by formation of complexed metal ions. These steps together determine the composition, growth rate, lattice structure and surface topography of the thin films.

4.1.7.Sol-Gel Technique

The sol-gel process is another thin film deposition technique which is very popular among researcher because of being simple & cheap. In this technique, a homogeneous solution of molecular precursors materials (sol) is converted into a 3-dimensional network (gel) by a set of chemical reactions. The homogenous solutions used in sol-gel process consists of a metal alkaloid and an alcohol. In the starting, the alkaloid is subjected to a hydrolysis reaction & then it is followed by condensation & polymerization. After reaction between metal alkaloid & alcohol solution , an gel like oxide network is formed. The oxide network (gel) contains a 3-dimensional skeleton of interconnected pores. This gel of oxide network is dried & a rigid solid thin film is prepared.

In the process of sol-gel synthesis the solution gradually converts into a gel-like dual-phase system which contain both liquid as well as solid phase & which can have morphology of discrete particles or a continuous polymer network. For a colloidal type of solution, the fraction of particles is very low & significant amount of liquid has to be removed for getting a gel-like end product. It can be accomplished by leaving the solution for some time for sedimentation, and then removing the remaining liquid. Remaining solvent can be removed by drying process. In drying process significant amount of shrinkage and densification occurs. The porosity distribution of gel is determined by the rate at which the solvent can be removed.

The reaction rate in sol-gel method depends upon type of precursors systems (binary or ternary), pH of the solvent, concentration and temperature. In a system having single precursor, we can synthesize thin films with nano-scale porosity & a high surface area by carefully selecting process design parameters.[99-100]

The Sol-gel techniques is one of the cheapest methods for synhesizing ZnO thin films. In this approach a colloidal solution is prepared by combining zinc precursor powders (zinc acetate dihydrate, zinc nitrate hexahydrate or zinc chloride) and bases (sodium hydroxide). Then mixture is dissolved in organic solvent (ethanol, methanol or 2-propanol). Also hexamethylene-tetramine is added to the solution for promoting ZnO crystallization and controlling morphology of ZnO thin film. The prepared solution is stirred for few hours at mild conditions (60–70 ˚C) and finally deposited on the desired substrates. To further promote ZnO crystallization as well as the formation of the desired porous morphology, a final sintering process is generally performed for several hours at temperatures ranging between 300 ˚C and 500 ˚C.[97-98]

Sol-gel derived porous ZnO structures show high surface areas coupled with the existence of good optical and electrical properties. All these aspects result into interesting application properties. For example, porous ZnO obtained by CBD exhibited good sensing properties against a wide range of toxic and combustible gases like hydrogen, liquid petroleum gas, methane and H_2S. The response of the ZnO thin film sensors was found to be significant, even for low gas concentrations, i.e., 50 ppm for methane, 15 ppm for H_2S. Highly porous ZnO thin films prepared by a sol–gel approach showed promising photocatalytic properties.

The sol–gel method has emerged as one of the most promising processing route as it is particularly efficient in producing thin, transparent, homogeneous, multi component oxide films of many compositions on various substrates at low cost.

Advantages of Sol-Gel Process

1. Less energy consumption: there is no need to melting temperature to achieve network structure i.e. low temperature processing and consolidation is possible.
2. Smaller particle size and morphological control in powder synthesis.
3. Better homogeneity due to mixing at the molecular level and high purity compared to traditional ceramic method.
4. No need for special or expensive equipment.

Disadvantages of Sol-Gel Process

1. Metal alkoxides are the most preferred precursor. But they are expensive as compared to mineral based metal ion sources.
2. Due to the use of organic reagents in preparative steps, products would contain high carbon content and this would inhibit densification during sintering.
3. Close monitoring of the process is required because multi steps are involved in this process.
4. Moreover, formation of gel is a slow process, which makes sol gel a time consuming fabrication technique as compared to other methods.

4.1.8.Dip Coating Method

In the dip coating technique, first the substrate is immersed in a solution (containing material whose thin film has to be grown) for some time and then withdrawn at a well-defined withdrawal speed under controlled pressure, temperature and other surrounding conditions. The thickness of thin film mainly depends on the speed of withdrawal, viscosity & concentration of the solution.

There are theoretical models which defines the relationship between thin film thickness & dip coating systems. The equations given by Landau-Levich can be used for calculating thin film thickness if withdrawal speed is kept below certain limit. The limiy of withdrawal speed should be chosen such that the sheer rates of system doesn't go beyond Newtonian regime[99].

James and Strawbridge [100] verified the above method for an acid catalyzed silicate sol, by comparing the thicknesses obtained experimentally & theoretically. Selection of viscosity in dip coating process is the most critical part for controlling thickness. Very high precision ranging 20 nm up to 50 μm can be achieved in this technique having excellent optical properties. The dip coating diagram has been shown in figure 4-4.

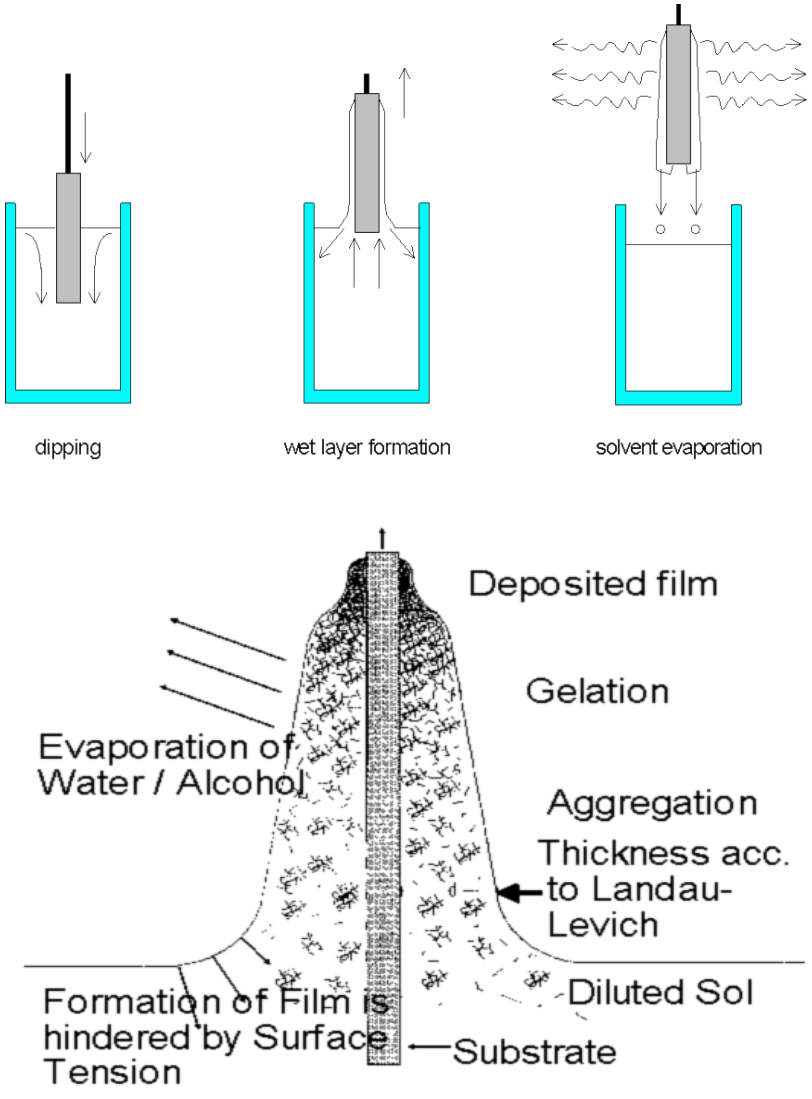

Figure 4-4: Dip coating diagram

4.1.9.Spin Coating Method

Spin coating is another simple & fast techniques for thin film deposition using homogenous solutions. This technique was first introduced by Meyerhofer et al.,[101]. The diagram of spin coating process is given in fig 4.5.

The main steps which are followed in spin coating process are

- The coating fluid depositing onto the wafer or substrate
- Accelerating the substrate up to pre-decided rotation speed
- Spinning of the substrate at a constant rate (because the viscosity dominate the thinning behavior & solvent evaporation dominates the coating behavior)

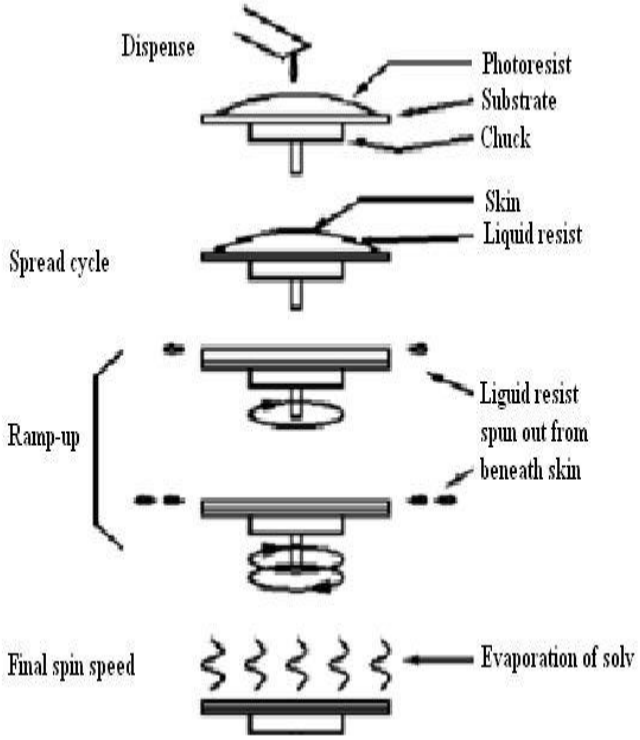

Figure 4-5: Spin coating method

4.2. Selection of deposition techniques

Some of the important aspects for the selection of a deposition technique for the preparation of ZnO thin films are

- Uniformity of layer thickness values over a desired area.

- Consistency of thin films
- The precision of the layer thickness
- The optical quality of the deposited layers.
- The substrate temperature requirement.
- Thin film growth rate.

The sol-gel spin coating method meets all of above requirements & also provides additional advantages such as simplicity, inexpensive, non-vacuum and low temperature. Thin films synthesized using this technique have been used for many applications such as optical coatings, sensors, electro-optic and nonlinear optical films, electro-chromic, semiconducting, anti-static coatings, superconducting films and ferro-electric materials [102]. Within few years, the sol-gel technique even more widespread due to many developments in precursor solutions, coating processes and equipment.

Sol-gel Spin coating method has been very popular low cost technique for thin film preparation because it involves processing of the raw materials at low temperature and fabrication of high quality thin films/ nano powders [103]. This technique is a very attractive method to produce films for spintronic applications. The method is also used for fabricating metal oxide nano materials. So sol-gel spin coating method has been used for synthesizing thin films of pure zinc oxide & TM doped zinc oxide in the present work.

4.3. Selection of substrate & Initial cleaning

Selection of the substrate for thin film deposition is another critical step. Substrate should be mechanically stable & should have thermal expansion coefficient matching with the device material & should remain inert during the device fabrication [104]. The requirements for the substrate material may vary, based on the type of application. In the present study well-cleaned glass slides having 1mm thickness have been chosen as substrates. The main advantages of glass substrates are as follow

1. low surface roughness and flatness values,
2. high thermal expansion coefficient,
3. low insertion loss,
4. high physical properties
5. chemical durability,

6. low cost and ease of availability.

Proper cleaning and preparation of substrate is highly essential for achieving good adhesion quality for thin films. The cleaning and surface preparation has to be done immediately prior to deposition process. If substrates are not cleaned properly then it may lead to loss of adhesion and therefore reduced durability and performance.

Initially the substrate cleaning is performed by distilled water. Then the substrate is gently washed with cotton cloth (soaked in acetone) for cleaning the dirt and residues. After this the glass substrates are immersed into chromic acid solution for 30 min & again cleaned with distilled water and wiped with acetone. [105]. Subsequently the substrate should be immersed into sodium hydroxide solution for another 30 minutes for mild etching of the substrate surface. Finally, the cleaned substrates should be dipped in bi-propanol in the ultrasonic agitator. This process helps dissolution of residues by stirring through shock waves. Through this process the glass substrates becomes well cleaned. Finally the glass substrates should be dried in a hot air oven & can be used further.

4.4. Solvent, Precursors and Stabilizer

As described earlier certain key factors of sol-gel process are reaction time, synthesis temperature, , precursors solvent & stablizer, ultrasonic pre-treatment of the solution mixture etc. The solvent plays an important role in quality of thin films. The properties of solvent affect the preferential direction of crystal growth.

The most common solvents which are used for ZnO thin film preparation are alcohols with low carbon number (<4) such as methanol, ethanol, 1-propanol, 2-propanol and di-methoxyethanol. However 2-propanol is most commonly used as solvent. Whereas other solvents such as 2-methoxy ethanol, is not often used despite its good physical properties. Because it is highly toxic & not recommended by the International community on Chemical Safety.

Several other precursors for preparing ZnO thin films include nitrate, chloride, perchlorate, acetyl-acetonate etc.. Mostly zinc acetate dehydrate is used for growing thin films of ZnO. Usually metal alkoxides offer many chemical advantages but it is sensitive to moisture & is highly reactive. Metal salts are mostly used as precursors in thin film synthesis, because of their low cost & commercial availability. Inorganic salts like nitrates are used for synthesis of ZnO thin films in sol–gel

technique. Using zinc acetate as a precursor has a advantages because the acetate groups which act as contaminants in the oxide gel, decompose by annealing & removed in form of gases[106-107]. Because Zinc acetate has a limited solubility in ethanol and 2-propanol. Hence mono-ethanol amines aids in dissolution process & formation of a stable sol. Further, It also stabilize the process, & avoid the rapid precipitation of zinc hydroxide. However, it has been reported that MEA solution facilitates the c-axis growth of ZnO thin films.

4.5. Structural Characterization and measurement techniques

The study of structural information of a material is highly necessary for understanding the nature of the materials and helps in correlating the different physical properties of the material. For understanding magnetic behavior of the diluted magnetic semiconductor (DMS), it is essential to study structural properties of thin films. A brief description on experimental techniques for structural characterization used in this study is as follow

4.5.1. X-ray diffraction

X-ray diffraction techniques are a family of non-destructive analytical techniques which reveal the information about the crystallographic structure, chemical composition and physical properties of materials and thin films. These techniques are based on observing the scattered intensity of an X-ray beam hitting a sample as a function of incident and scattered angle, polarization and wavelength or energy.

From X-ray diffraction pattern, we can obtain the following information:-

i. Identification of phases present in the material
ii. Study the formation of a particular material system
iii. Estimation of unit cell structure, lattice parameters and miller indices
iv. Estimation of amorphous content.
v. Analysis of the average crystalline size from the width of the peak. Large grain size gives rise to sharp peaks, while the peak width increases with decreasing grain/particle size.
vi. Analysis of structural distortion caused by the strain and thermal distortion

The X-ray diffraction study has been the most popular method to guess the crystallite size in nanomaterials. The assessment of crystallite sizes in the nanometer range warrants careful analytical skills. The broadening of the Bragg peaks is attributed to the growth of the crystallite refinement and internal stain. To size broadening and strain broadening, the full width at half maximum (FWHM) of the Bragg peaks as a function of the diffraction angle is analyzed. Crystallite size of the deposits is calculated by the XRD peak broadening. The diffraction patterns are obtained using Cu-K α radiation at a scan rate of 1º/min. pseudo-Voigt curve fitting technique was used for estimating the full width at half maximum FWHM. After subtracting the instrumental line broadening, which is estimated using quartz and silicon standards; the grain size can be estimated using the Debye Scherrer formula.

The basic principle lies on the mechanism of electron (x-ray) diffraction within the crystalline lattice. Since all the atoms in a crystalline solid are regularly arranged with interatomic spacing of the order of few angstrom, the crystal can behave as a three-dimensional grating for x-rays. When monochromatic an x-ray beam passes through such crystalline solid, the x-ray electron gets diffracted as the wavelength of x-ray is comparable to interatomic spacing with the solids. In 1912, W.H Bragg and W. L. Bragg put forward a model which generates the condition for diffraction considering the reflection of x-rays beam from atomic planes as shown in Fig. 4-6. It was discovered that the constructive diffraction pattern will occur in accordance with Bragg's law condition

$$n\lambda = 2d_{hkl}\sin(\theta) \tag{4-1}$$

where n is an integer 1, 2, 3….. (usually n =1), λ is wavelength in angstroms (1.5418 Å for $Cu\ K_\alpha$), d_{hkl} is spacing between the planes, the θ is the angle between the incident light and the lattice planes, the 2θ is angle between the incident and scattered beams, the angle 2θ of maximum intensity is called the Bragg angle. All diffraction directions of the lattice will be generated by scanning through a range of 2θ angles on the sample. Figure 4-6 illustrates the reflection of X-rays from two planes of atoms in a crystal solid. From these XRD pattern, the lattice parameter of the samples can be estimated by equations 4.2-4.4.

The direction of plane normal [hkl] is perpendicular to a plane of atoms and the diffraction vector S is the vector bisects the angle between the incident and diffracted beam. The lattice constants 'a'

(4-2)

and ‘c’ and the spacing d_{hkl} for the wurtzite structure of ZnO can be calculated using the relations [108-110]:

$$a = \sqrt{\frac{1}{3}}\frac{\lambda}{\sin(\theta)}$$

$$c = \frac{\lambda}{\sin(\theta)} \qquad (4\text{-}4)$$

$$\frac{1}{d_{hkl}^2} = \frac{4}{3}\frac{h^2 + hk + k^2}{a^2} + \frac{l^2}{c^2} \qquad (4\text{-}3)$$

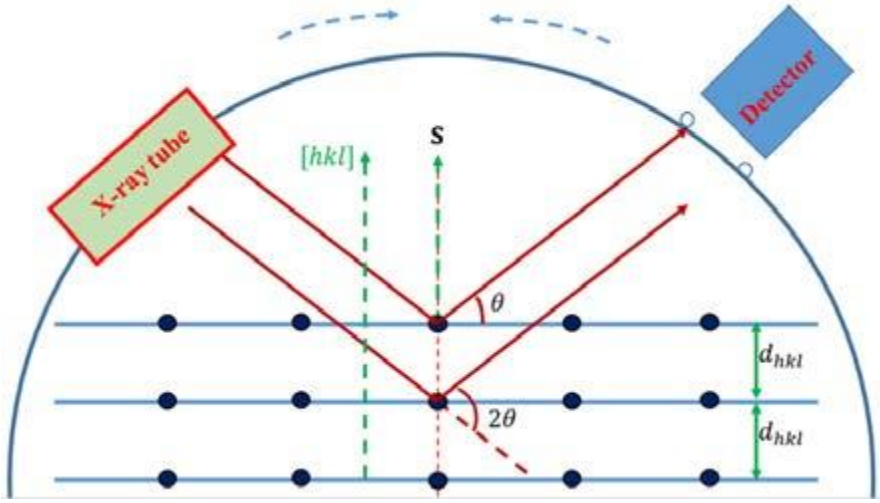

Figure 4-6 X-Ray Diffraction instrument

The XRD analysis can be used for Phase identification using & it depends on the diffraction peak position & relative intensities of these peaks. Also the XRD study reveals the presence of lattice defects & dislocation in crystals with dimensions. Small sized grains can also change the width of diffraction peak. Very small crystals also cause peak broadening. The crystallite size is a function of peak width, peak position and wavelength. The crystalline size given by Scherer’s formula [111]

$$D = \frac{0.94\,\lambda}{\beta\,\sin(\theta)} \qquad (4\text{-}5)$$

where ‘ β ’ is the FWHM in radians.

The structural strain (ε) can be calculated by using following relation

(4-6)

$$\beta = \frac{\lambda}{D\cos(\phi)} - \varepsilon\tan(\theta)$$

The dislocation density (δ) defined as the length of dislocation lines per unit volume given by

$$\delta = \frac{1}{D^2}$$

Experimentally measured diffraction patterns are compared with the standard diffraction files published by the international center for diffraction data (ICDD).

4.5.2. Electron-Matter interaction (Electron microscopy)

The principle of electron microscopy stands on the mechanism of electron interaction with matter or sample specimen. Electron can interact various way with mater (Fig. 4-7). If a beam of electron is incident on mater it can undergo two types of scattering, elastic and inelastic. In elastic scattering only the trajectory changes and the kinetic energy and velocity remain constant. In the case of inelastic scattering, some incident electrons will actually collide with and displace electrons from their orbits (shells) around nuclei of atoms comprising the sample. This interaction places the atom in an excited (unstable) state. The inelastic interactions noted on the top side of the diagram are utilized when examining thick or bulk specimens in Scanning Electron Microscopy (SEM) while on the bottom side are those examined in thin or foil specimens in Transmission Electron Microscopy (TEM).

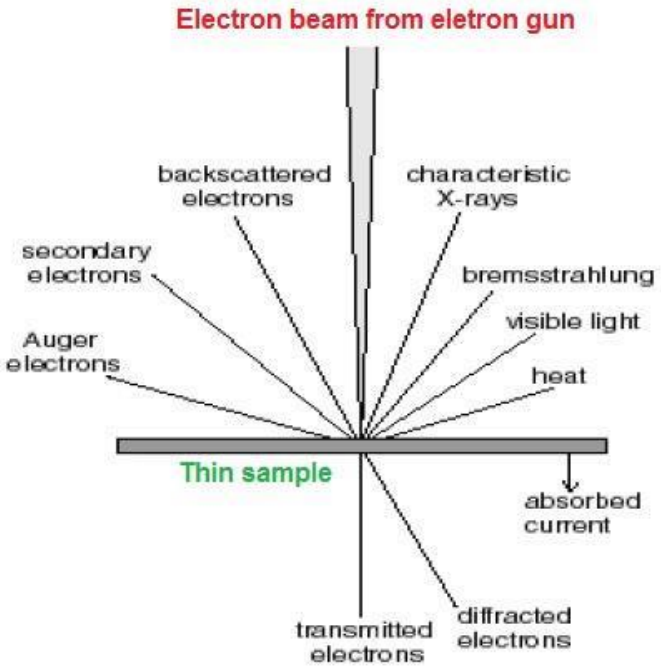

Figure 4-7 : Interaction of electron with matter (thin film sample)

Scanning Electron Microscopy (SEM)

Scanning Electron Microscopy (SEM) is a popular technique which is used for imaging the surface morphology of thick-sample. Fig. 4-8 shows a schematic diagram of SEM. A beam of electrons is focused on to sample after passing through several lens systems. The electron beam passes through scan coils and objective lens deflects horizontally and vertically so that the beam scans the surface of the sample. As the electrons penetrate the surface, a number of interactions occur that can result in the emission of electrons or photons from or through the surface. A reasonable fraction of the electrons emitted can be collected by appropriate detectors, and the output can be used to modulate the brightness of a cathode ray tube (CRT) whose x and y- inputs are driven in synchronism with the x-y voltages rastering the electron beam. In this way an image is produced on the CRT; every point that the beam strikes on the sample is mapped directly onto a corresponding point on the screen. SEM (Quanta 200 ESEM, FEI) works on a voltage between 30 to 200kV with spatial resolution of 3 nm at 30kV and its beam diameter that scans the specimen is 5nm-2μm.

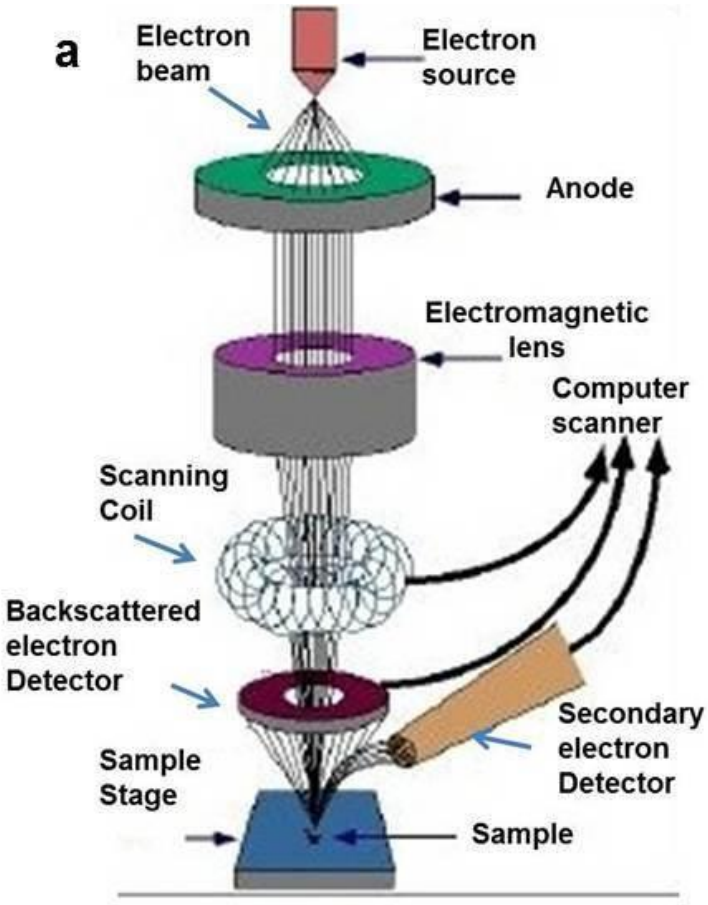

Figure 4-8: Block Diagram of SEM components

The principle images produced in SEM are of three types: secondary electron images, backscattered electron images and elemental X-ray maps. When the electron bombards with the atoms, it can eject the core electrons of the individual atoms leads to the generation of characteristic x-ray for each composite elements of the samples. EDX spectroscopy techniques attached with SEM set up collects that characteristic x-ray which are analyzed to get the information about the chemical composition and atomic percentages of individual elements.[112]

Transmission electron microscopy

Transmission Electron Microscopy (TEM) imaging exploits the electrons that are transmitted through ultrathin specimen . Nanopowder samples are initially dissolved in aqueous or alcoholic solution and ultrasonicated 20-30 minutes so that the particle gets dispersed very well inside the solution. After that a drop of solution is made to fall on the copper grid which was dried under infra-red (IR) lamp. Samples are mounted on the sample holder of TEM unit. A beam of electrons

(typical wavelength less than 1Å) are emitted by the source and focused on the samples after passing two condenser lenses which also control the brightness of the beam. The electrons that are elastically scattered consists the transmitted beams, which pass through the objective lens. The objective lens forms the image display and the following apertures, the objective and selected area aperture are used to choose of the elastically scattered electrons that will form the image of the microscope. Finally, the beam goes to the magnifying system that is consisted of three lenses, the first and second intermediate lenses which control the magnification of the image and the projector lens. The formed image is shown either on a fluorescent screen or in monitor or both and is printed on a photographic film.

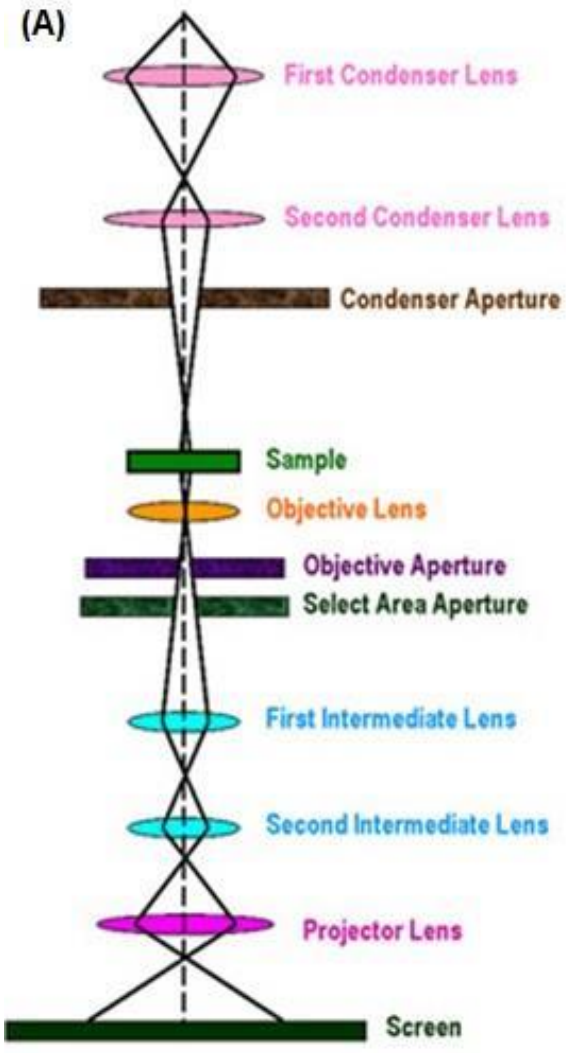

Figure 4-9: Schematic of TEM

The spatial resolution i.e. the minimum spatial separation that can be resolved by TEM (FEI TECHANI G2 SERIES) is 0.2 nm. High resolution TEM (HRTEM) is an imaging mode of TEM which provides the opportunity to imaging the crystal in an atomic scale and used to study the crystallographic orientation of atomic planes and also to estimate the inter-planar spacing. HRTEM is also very useful to detect various crystalline defects within the materials.

4.5.3. X-ray photoelectron spectroscopy

X-ray Photoelectron Spectroscopy (XPS) is widely used to investigate the chemical composition of surfaces based on photo-ionization effect. XPS uses to measure chemical composition at the surface (0 - 10 nm) of the sample, chemical or electronic state of each chemical element and uses to study the energy distribution from the emitted electrons at the surface. In principle, the XPS spectra generated by radiated an X-rays beam on the samples. When the X-ray photon energy is higher enough, the core electron will escape from the atom at the surface of the sample and emit from the surface of the sample with certain kinetic energy, which is also called photoelectron. Then simultaneously the kinetic energy and amount of electrons that releases from the top of the material (0 - 10 nm) are measure. In general, the energy of an X-ray with particular wavelength is known, and the kinetic energies of the emitted electrons are measured. The working principle of the XPS spectroscopy and binding energy diagram are illustrated in Figure 4.3.

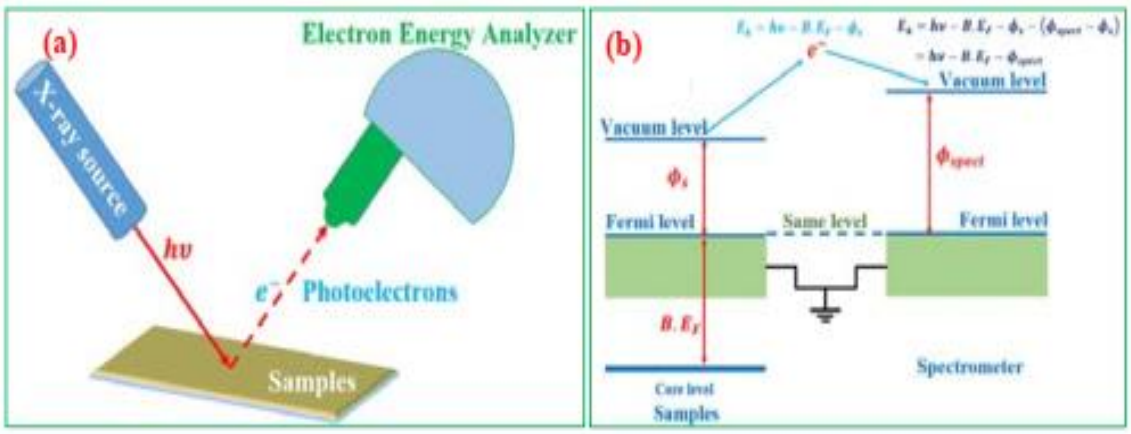

Figure 4-10: (a) Working principle of XPS spectroscopy (b) Binding energy diagram

Therefore, the binding energy of each emitted electrons can be estimated by the following equations 4.8 and 4.9:

$$E_b = E_{photo} - (E_k + \phi_{spect}) \quad (4\text{-}7)$$

$$E_k = h\nu - E_b - \phi_{spect} \quad (4\text{-}8)$$

Where E_b is the binding energy (B.E) of the atomic orbital from which the electron originates, E_{photo} is the energy of the X-ray photons being used, E_k is the measured kinetic energy of the electron and ϕ_{spect} is the work function of spectrometer. The XPS spectrum describes about the amount of detected electrons as a function of binding energy of the detected electrons. Due to each element produces a set of XPS peaks at a specific characteristic binding energy values therefore the XPS normally used to analyze the concentration of the chemical elements on the surface of the sample. A change in the elemental binding energies (the chemical shifts) can be used to identify the chemical state of the materials [113].

4.6. Optical properties characterization

The demand for low cost, high performance optoelectronic devices is increasing in the current era. It has lead to the development of transparent conductive oxide (TCO) thin films. These films can be used in a wide variety of applications such as touch screen display, gas sensors, acoustic wave transducers, magneto-optic storage devices, solar cell electrodes & optical position sensor etc.. Most of the techniques which are used for studying optical properties involves spectrophotometer.

.

Principle of Spectrophotometer

A spectrophotometer device may use either single beam or double beam. The main components of a spectro-photometers are

a) source of light with single/continuous wavelength (eg. light-emitting diode (LED)),
b) sample container
c) Optical detector (photodiode)

In a spectrophotometer instruments having continuous light source, a dispersive element is used for dispersion of different wavelengths finally selecting a single wavelength using aperture /slit for before passing through the sample as shown in fig.4.11. Another version of spectrophotometer uses two beams (also known as double beam spectrophotometer) among which one used as reference; the other is passed through the sample.

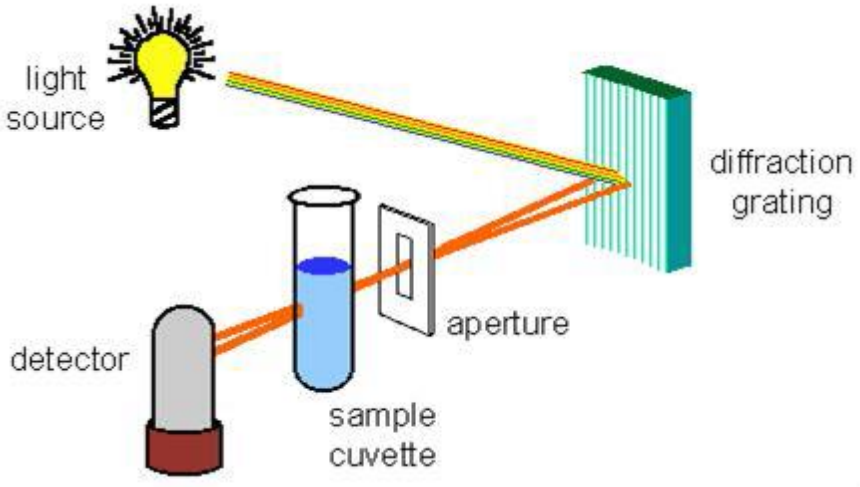

Figure 4-11:diagram showing principle of spectrophotometer

At output the measurement displayed as the ratio of the two beam intensities. Some two beam spectrophotometers use two detectors for measuring sample and reference beam at the same time. The electronics or software module produce the absorption/transmission spectrum of samples spectrum as a function of wavelength . UV/Vis spectrophotometry is used for thin films, liquids. However the absorbance of gases / solids can also be measured using UV-Vis spectroscopy. Samples are typically placed in a transparent cell, known as a cuvette which are made of high quality fused silica or quartz glass because these are transparent throughout the UV, visible and near infrared regions. Glass and plastic cuvettes are also common, although glass and most plastics absorb in the UV, which limits their usefulness to visible wavelengths.

Band gap engineering

Some of the modern applications needs electronic control of the band gap. It has been reported that bandgap control is possible for alloys for large/small band gap materials.The energy gap Eg of a ternary semiconductor is determined using the following empirical equation [114]. For example, if material P has a band gap X, and material Q has a band gap Y then the band gap Eg of the PQ alloy is

$$E_g = \frac{1}{2}X + \frac{1}{2}Y - \frac{1}{4}B \qquad (4\text{-}9)$$

where B is the band gap bowing coefficient. The DMS based on Mn doped ZnO provides the possibility of tuning band parameters by varying composition of the material. virtual crystal approximation predicts a linear variation in the band gap. However this is not the case for Mn

doped zinc oxide. In the Mn doped ZnO system the bandgap measurements show a deviation from the linear dependence as predicted by VCA [115].

The optical properties include absorption, transmission spectra, band gap, impurity state, extinction coefficient etc. The semiconductors usually show a sharp rise pattern in the optical absorption spectra beyond a certain value of the incident optical energy. The fundamental reason of this may be due to the excitation of electrons to the conduction band (CB) from the valence band (VB). Most of the semiconductors exhibits two types of electron transitions which are direct band gap transition and indirect band gap transition.

Semiconductor having direct band gap implies that the minimum energy of the conduction band lies directly above the maximum energy of the valence band in energy-momentum space. They can be used in fabrication of efficient light emitting devices.

Semiconductors that have an indirect band gap are inefficient at emitting light, because any electron quickly settles into the energy minimum of energy band. Silicon being indirect band gap is not useful for light-emitting devices.

In the opto-electronic applications of thin films, the optical absorption studies play an important role giving an insight into the nature of transitions, either direct or indirect.

The absorption coefficient (α) can be estimated from the optical transmittance spectra using the relation

$$\alpha = \frac{2.303 log_{10}\left(\frac{1}{T}\right)}{t} \qquad (4\text{-}10)$$

where T is the transmittance value at a particular wavelength and t is the thickness of the semiconductor film.

In the direct band gap material, the transition between the conduction band minimum and valence band maximum occurs at the same k-vector. The transition probability is given by

$$(\alpha h\nu)^p = \mathrm{A}\left(h\nu - E_g\right)$$

Where Eg is the energy gap, v is the frequency, A is a constant and h is the Planck's constant. The exponent p is the number which characterizes the transition process, (4-11)

p = 2 for direct permitted transitions

p = 2/3 for direct invalid transitions

p = 1/2 for indirect permitted transitions

p = 1/3 for indirect invalid transitions

The band gap is determined by plotting $(\alpha h\nu)^p$ against photon energy hv. For suitable value of p the graph is a straight line and the value of band gap (E_g) is obtained by extrapolating the linear portion of the graph to intercept the energy axis. The optical method provides a very simple & reliable way of finding the band gap as compared to the electrical method.

4.6.1. Photoluminescence spectroscopy

Photoluminescence (PL) spectroscopy is one of the most popular & non-destructive technique for investigating the optical property of the material. The Photoluminescence is a process in which the material absorbs and re-radiates photons. It can also be described in quantum mechanics with the help of excitation of electrons to a higher state and then return to a lower state by the emission of a photon. This is one of many forms of luminescence (light emission). The time gap between absorption and emission is extremely short, few nanoseconds.

In addition to absorption & transmission spectra, other properties such as surface roughness/ quality, impurity levels and disorders etc. are also studied by Photoluminescence (PL) spectroscopy. The study of near-band-edge emission provides approx.. value of the band gap energy (Eg) of the some material such as ternary alloys. The time-resolved PL spectroscopy can be very fast, & hence it can be a useful tool for characterizing the very rapid processes in a material because some thermally processes lead to changes in PL intensity. However, one major limitation of this method is its dependence on radiative events. PL spectroscopy system has following components,

1. A light source (continuous or pulsed laser).
2. Dispersive element for light dispersion (spectral analysis of PL).
3. sample holder including lens optics for focusing light and collecting the emissions.
4. Optical detector along with appropriate electronics for signal conditioning & readout mechanism.

As the measurement does not rely on electrical excitation or detection, sample preparation is minimal due to which it is attractive for material systems having poor conductivity or undeveloped contact / junction technology. PL is the only technique available for studying fast transient behavior in materials.

The main principle of the PL measurements is that, the semiconductor is excited by light photons which has higher energy than the band gap of the semiconductor such as a laser. Then the incident photons are absorbed and create electron-hole pairs in the semiconductor.

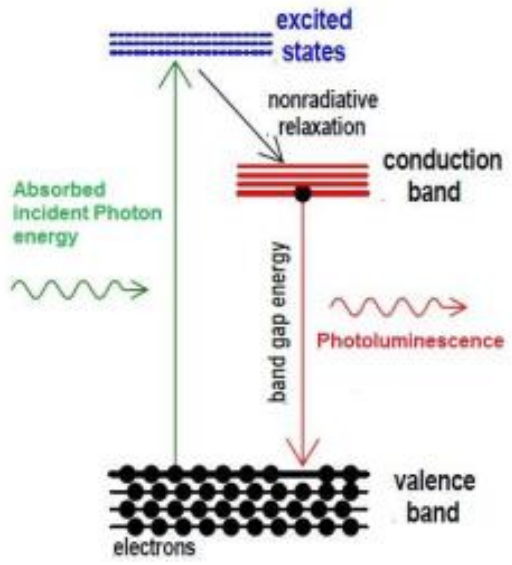

Figure 4-12: Diagram showing mechanism of Photoluminiscence

Within a short period of time the electron-hole pairs are recombined and emit photons from the semiconductor, the energy of the emitted photons reflects the carrier energy in the semiconductor. Finally, the emitted luminescence (light) and intensity are collected and recorded to generate a PL spectrum. These emitted photoluminescence and intensity are the direct measurement of the semiconductor properties such as bandgap, impurity levels and defect detection and recombination mechanisms [116].

4.6.2.Cathodoluminescence spectroscopy

The cathodoluminescence (CL) technique is similar to other spectroscopic techniques such as PL spectroscopy technique. Comparing the CL spectrum with PL spectrum should yield similar results. In principle, the electron beam excites the sample, leading to the emission of light from the semiconductor sample, showing all mechanisms of radiative recombination which are present. CL spectroscopy is used to investigate the impurity induced defects, trace element analysis, and to

map the spatial distribution of stress around defects. An advantage of using the CL is the ability to obtain more detailed depth-resolved information by varying the electron-beam energy.

4.6.3.UV-visible spectroscopy

Ultraviolet-visible spectroscopy (UV-vis) is a spectroscopy (absorption or reflectance) in the ultraviolet-visible region. The UV-vis absorption spectroscopy provides information of light absorption as a function of wavelength, which describes the electronic transitions occurring in the measured samples. The UV-vis spectrophotometer detects the light intensity passing through a sample and compares the detected intensity to incident light intensity (light before passes through the sample): The absorbance A is simple expressed as Beer's law:

$$A = -\log\left(\frac{I}{I_0}\right) \tag{4-12}$$

Where the ratio I/I_0 is called transmittance, I is the intensity of light passing through the sample and I_0 is the intensity of light before passing through the sample. the optical band gap of the samples can be estimated using

$$\alpha = \left(\frac{k}{h\nu}\right)\left(h\nu - E_g\right)^{\beta} \tag{4-13}$$

Where $\alpha = 2.303 \times \frac{A}{d}$ is the absorption coefficient, d is thickness of the sample (length of nanorods), $\beta = 1/2$ for direct band gap semiconductors and $k = \alpha\lambda/4\pi$ is the extinction coefficient, h is Planck's constant and $h\nu$ is the incident photon energy .

$$\alpha = \left(\frac{k}{h\nu}\right)\left(h\nu - E_g\right)^{1/2} \tag{4-14}$$

$$(\alpha h\nu)^2 = \mathrm{C}\left(h\nu - E_g\right) \tag{4-15}$$

The optical energy gap of the samples were obtained from the intercept of the linear portion with the x-axis of versus $h\nu$ curve.

4.7. Magnetic properties characterization

The physical quantity called magnetic susceptibility (χ) describes the properties of the material placed in external magnetic field. Magnetic susceptibility is defined as χ=M/H: Where M is magnetization of the material in the magnetic field and H is the field intensity. While the the material is classified as ferromagnetic materials, diamagnetic materials and paramagnetic materials, respectively. Normally, magnetization is measured by using superconducting quantum interferometer device (SQUID) magnetometer. This is due to the fact that the SQUID provides extremely high sensitivity to any magnetization such as magnetic impurities, precipitates, clusters, and mixed magnetic phases. In the case of TM-doped ZnO materials, SQUID measurement is performed to observe the ferromagnetism behavior at Curie temperatures near/above room temperature. The combination of SQUID, XRD and XPS measurements can provide information about the origin of ferromagnetism of the TM-doped ZnO nanostructures.

4.7.1.Electron paramagnetic resonance spectroscopy

Electron paramagnetic resonance (EPR) spectroscopy is often employed in material research to investigate the presence of any unpaired spin species such as paramagnetic radicals, vacancies etc. In case of oxide materials, EPR spectroscopy is widely used to identify the presence of oxygen vacancies (VO). Depending on the charge, there exist three types of VO such as doubly ionized (VO^{++}), singly ionized (VO^{+}) and neutral (VO^{0}). Among them only singly ionized (VO^{+}) is EPR active while the other two are EPR silent.

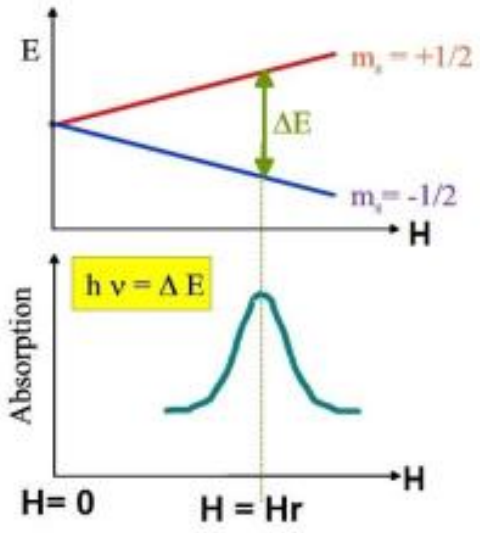

Figure 4-13: Working principle of EPR

The basic principle of EPR spectroscopy is quite analogues to those of nuclear magnetic resonance (NMR), but it is electron spins that are excited instead of the spins of atomic nuclei. An electron with spin S=1/2 has its two possible magnetic spin quantum number $m_s = 1/2$ and $m_s = -1/2$. In presence of an external magnetic field (H) the electron magnetic moment (μ_B) aligns itself either parallel ($m_s = 1/2$) or antiparallel ($m_s = -1/2$) to the direction of external magnetic field and individual alignment having a specific energy $E = g\,\mu_B m_s H$ due to Zeeman effect. Where, g is Lande g factor, $\mu_B$is Bohr magnetron.

EPR spectroscopy is performed using microwaves with frequency 9-10 GHz and the corresponding magnetic field strength is about 3500 G. Absorbed spectrum is collected by scanning the magnetic field strength keeping frequency at a fixed value. An unpaired electron can move between the two energy levels by either absorbing or emitting a photon of energy hν such that at resonance condition $h\nu = \Delta E = g\,\mu_B H_r$ which is the fundamental equation of EPR spectroscopy. H_r is resonant magnetic field strength.

4.7.2.Vibrating sample magnetometer

Vibrating sample magnetometer (VSM) is used to measure the magnetic properties of the sample. The basic principle of VSM lies on Faraday's Law of Induction, $\nabla \times \vec{E} = \frac{\partial}{\partial t}\vec{B}$ which tells us that a changing magnetic field (B) will produce

an electric field (E). This electric field can be measured and can give us information about the changing magnetic field. Thus, the sample is placed in a constant magnetic field and oscillated with a fixed frequency near a set of detection (pickup) coils. If the sample is magnetic, the constant magnetic field induces a magnetic dipole moment in the sample. This magnetic dipole moment creates a magnetic field around the sample. As the sample is oscillated, this magnetic flux changes as a function of time and the voltage induced (proportional to the rate of change of flux) in the pickup coils is synchronously detected. The voltage will also be proportional to the magnetic moment of the sample. In Fig. we show (a) schematic of VSM and (b) detailed configuration near the pick-up coils. The system detection capability can be maximized by optimizing the geometry of the pickup coils and by having oscillation amplitude that is relatively large (1 – 3 mm peak). The time dependent voltage induced in the pickup coils is given by

$$V_{induced} = \frac{d\phi}{dt} = \frac{d\phi}{dz}\frac{dz}{dt}$$

where, ϕ represents the magnetic flux, the axis of oscillation of the sample is conventionally chosen to be the z – axis, and z, therefore, represents the position of the sample along this axis and t is the time. If the sample is made to oscillate sinusoidally, then the induced voltage in the pickup coils will have the form $V_{induced} = cmA\omega\sin(\omega t)$ where, c is a coupling constant, m is the DC magnetic moment of the sample, A is the amplitude of oscillation, and $\omega = 2\pi f$, where f is the frequency of oscillation of the sample. The detection of the magnetic moment of the sample, thus, amounts to measuring the coefficient of sinusoidal voltage response induced in the detection coil.

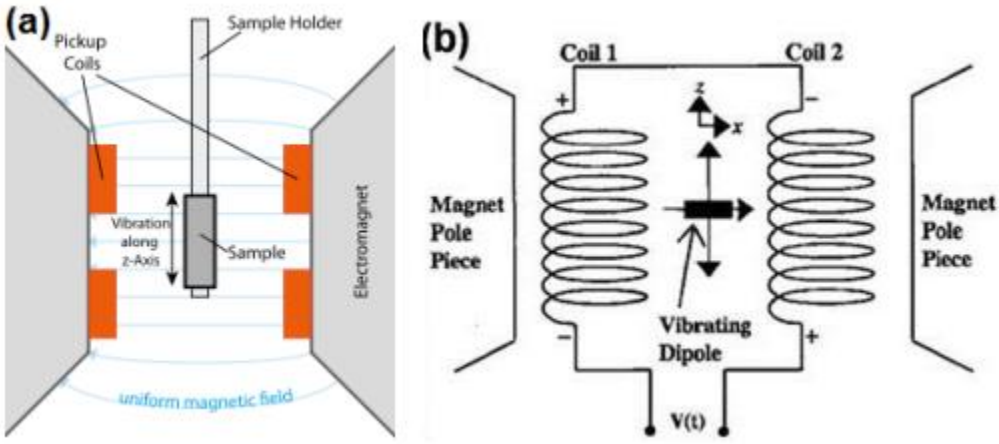

Figure 4-14: Schematic diagram of (a) VSM & (b) details near pickup coils

4.7.3. SQUID magnetometer

Superconducting Quantum Interference Devices (SQUID) is another-type of magnetometer which has much higher sensitivity (~10^{-8} emu) compared to the VSM (~ 10^{-6} emu). Thus SQUID magnetometer provides the opportunity to measure the sample having very low magnetic moment with high degree of accuracy. The basic principle of a SQUID is based on the quantum interference of wave functions that describe the state of the superconducting charge carriers (the Cooper pairs). A SQUID is based on an interferometer loop in which two weak links (Josephson contacts) are established. A weak link is established by interrupting a superconductor by a very thin insulating barrier. The function of the SQUID is to link the quantum mechanical phase difference of the Cooper pairs wave functions over a weak link with the magnetic flux penetrating the interferometer loop.[117]

There are two types of SQUID operation such as direct current (DC) which uses two parallel Josephson junction and the another is the radio frequency (RF) SQUID which have only one Josephson junction. The components of a SQUID magnetometer typically consist of the following: a detection coil which senses changes in the external magnetic field and transforms them into an electrical current, an input coil (i.e. the SQUID element with one or two Josephson junction) which transforms the resulting current into a magnetic flux in the SQUID sensor, electronics which transform the applied flux into a room temperature voltage output and acquisition hardware and software for acquiring, storing and analyzing data. Both the SQUID amplifier and detection coils are superconducting devices.

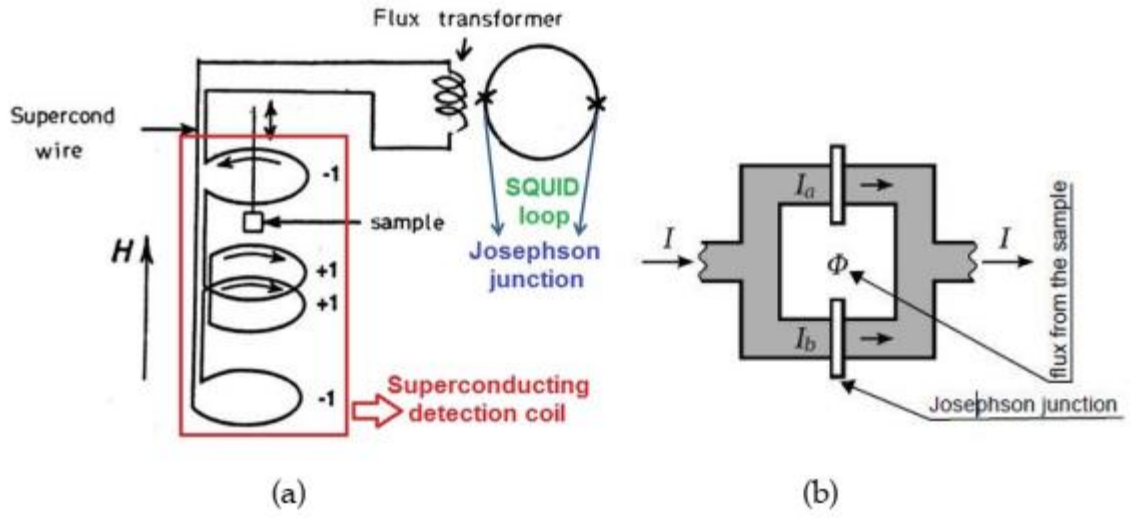

Figure 4-15: Schematic diagram of SQUID magnetometer

Superconducting detection Coil and SQUID loop

These are the two principle parts for the function of SQUID magnetometer. The detection coil consists of a superconducting wire in a set of three coils configured as a second order gradiometer (as shown in Fig. 4.14(a)). The coil sits outside the sample space within the liquid helium bath. The upper coil is a single turn would clockwise, the centre coil comprises two turns wound counter-clockwise and the bottom coil is a single turn wound clockwise. The coils are positioned at the centre of the superconducting magnet outside the sample chamber such that the magnetic field from the sample couples inductively to the coils as the sample is moved through them.

The SQUID loop is superconducting loop with two Josephson junction (Fig. 4.14(b)) and can be used to convert the sample magnetic flux to equivalent voltage which is detected computer system through a lock in-amplifier. The Josephson junction [118] is a junction between two superconductors which are weekly coupled separated (in the case of low- Tc Tunnel junction) by thin insulating barrier. Under this condition, cooper pairs of electrons can pass from one superconductor to the other even with no applied voltage. It operates under the] (4-17) of flux quantization within the superconducting loop. Magnetic flux passing through a superconducting current circuit is quantized $\phi_0 = {}^{h}/_{2e} \approx 2.067 \times 10^{-15} Tm^2$ and the current passing through the Josephson junction will be a function of the flux due to sample's moment and is given by

$$J_{total} = J_0 cos\left(\frac{2\pi e}{h}\phi\right)$$

Since the junction has a resistance, the voltage drop across the junction is measured using appropriate electronics devices.

4.7.4. Atomic and Magnetic force microscopy

Atomic force microscopy (AFM) is a high resolution imaging techniques in which the forces due to individual atom are exploited. The AFM consists of a silicon or silicon nitride cantilever with a very sharp tip to scan the surface of sample. The tip radius of curvature is generally of the order of nanometers. When the tip is brought very near to sample surface, forces between the tip and the sample lead to a deflection of the cantilever according to Hooke's law. Depending on the situation, forces that are measured in AFM include mechanical contact force, van der Waals forces, capillary forces, chemical bonding, electrostatic forces, magnetic force, Casimir forces, solvation forces, etc. The AFM can be operated in different modes, depending on type of the application. In general, possible imaging modes are divided into static (also called contact) modes and a variety of dynamic (non-contact or "tapping") modes where the cantilever is vibrated. Unlike AFM in which the atomic or electrostatic forces are measured, the magnetic force microscopy (MFM) technique uses the magnetic force of sample to generate the images of magnetic domains within the specimen (Fig. 4.15). The MFM is another mode of AFM in which the sharp tip of the cantilever is magnetized and it scans over the magnetic sample . The tip-sample magnetic interactions are used to reconstruct the magnetic structure of the sample surface. Many kinds of magnetic interactions are measured by MFM, including magnetic dipole–dipole interaction. MFM scanning often uses non-contact AFM (NC-AFM) mode. During MFM measurements, the magnetic force between the sample and the tip can be expressed as

$$\vec{F} = \mu_0(\vec{m}\,.\nabla)\vec{H} \qquad (4\text{-}18)$$

where $\vec{m}$ is the magnetic moment of the tip (approximated as a point dipole), $\vec{H}$ is the magnetic stray field from the sample surface, and μ_0 is the magnetic permeability of free space.

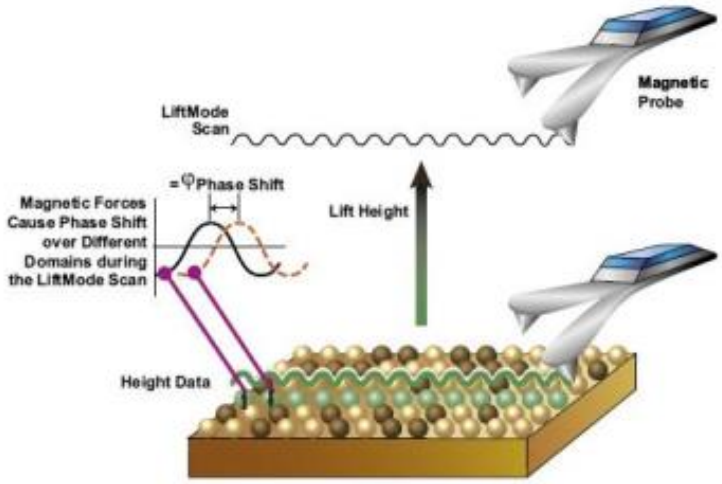

Figure 4-16: Magnetic Force Microscopy using silicon probe (magnetically coated with Ni) scanning

The imaging is performed keeping the probe (tip) at a lift height of ~300 nm over a scan size of 2.5×2.5 μm on the surface. Typical resolution of 30 nm can be achieved, although resolutions as low as 10 to 20 nm are attainable.

5. PREPARTION & STUDIES ON INDIUM-DOPED ZnO TRANSPARENT CONDUCTING THIN FILMS

Modern optical and electrical applications are two core areas which have been intensively investigated for conducting oxide (TCO) films. The examples are liquid crystals, organic light-emitting diodes, thin-film transistors, and thin-film solar cells. The ideal situations for these thin films are having low resistivity, high transmittance in the visible region with appropriate stability in terms of thermal /chemical. Indium oxide based ITO's have been considered superb because of good electrical and optical properties. Recently, zinc oxide (ZnO) has evolved as a much better alternate for transparent conducting oxide because of its wide band gap (>3.3 eV at room temperature) and high excitation binding energy (0.060 eV) and other multiple functionalities. III group elements from the periodic table have been used for improving the electrical conductivity and optical transmittance of ZnO films [119-120]. In this study, Indium -doped ZnO (IZO) thin films have been prepared by using sol–gel spin-coating technique. We study the effect of these dopants on the microstructure, electrical, and optical properties as a function of doping concentration. The reason we use the deposition of thin films by spin-coating due to it is a very simple with ultralow instrumental costs and widely used technique to prepare films of uniform thickness of non-volatile materials initially found in liquid solution dissolved in a volatile solvent. Furthermore, deposition by spin coating produces films with thickness that become uniform during spin-off if the viscosity is homogeneous everywhere on the substrate and is independent of the sliding force. The uniformity of the film thickness results from the balance of two opposite main forces: the centrifugal and the viscous forces.

5.1. Synthesis of ZnO and doping with Indium

In doped-ZnO (IZO) thin films were prepared by the sol–gel method using spin coating technique. As a starting material, Zinc acetate dehydrate ($Zn(CH_3COO)_2.2H_2O$) was used as solute,

Isopropanol Alcohol (IPA, $CH_3CH(OH)CH_3$) was used as solvent & mono ethanolamine (MEA, C_2H_7NO) was used as a stabilizer, respectively. The dopant source of Indium was indium chloride ($InCl_3$). Zinc acetate dehydrates and dopants were first dissolved in a mixture of Isopropanol Alcohol and MEA solution at room temperature. The molar ratio of MEA to zinc acetate ($Zn(CH_3COO)_2$) was kept at 1 M and the concentration of zinc acetate was kept to 0.75 M. The In dopant concentration [In/In+Zn] was studied from 1% to 10%. The solution was stirred at 50°C for 2 h to yield a clear and homogeneous solution, which served as the coating solution. The solution was dropped on glass substrates. The glass substrate was cleaned before by sonication in acetone for 5 min, followed by ethanol for another 5 min, then rinsed with DI water and blown dry by nitrogen. The solution was dropped on the glass substrate by spin coating was rotated at 2000 rpm for 30 s.

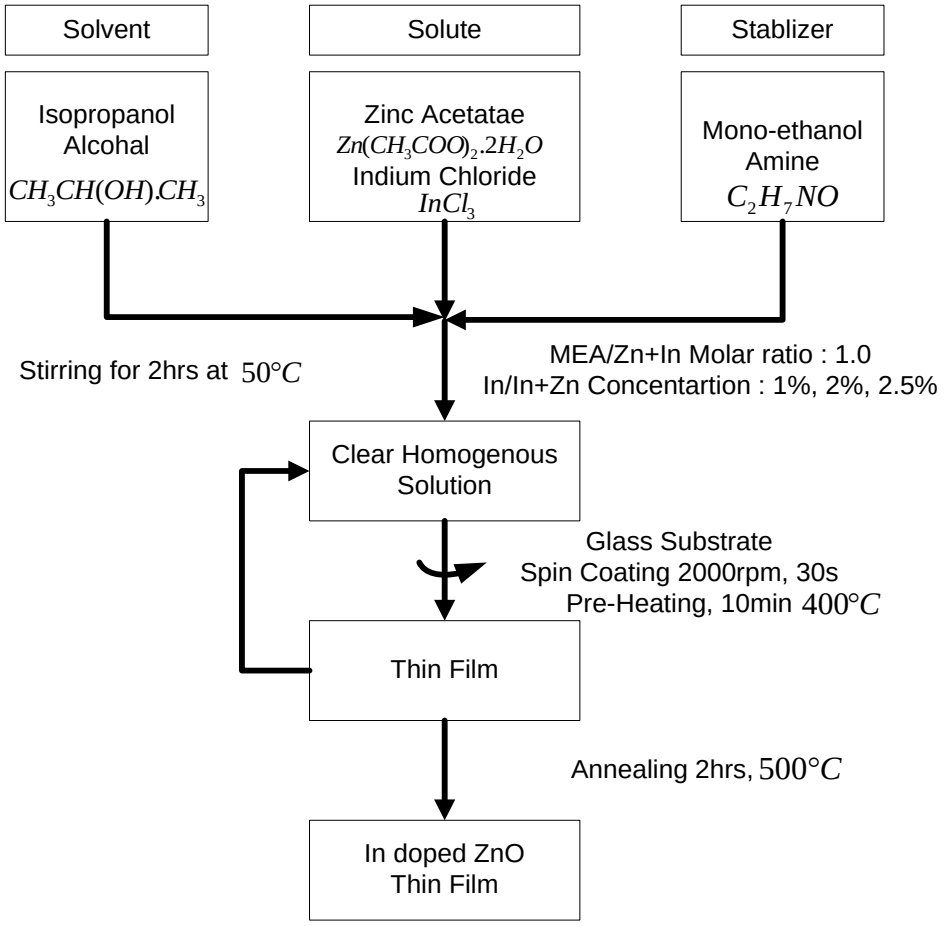

Figure 5-1 : Synthesis of In doped ZnO thin films

After depositing by spin coating, the films were preheating at different temperature (400°C to 450°C) for several minutes (10 min) over a hot plate to evaporate the solvent, remove organic

residuals, followed by decomposition and oxidation of the precursor to form doped ZnO, then naturally cooled to room temperature.

The procedures from coating to drying and cooling were repeated several times until the thickness of the films was approximately 300 nm. The films were post-heating in vacuum 10^{-3} Torr at 500°C for 2 hours to get IZO films with preferential orientation.

5.2. Study of Structural properties of In-Doped ZnO thin films

The structural properties of the IZO films were characterized using X-Ray Diffraction (XRD). Figure-5-2 shows the XRD patterns of the films doped with various indium concentrations. Interestingly, only a strong (0002) ZnO peak was observed in the films, no additional diffraction peak was detected for all IZO films, corresponding independent of the Indium doping concentration. The 0002 peaks indicate that the films are highly oriented with their crystallographic c-axis perpendicular to the substrate. This strongly asserts that there is no significant change in orientation for the films deposited at various doping concentration. In other words, the Wurtzite-type crystal structure of ZnO is dominantly formed to produce the IZO films at any doping concentration. No signal corresponding to a single metallic phase of Indium or to phase separation between Indium and Zinc oxide (Figure-5-2) of all films was detected, which provides evidence that the Indium present could be substituted in the Zinc oxide lattice with the Wurtzite structure.

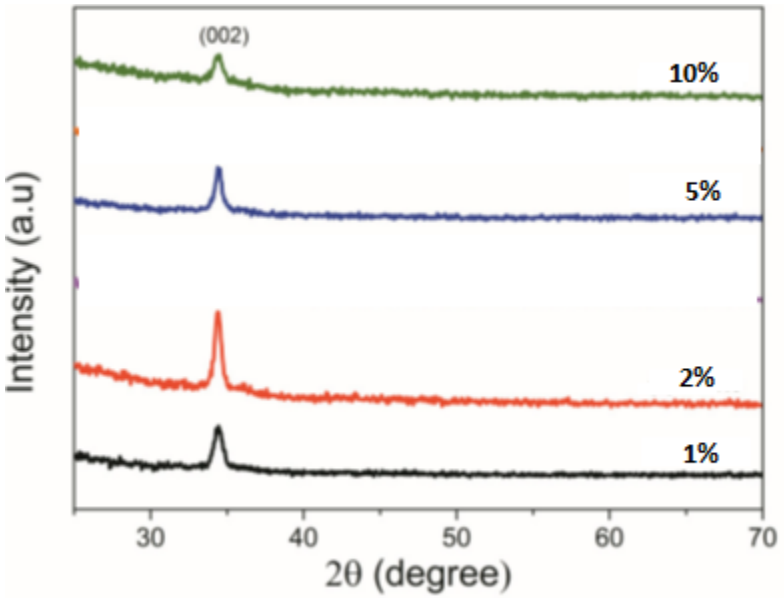

Figure 5-2 : X-Ray Differaction Spectra of In doped ZnO films

The crystallite properties of all films under different In doping concentration were also evaluated by observing the full width half maximum (FWHM) for different doping concentration which suggests deterioration of crystallinity of the films at higher doping concentrations (>5%), which may be effect of the formation of the compressive stresses due to more ions In occupies in the interstitial sites of ZnO under high doping level of In and the segregation of dopants in grain boundaries for high doping concentrations. In addition, the lattice constant of IZO films was larger than that of the pure ZnO films [119-120]. Due to the radius of In^{3+} ion (0.84 A°) not only was larger, but also was substituted for the Zn^{2+} ion (0.74 A°) when the indium was doped. This result can be attributed to indium ions substituting for the zinc atoms and suppressing the growth of ZnO.

5.3. Study of Electrical properties of In Doped ZnO thin films

Thin films were prepared by doping of Indium (III) chloride, and different [In]/[In+Zn] atomic percent ratios, i.e., 1.0%, 2.0%, 5% and 10.0% were tested. A molten tin bath was used for substrate heating, and the temperature of the bath was controlled and monitored by a thermocouple. Substrate temperatures selected were 400, 425 and 450 °C, within ±1 °C variation. The deposited thin films were presented an apparent homogeneous surface and very good adhesion with the substrate. The sheet resistance, of indium thin film were measured by the four-point probe technique, taking into account the adequate geometrical corrections. The vacuum aluminized film was sandwiched between two electrodes. The sample was thermally polarized at different temperatures and electric fields. The sample holder was placed in a digitally controlled oven heated up to poling temperature. The sample was then allowed to remain at that temperature for about 30 min. Then desired strength of electric field was applied for 1 h at poling temperature. The sample was allowed to cool down at room temperature in the presence of applied field. The complex TSDC spectrum was obtained by submitting the sample to a constant electrical field E_p = 10M V/m during 2 min at a varying polarization temperature of T_{max} = 1500C.The sample is then cooled, with a ramp of 20 C/min, to liquid nitrogen temperature in the presence of the electrical field. The field was then suppressed at around 250 C and the electrodes were short-circuited for 15 min. All measurements were repeated to verify the reproducibility and the accuracy of the results. The current was measured with an electrometer and recorded by using X–Y plotter. The electrometer was also coupled to a PC for data collection. A platinum temperature sensor Pt100, mounted in the sample holder and adjacent to the film, allowed the temperature measurement with a precision of

0.05 0C. The heating rate of 50C/min was used and controlled by a temperature regulator. The DSC measurements were performed in a Perkin-Elmer with a controlled cooling accessory.

5.3.1.Results & Discussions

Figure 5-3 showed the depolarizing current vs. Temperature at constant polarising temperature Tp (i.e.40, 60, 80 and 90°C). Figures 5-4 showed the TC curve for charging mode obtained for polarising temperature Tp (i.e.40, 60, 80 and 90°C) with polarizing field Ep (05MV/m) for Al-Al electrode system respectively.

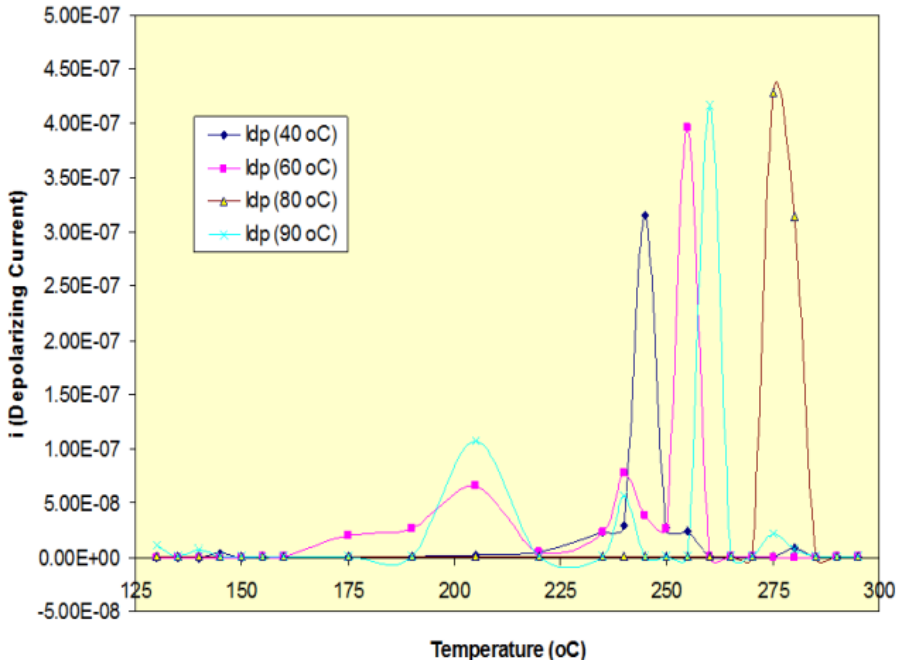

Figure 5-3: Depolarizing Current for doped ZnO System

These characteristics are showing two to three peaks at each temperature, one at low temperature (β peak), which is associated with dipolar relaxation, and other at higher temperature (α peak) that appears due to space charge relaxation. The analysis of the shape of TSDC peak makes it possible to obtain the activation energy, relaxation time and charge released. When polarizing field was increased, the magnitudes of both peaks increased.

The present study on polarizing field and temperature dependence of electrical conduction in un-doped and doped films has been carried out to understand the role of dopant when added in varying concentrations.

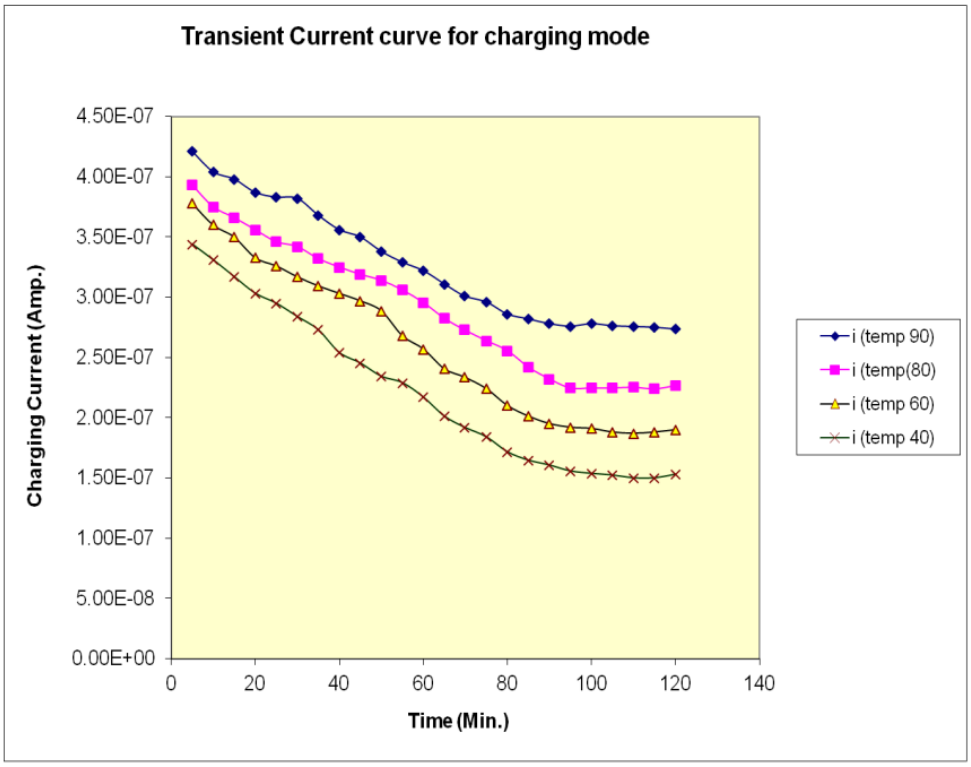

Figure 5-4: TC curve for charging mode

The conductivity also depends on temperature. As the temperature increases film becomes soft and mobility of the main chain segments as well as the rotation of side groups become easier. Thus, at higher temperature more and more dipoles are oriented resulting in the higher equivalent surface charge density i.e. as temperature increases conductivity increases as per Arrhenius equation

$$\sigma = \sigma_0 \exp\left(-{}^{E_a}/_{kT}\right)$$

where σ_0 is the pre-exponential factor, E_a the activation energy of conduction and k the Boltzmann's constant. The activation energy for these low and high temperature regions are also different Electrical conductivity of all the samples were measured by the four-point probe method by considering the geometry of electrical contacts located over them. It was observed that, with the increase in the substrate temperature, the resistivity of the ZnO:In thin films decreases, reaching a minimum value, for a fixed [In]/[In+Zn] ratio in the starting solution. From the measured electrical conductivity of the samples presented in Table 5-1. Low resistivity of

the ZnO:In films containing 5 at% nominal indium contents fabricated at Ts = 450 °C might be associated with their compact surface morphology and bigger crystallite sizes.

Table 5-1: Electrical resistivity of In doped ZnO films

[In]/[In+Zn]	Electrical Resistivity (Ω·cm)		
	400ºC	425ºC	450ºC
1.0%	1.1×10^{-2}	4.4×10^{-3}	4.1×10^{-3}
2.0%	8.6×10^{-3}	3.3×10^{-3}	3.3×10^{-3}
5.0%	3.5×10^{-2}	2.2×10^{-2}	3.1×10^{-3}
10.0%	7.5×10^{-3}	8.1×10^{-3}	5.2×10^{-3}

5.4. Study of Optical properties of In-Doped ZnO thin films

The optical properties of indium doped zinc oxide (IZO) were obtained using UV-visible spectrophotometer in the wavelength from 300 to 1500 nm. The optical transmittance spectra of the doped ZnO thin films for different wavelengths are presented in Figure-5-5. All IZO films show a very good transmittance, between 80 and 90%, within the visible wavelength region. An increase in Indium dopant concentration, leads to a slight decrease in optical transmittance, but still maintain above 80% transmittance.

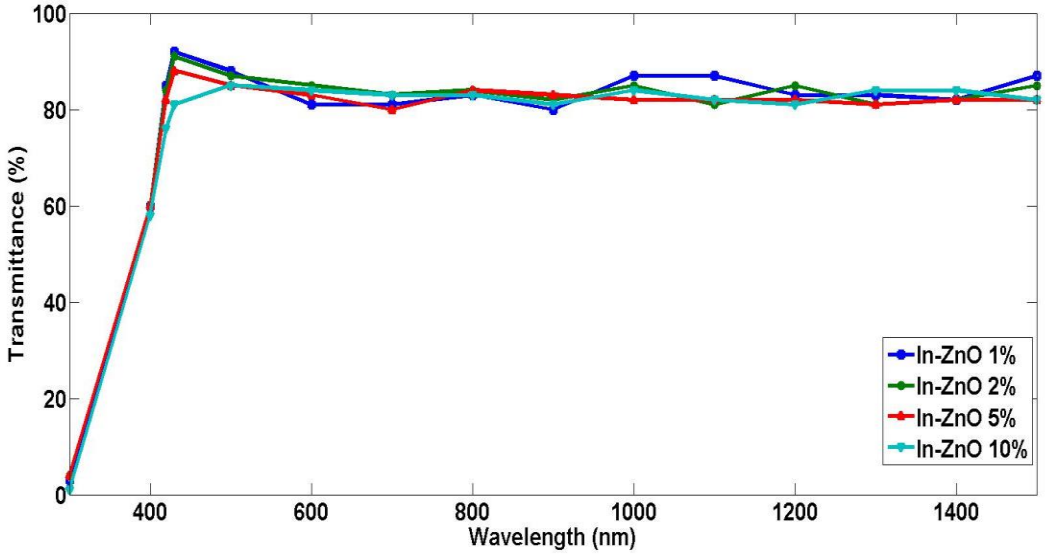

Figure 5-5 : Optical Transmittance spectra of In doped ZnO films

5.5. CONCLUSION

Indium-doped ZnO thin films were prepared by sol–gel spin-coating method for TCO applications. All films had a crystal structure, and a minimum sheet resistivity of $3.1x10^{-3}$ Ω.cm for doped ZnO thin film. In conclusion, the structural, morphological, electrical, and optical characteristics of IZO thin films were observed, and In doping seems to be more effective at 5% doping concentration. Additionally, the optical transmittance observations show a very good transmittance (> 90%) within the visible wavelength region which suggests that In doped ZnO thin films can be very good candidates for transparent conducting oxides

6. PREPARTION & STUDIES ON Mn-DOPED ZnO DILUTE MAGNETIC SEMICONDUCTORS

Zinc oxide is a well-known wide band-gap semiconductor due to its electronic, optical, structural properties. Because of these properties, ZnO presents a strong excitonic UV light emission at room temperature. It also presents a high photoconductivity and considerable piezoelectric and pyroelectric properties. Because of these properties, ZnO has attracted much attention for potential applications in various electronic and optoelectronic devices. The main focus of research lies that how to change the optical, magnetic & electronic properties of this semiconductor. The simplest way is to incorporate 3d block transition metal ions from periodic table as dopant into ZnO. Semiconductor with small amounts of such ions is also known as dilute magnetic semiconductors (DMS). In DMS materials, magnetic ions substitute a small fractions lattice sites of semiconductor. The exchange interactions between these ions & free carriers leads to ferromagnetism. They can be very usefull materials in future for spintronic applications. Transition metal which are important as dopant comes from 8th block of periodic table like Co^{2+} , Mn^{2+}, Ni^{2+},Cu^{2+}, Fe^{2+}, Al^{3+}, Mg^{2+}, and Cd^{2+} [1,4].

In particular, the research interest in ZnO has been continuously rising since the theoretical prediction of room temperature ferromagnetism in Mn-doped zinc oxide DMS by Dietl et al. [30]. Among all the TM-doped ZnO systems, Mn doping is most concerned because of very high solubility in ZnO. The 'electron effective mass' is as large as approximately 0.3 m_e, where 'm_e' is the free-electron mass . Therefore, generated spins and carriers in the semiconductor are large, & making Mn-doped ZnO suitable for spintronic devices. A high-performance DMS with a high Curie temperature and magnetization is always desired in all practical devices.

However, until now, the mechanism involved in ferromagnetism is complicated and the reproducibility is still very challenging. Because several researchers have reported different

properties such as paramagnetism, antiferromagnetism, and ferromagnetism for Mn-doped zinc oxide [123-125],

6.1. Synthesis of ZnO and doping with Mn

$Zn_{1-x}Mn_xO$ films were synthesized with undoped ZnO, 8%, 12% and 15% of Mn by using the sol gel method. Zinc acetate dehydrate and manganese acetate tetrahydrate are dissolved in 2-methoxyethanol and then mono-ethanolamine is added to the solution. The concentration of metal ions in $Zn_{1-x}Mn_xO$ sols are controlled for each solution. MEA is added to keep the sol solutions stable and clear for a long period. 2-methoxyethanol is used as a solvent. The solution is stirred for 2 hr at 75ºC until a clear and homogenous sol is obtained. The spin coater was set to operate at around 3000 rpm. Before that, the substrate is cleaned using acetone, methanol and isopropanol in order to remove any dust, etc. These coated films are evaporated on hot plate The procedures from coating to drying and cooling were repeated several times until the thickness of the films was approximately 280 nm. The films were subjected to annealing at 500ºC for 2 hours to get pure as well as Mn doped ZnO thin films. Then after annealing, the thin film is ready for analyzing its optical and structural properties. The properties of the films depend on the chemistry of solutions, the nature of the substrate and ambient conditions during the films formation and thermal treatment. The coating techniques will influence the physical and optical properties of the films. The doped-material had different color from the white ZnO and was yellow with Mn doping.

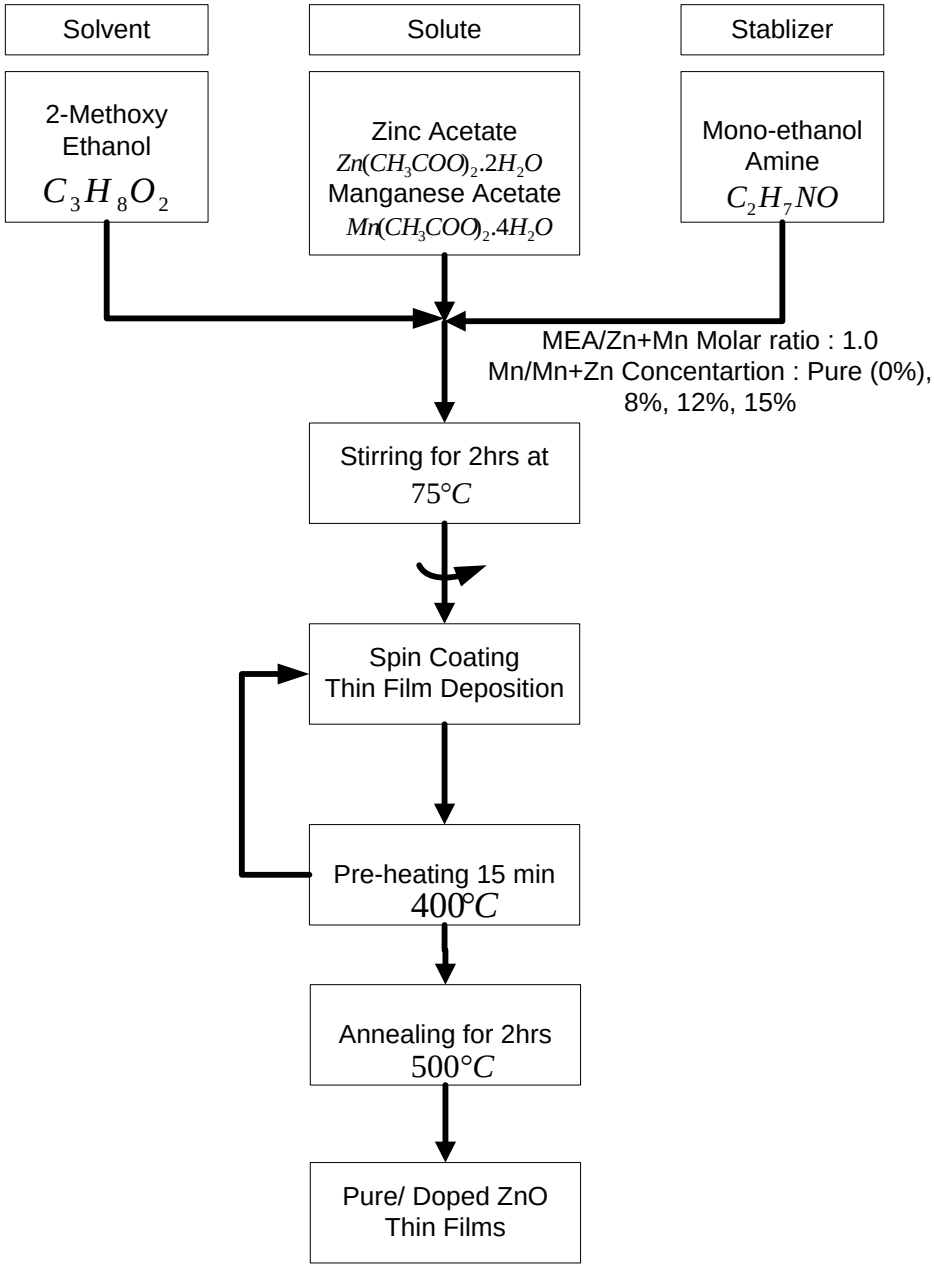

Figure 6-1: Synthesis of Pure/ Mn-doped ZnO thin films

6.2. Study of Structural properties of Mn-Doped ZnO thin films

An X-ray diffractometer was used to determine the crystallite phase and orientation. Figures 1 a-d show XRD-ray patterns of all samples which were deposited on glass substrates. The diffraction

patterns reveal good crystalline quality without any appreciable changes from pure ZnO films and are genuinely polycrystalline with a hexagonal wurtzite structure. These results imply that there are no secondary phases such as a manganese cluster or oxides. The average size of the undoped ZnO is found to be 40nm, and for 8, 12 and 15% Mn doped ZnO the average size is found to be 37, 34 and 29nm, respectively. The wide distribution of grain size of samples on the film can be the possible reason resulting in broadening the diffraction peaks. This may be due to the ionic radius of Mn^{2+} (0.83Å) that is larger than the ionic radius of Zn^{2+} (0.74Å). This phenomenon in the films creates strain or stress because of mismatching Mn^{2+} in the Zn^{2+}lattice site. However, the crystal quality of films decreases with an increase in the Mn percentage Zn site.

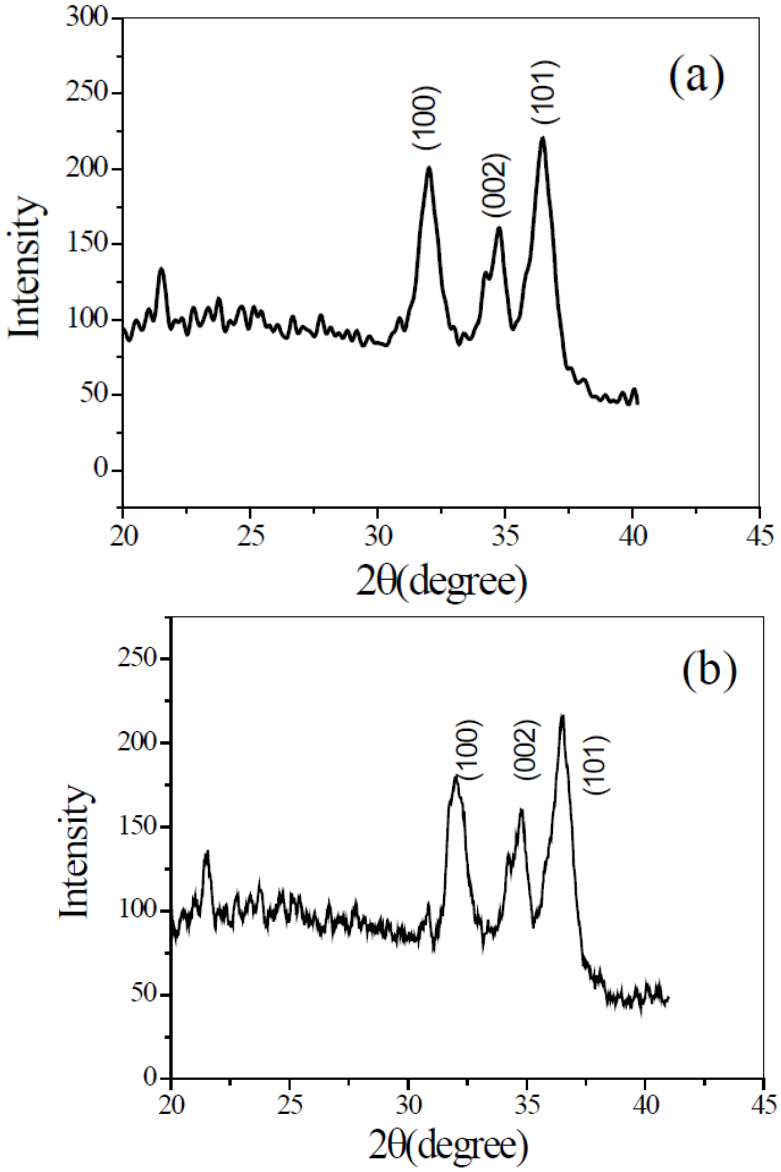

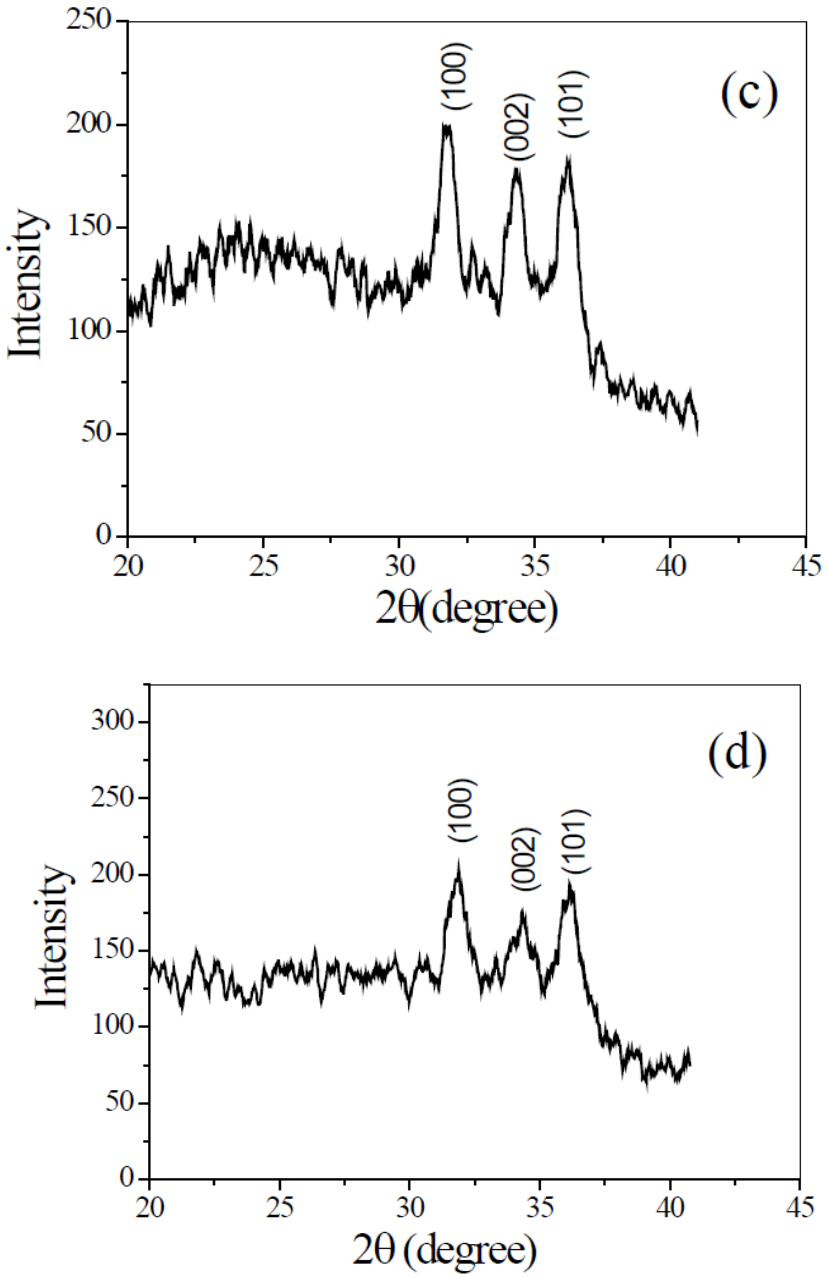

Figure 6-2 : X- Ray Differaction Spectra of different ZnO thin films (a) Pure ZnO, (b) 8% Mn Doping, (c) 12% Mn doping, (d) 15% Mn doping

Surface morphological studies of undoped and manganese doped ZnO films have been carried out using a scanning electron microscope. Figures 2 a-d show SEM images of an undoped and Mn doped ZnO film. The SEM images of ZnO resemble a granular surface. The incorporation of Mn ions changed surface morphology to a wrinkle network. The crystalline nature of films was affected due to the enhancement of dopant concentration, by which more impurities were included

in the ZnO crystal. For an Mn concentration of 12 at % the morphology of the film was neither wrinkle nor whiskers and for 15 at % of Mn concentration the morphology of the film changed to whiskers

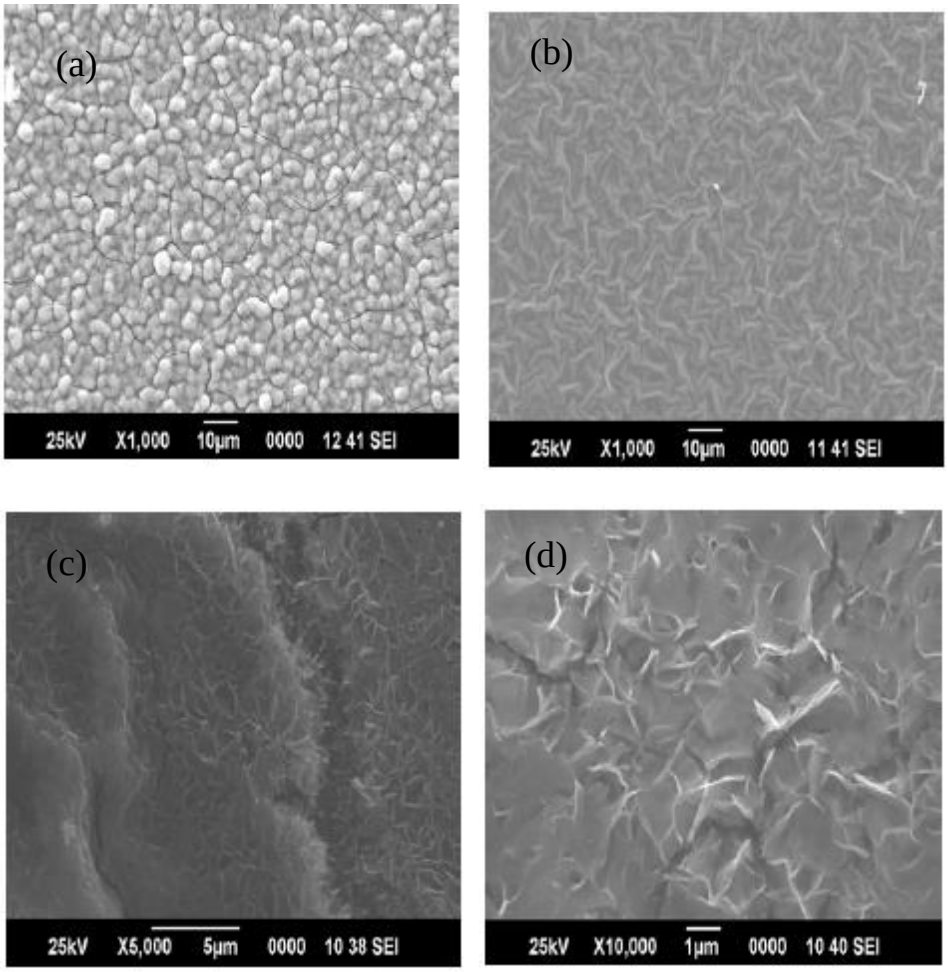

Figure 6-3 : SEM images of ZnO films (a) Pure ZnO (b) 8% Mn doping, (c) 12% Mn Doping (c) 12% Mn doping, (d) 15% Mn doping

6.3. Study of Electrical properties of Mn Doped ZnO thin films

The four point probe method was used to examine the electrical properties of the $Zn_{1-x}Mn_xO$ thin films and the results were listed in Table 6-1. The electrical conductivity of ZnO is related to the number of electrons, electrons formed by the ionization of interstitial zinc atom and the oxygen vacancies. Undoped ZnO has a highest resistivity and this value is decreasing as ZnO is doped with Mn. These changes are due of increasing Mn carrier concentration in the thin films.

However, a slight increase in resistivity for 12% of Mn compare to 8% Mn may be due to excessive Mn contents which increase the defects and the quality of the film crystal is degraded. At 15% of Mn, the resistivity value is the lowest (highest conductivity) and the films decrease quickly to 2.26 $x10^2$ Ω.cm. The resistivity will decrease as the thickness of the sample is increased.

Table 6-1: Resistivity of $Zn_{1-x}Mn_xO$ thin films

Samples	**Resistivity (Ω.cm)**
Pure ZnO	$5.80x10^2$
8% Mn	$3.82x10^2$
12% Mn	$2.57x10^2$
15% Mn	$2.26x10^2$

6.4. Study of Optical properties of Mn-Doped ZnO thin films

The optical properties of the films were studied from the transmittance spectra shown in Fig.6-4. With increase of 0, 8, 12, 15 at % manganese concentration, the optical transmittance spectra of the samples gradually increase in the visible region. The optical energy band gap shows a blue shift with increasing Mn doping concentrations. The optical band gaps have been calculated from the transmittance spectra and estimated by extrapolation of the linear relationship,

$$(\alpha h\upsilon)^2 = h\upsilon - E_g$$

Where α is the absorption coefficient, hν is the photon energy, Eg is the optical band gap of a nanofilm which is determined by the theory of direct optical absorption. Figure 4 shows the $(\alpha h\nu)^2$ vs. photon energy curves of a ZnO nanofilm with a varying doping concentration (see Table 6-2). The band gap value decreases with an increased Mn doping concentration which may due to the sp-d exchange interactions and has been theoretically explained using the second–order perturbation theory [126,127].

Table 6-2 : Band Gap measurement for Mn doped ZnO films

Dopant Mn concentration in ZnO	**Band gap Energy (E_g) [eV]**
0 %	3.27
8 %	3.26
12 %	3.24
15 %	3.20

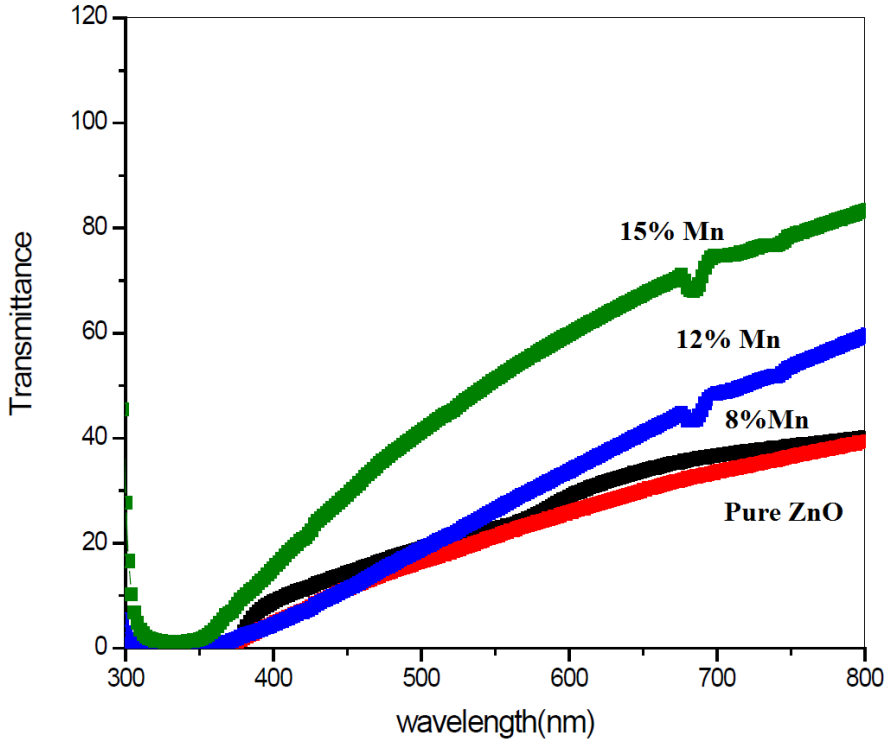

Figure 6-4 : Transmission Spectra of Mn doped ZnO films

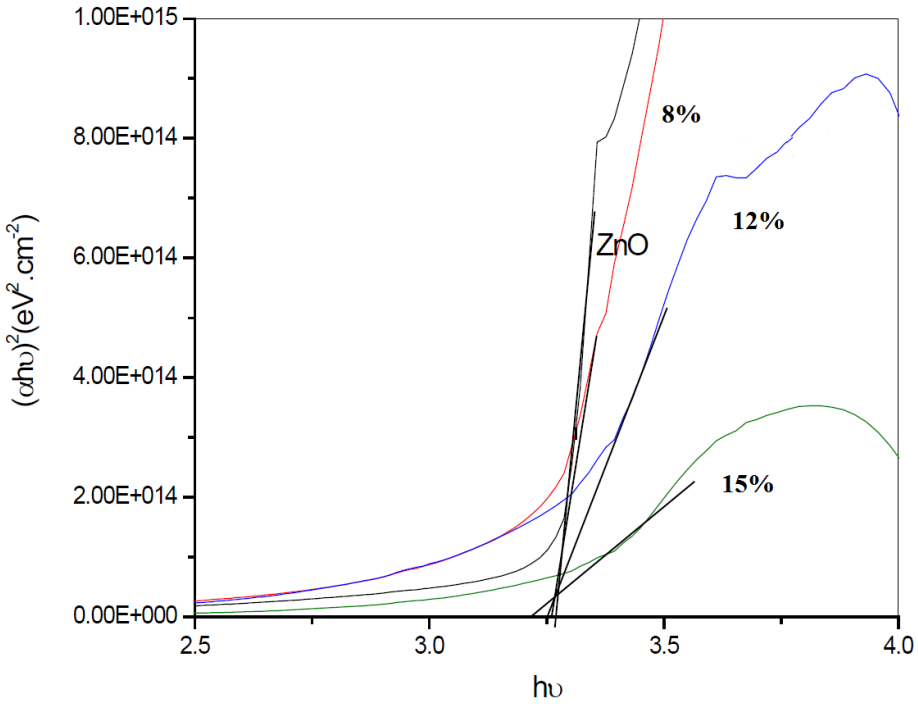

Figure 6-5 : Optical Band Gap for Mn doped ZnO

6.5. Study of Magnetic properties of Mn-Doped ZnO thin films

The magnetic properties were characterized using SQUID magnetometer equipped with a 7-T magnet in the temperature range of 4 to 400 K. Based on our theoretical studies, it was observed that Mn doped ZnO exhibit ferromagnetism for less than 10% Mn doping concentration. Hence we have prepared additional Mn doped ZnO thin films with 2% & 5% doping concentration. Figure 6a shows the magnetization of $Zn_{0.92}Mn_{0.08}O$ thin films as a function of temperature obtained at the zero-field-cooled [ZFC] and field-cooled [FC] processes with an applied magnetic field of 1,000 Oe. It is evident that the $Zn_{0.92}Mn_{0.08}O$ films are ferromagnetic with T_C higher than 300 K due to the clear separation between the FC and ZFC processes. The ZFC-FC magnetization curves (figure 6-6a) clearly reveals that the sample is stable without any superparamagnetism, as reported in [128]. further, magnetic hysteresis loops for the samples with three levels of Mn doping from SQUID measurements are shown in Figure 6-6b. The magnetization versus magnetic field [M-H] measurements for the Mn doped ZnO thin films with doping fraction x = 0.02, 0.05, and 0.08 at RT exhibit the coercive field of approximately more than 200 O. The coercivity reduces with rise in Mn doping level. The saturation magnetization values of the samples also increase with more Mn doping. However, magnetization per Mn atom still reduces with increasing content of doping. Similar phenomena have been observed in other DMS materials [129]. As discussed in theoretical study, the indirect exchange interactions among Mn^{2+} ions & carriers give rise to ferromagnetism, whereas direct interactions among them leads to anti-ferromagnetism. When Mn doping concentration is increased, the average distance between Mn^{2+} ions decreases, resulting in the enhancement of the antiferromagnetic contribution. Therefore room temperature ferromagnetism in the Mn-doped ZnO thin films can be attributed to the magnetic coupling between Mn atoms [130]

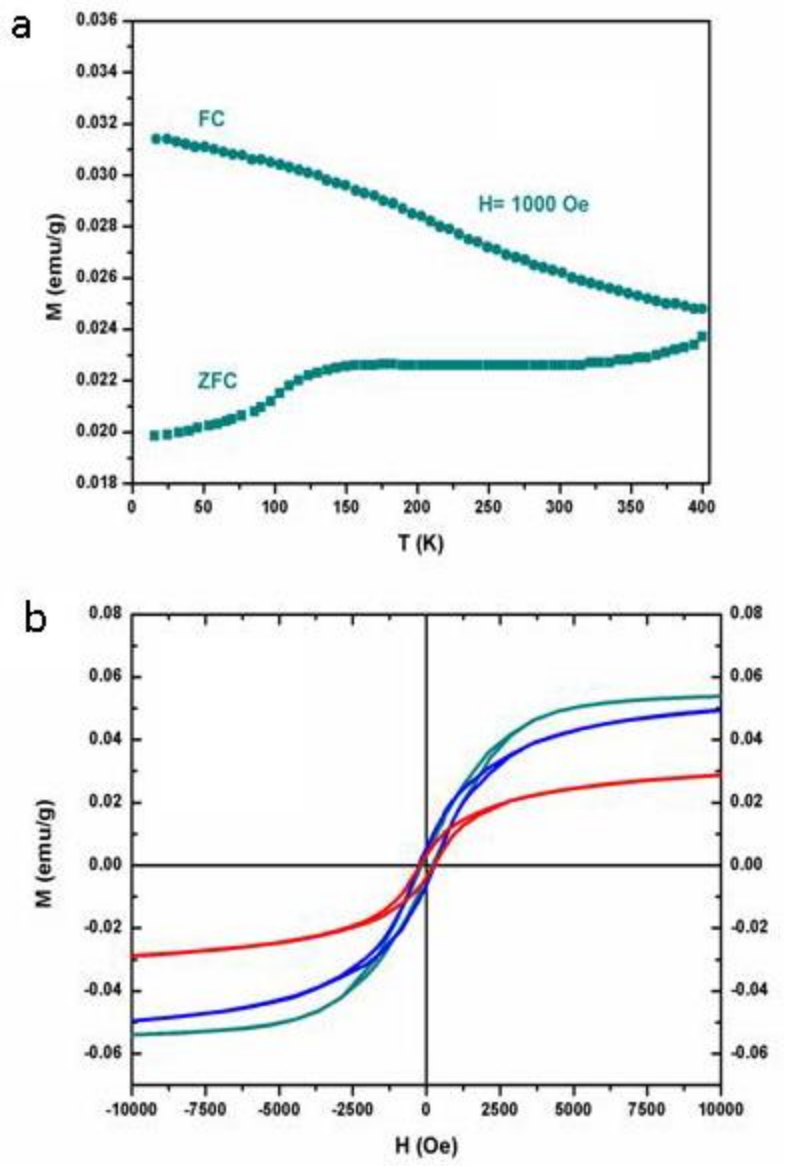

Figure 6-6 : (a) Magnetization vs Temperature curve for $Zn_{0.92}Mn_{0.08}O$ film for Zero field cooled & field cold modes (b) M-H curve at room temperature for Mn doped ZnO films (2%,5% & 8%)

CONCLUSION

In conclusion, transparent undoped and Mn doped ZnO thin films on glass substrates were prepared by a sol-gel method using a spin-coating method. The films were found to be highly c-axis oriented and the transmittance was increased in the visible region with increase of manganese. The thin films were characterized by XRD, SEM and ultraviolet-visible spectrophotometry, which indicate that Mn doped ZnO films have potential applications such as catalyst and transparent

electrodes in optoelectronic devices. Also the magnetic measurement reveals possibility of room temperature ferromagnetism in Mn doped ZnO thin films.

7. CONCLUSION & FUTURE WORK

7.1. Conclusion

The main objective of present investigation was to study theoretical aspects of dilute magnetic semiconductors and perform experimental studies on and transition metal (Mn and In) doped oxide based DMS (ZnO).

As initial part of theoretical study, various mechanisms for understanding origin of ferromagnetism in dilute magnetic semiconductors were studied & relationship between magnetization, curie temperature, doping & carrier concentration for TM doped DMS was simulated

- The analysis of simulation results revealed that maximum Curie temperature is obtained for optimum carrier density $n_c/n_i \sim 0.5 - 2$
- T_c first increases with concentrations for very low values of x after attaining it's maximum values it starts decreasing. T_c cannot be increased by just increasing magnetic impurity concentration for optimum carrier density (n_c/n_i) actually we have to maximize mean free path for obtaining maximum curie temperature.
- Also curie temperature depends upon type of magnetic impurity being doped however it affects amount of magnetization below curie temperature

This study was further extended to oxide based DMS (ZnO) & mechanism of ferromagnetism in Mn doped zinc oxide was studied for exploring room temperature ferromagnetism. The study revealed that

- The energy difference (FM –AFM) simulation for Zinc oxide system revealed that electron doping doesn't contribute in ferromagnetism. However hole doping contributes in ferromagnetism through exchange intractions.
- Although Mn doping in ZnO does not introduce carriers into the system so the system is expected to be antiferromagnetic, but addition of holes makes the system ferromagnetic because strong hybridization of the spin-up 3d states of Mn hybridize with the 2p (hole) states.
- The curie temperature was calculated for Mn doped ZnO system using Coey's sub-lattice mode & was estimated to be near room temperature (250K)

Subsequently a theoretical study on optically induced ferromagnetism in DMS was performed for understanding effects of optical radiation on TM doped DMS.

- Analysis of Photo-Induced Magnetization TM doped DMS using Mean Field theory revealed that free energy of system decreases with magnetization when energy of incident light is increased.
- The simulation results for magnetization of Mn doped DMS system revealed that curie temperature is increased when energy of coupling light & doping concentration of Mn is increased

As a part of experimental study, transition metal (Indium & Magnanese) doped zinc oxide thin films were prepared using sol-gel method. The thin films were subjected to structural, electrical, optical & magnetic characterization using XRD, SEM, UV-Visible spectroscopy & SQUID techniques.

The Indium-doped ZnO thin films having different doping concentrations viz. 1%, 2%, 5% & 10% were synthesized by using sol–gel spin-coating method with for transparent conducting oxide applications and their electrical, structural & optical properties were studied.

- All films had a crystal structure, and a minimum sheet resistivity of 3.1×10^{-3} Ω.cm for In doped ZnO thin film at 5% doping level.
- In XRD patterns for different films, only a strong (0002) peak was observed, no additional diffraction peak was detected. The 0002 peaks indicate that the films are highly oriented with their crystallographic c-axis perpendicular to the substrate. The full width half maximum (FWHM) observations for different doping concentration revealed deterioration of crystallinity of the films at higher doping concentrations (>5%), which may be effect of the formation of the compressive stresses due to more ions.
- Analysis of TSDC spectra for In doped ZnO thin films revealed two to three peaks at 400,425 & 450^{o}C, one at low temperature (β peak), which is associated with dipolar relaxation, and other at higher temperature (α peak) that appears due to space charge relaxation. When polarizing field was increased, the magnitudes of both peaks increased
- Additionally, the optical transmittance observations using UV-Visible spectroscopy show a very good transmittance (> 90%) within the visible wavelength region which

suggests that In doped ZnO thin films can be very good candidates for transparent conducting oxides

The pure as well as Manganese (Mn)-doped ZnO thin films having 8%, 12% & 15% Mn doping concentration were prepared by using sol–gel spin-coating technique for electronic & optoelectronic applications. The structural, optical & electrical properties of these thin films were studied.

- The XRD patterns for Mn doped ZnO films revealed peaks at 31.7, 34.4 & 36.2 degree (2θ). The diffraction patterns reveal good quality with minor deviation from pure ZnO films.
- The measured value of average grain size of the pure ZnO is approx.. 40nm. For 8, 12 and 15% Mn doped ZnO the average size is found to be 37, 34 and 29nm, respectively. The wide distribution of grain size of samples on the film can be the possible reason resulting in broadening the diffraction peaks.
- The SEM images of ZnO reveal that incorporation of Mn ions changed surface morphology to a wrinkle network & with further enhancement of doping concentration it got changed to whiskers.
- The study of electrical properties of the $Zn_{1-x}Mn_xO$ thin films using four probe method, revealed that electrical resistivity decreases with increase in Mn doping concentration. ZnO films with 15% doping were found to have minimum resistivity.
- The optical transmittance spectra of the samples shows gradually increase in in transmittance in visible region. The optical transmittance of Mn doped ZnO samples increases with dpoing concentrations.
- The optical band gaps were calculated from the transmittance spectra and estimated by extrapolation of the linear relationship & shows a blue shift with increasing Mn doping concentrations
- The magnetic measurements revealed possibility of room temperature ferromagnetism in Mn doped ZnO thin films.

7.2. Future Work

The oxide based dilute magnetic semiconductors especially ZnO is a highly promising material which can be utilized in variety of applications such as optical sensing, antibacterial and biomedical, photovoltaic, gas sensing, optoelectronic & spintronic devices. In this study, ZnO was doped with Mn and In. In the future work, other oxide based DMS such as SnO_2, TiO_2 etc. can be investigated and the effect of doping with other elements such as Cr, Co, Ni etc can be studied. Also doping with Rare Earth elements can be studied in future for exploring the possible applications in solar cells and biological imaging etc. Further this study may be extended toward fabricating spintronic devices such as spin LED, spin Transistors etc.

LIST OF PUBLICATIONS

1. **H.S. Kaushik**, Anuradha Sharma, Mamta Sharma, **"Dilute Magnetic Semiconductor: A Review of Theoretical Status"**, International Journal of IT, Engineering and Applied Sciences Research (IJIEASR), 26 (2016) 10330-10335.

2. **Hari Shankar Kaushik**, Anuradha Sharma, and Mamta Sharma, **"Study of Room Temperature Ferromagnetism in DMS"**, Conference on Science in Media (SIM) , YMCA University, Faridabad, 2012.

3. **Hari Shankar Kaushik**, Anuradha Sharma, and Mamta Sharma, **"Optically Induced Ferromagnetism in III-V Dilute Magnetic Semiconductors"**, Integrated Ferroelectronics, Vol. 203, 2019, 67-73.

4. **Hari Shankar Kaushik**, Anuradha Sharma, and Mamta Sharma , **"Studies on In-Doped ZnO Transparent Conducting thin Films"**, International Journal of Research in Engineering and Science (IJRES), Vol. 5, 2017, 74-76

5. **Hari Shankar Kaushik**, Anuradha Sharma, and Mamta Sharma , **"Evaluation of Mn doped Zinc oxide dilute magnetic semiconductor"**, International Journal of Advanced Research in Science & Engineering (IJARSE), Vol. 7, Issue 3, 2018, 519-521

REFERENCES

1. S. A. Wolf *et al.*, "Spintronics: a spin-based electronics vision for the future," Science 294, 1488-95 (2001).
2. Gary A. Prinz, "Magnetoelectronics," Science 282, 1660-1663 (1998).
3. H. Ohno, "Making nonmagnetic semiconductors ferromagnetic," Science 281, 951-6 (1998).
4. R. N. Gurzhi, A. N. Kalinenko, A. I. Kopeliovich, et al., Appl. Phys. Lett. 83 4577 (2003).
5. J. Rudolph, D. Hagele, H. M. Gibbs et al., Appl. Phys. Lett. 82 4516 (2003).
6. S. J. Pearton, D. P. Norton, M. P. Ivill, A. F. Hebard, J. M. Zavada, W. M. Chen, and I. A. Buyanova, ZnO doped with transition metal ions, IEEE Transactions on electron Devices, Vol. 54, No. 5, 1040-1048 (2007).
7. S. Singh et al, Structure, microstructure and physical properties of ZnO based materials in various forms: bulk, thin film and nano, J. Phys. D: Appl. Phys. 40, 6312-6327 (2007).
8. J. Kang, S. Tsunekawa, and A. Kasuya, Appl. Surf. Sci. 174, 306 (2001).
9. H. Tang, H. Berger, P. E. Schmid and F. Levy, Solid State Commun. 92 267 (1994).
10. D. Jiles, Introduction to Magnetism and Magnetic Materials, Chapman & Hall, New York, 1991.
11. M. Getzlaff, Fundamentals of Magnetism, Springer, Berlin, 2008
12. Z. L. Wang, Y. Liu, and Z. Zhang, Handbook of nanophase and nanostructured materials, Kluwer Academic, New York, 2003
13. J. Stöhr and H. C. Siegmann, Magnetism: From Fundamentals to Nanoscale Dynamics, Springer, Berlin, 2006.
14. S. Methfessel and D. C. Mattis, in *Magnetism, Magnetic Semiconductors*, vol. XVIII/1 of *Encyclopedia of Physics*, 389562 (1968)
15. M. A. Ruderman and C. Kittel, Physical Review 96 (1954) 99.
16. T. Kasuya, Progress of Theoretical Physics 16 (1956) 45.
17. K. Yosida, Physical Review 1 (1957) 893.
18. H. Ohno, A. Shen, F. Matsukura, A. Oiwa, A. Endo, S. Katsumoto, and Y. Iye, Applied Physics Letters 69 (1996) 363.

19. H. Ohno and F. Matsukura, Solid State Communications 117 (2001) 179.
20. P. Mahadevan and A. Zunger, Applied Physics Letters 85 (2004) 2860.
21. C. Zener, Physical Review 82 (1951) 403.
22. H. Akai, Physical Review Letters 81 (1998) 3002.
23. H. A. Kramers, Physica 1 (1934) 182.
24. P. W. Anderson, Physical Review 79 (1950) 350.
25. M. Zajac, J. Gosk, M. Kaminska, A. Twardowski, T. Szyszko, and S. Podsiadlo, Applied Physics Letters 79 (2001) 2432.
26. A. Bonanni, Semiconductor Science and Technology 22 (2007) R41.
27. J. M. D. Coey, M. Venkatesan, and C. B. Fitzgerald, Nat Mater 4 (2005) 173.
28. M. Venkatesan, C. B. Fitzgerald, J. G. Lunney, and J. M. D. Coey, Physical Review Letters 93 (2004) 177206.
29. V. Litvinov and V. Dugaev, Physical Review Letters 86 (2001) 5593.
30. T. Dietl, H. Ohno, F. Matsukura, J. Cibert, and D. Ferrand, Science 287, 1019 (2000)
31. N. Y. H. Hong, J. Sakai, and A. Hassini, Appl. Phys. Lett. 84, p. 26022604 (2004)
32. Adam C. Durst, R. N. Bhatt, and P. A. Wolfi, Phys. Rev. B, 65, p. 235205 (2002).
33. V. Canella and J.A. Mydosh, Phys. Rev. B 6, p. 4220 (1972).
34. W. E. Hoke, P. J. Lemonias, and D. G. Weir, J. Cryst. Growth 111, 1024 (1991).
35. T. L. Tansley and C. P. Foley, J. Appl. Phys. 59, p. 3241 (1986).
36. J. Wu, W. Walukiewicz, K. M. Yu, J. W. Ager III, E. E. Haller, H. Lu, W. J. Schafi, Y. Saito, and Y. Nanishi, Appl. Phys. Lett. 80, p. 3967 (2002).
37. K Ueda, H Tabata and T Kawai., *Magnetic and electric properties of transition metal doped ZnO films*, Applied Physics, 2001, Vol. 79, p. 988.
38. Rajaram, Rekha. *Study of magnetism in dilute magnetic semiconductors based on iii-v Nitrides*. Stanford university, 2007, Ph.D Thesis.

39. Vu Kim Thai, Hoang Anh Tuan. Hanoi : s.n., *Curie temperature of diluted magnetic semiconductors: the influence of the antiferromagnetic exchange interaction*. Proceedings National Conference on Theoreical Physics, 2011, pp. 108-113.
40. S. Das Sarma, E. H. Hwang, S. A. Kaminski, *Enhancing Tc in Ferromagnetic Semiconductors*, Physics Rev., 2003, Vol. B67, pp. 1-4.
41. Mathieu Malfait, *Magnetic and transport properties of (Ga,Mn)As diluted magnetic semiconductor*, Doctoral Dissertation, Katholieke University Leuven (2005).
42. H. Ohno, F. Matsukura and Y. Ohno, Magnetic properties of (Al,Ga,Mn)As, *JSAP International* **5**,(2002).
43. T. Dietl, Jurgen Konig, A. H. MacDonald, Magnetic domains in III-V magnetic semiconductors, *Phys. Rev.* **B 64**, 241201 (2001).
44. S. K. Kamilla and S Basu, New semiconductor materials for magnetoelectronics at room temperature, *Bull. Mater. Sci.* **Vol. 25, No. 6**, pp. 541-543, November (2002).
45. T. Komori, T. Ishikawa, T. Kuroda J. Yoshino, F. Minami and S. Koshihara, Carrier-density dependence of magnetic and magneto-optical properties of (Ga,Mn)As, *Phys. Rev.* **B 67**, 115203 (2003).
46. Debjani Karmakar, S. K. Mandal, R. M. Kadam, P. L. Paulose, A. K. Rajarajan, T. K. Nath, A. K. Das, I. Dasgupta and G. P. Das, Ferromagnetism in Fe-doped ZnO nanocrystals: Experiment and theory, *Phys. Rev*. **B 75**, 144405 (2007)
47. S. Das Sarma, *American Scientist*, Spintronics, 89 (2001).
48. N. N. Bogoliubov, V. V. Tolmachov, and D. V. Sirkov, The theory of Superconductivity, *Fortschritte der Physik*, **6**, 605 (1958).
49. L. V. Kjeldysh and A. N. Kozlov, Collective Properties of Excitons in Semiconductors. *Sov. Phys.-JETP* **27**, 521 (1968).
50. Roman Kochetov , *Investigations of GaAs based hetrostructure for spintronics*, Master's Thesis, Lappeenrant University (2007).
51. H. Krenn, W. Zawadzki, and G. Bauer, Optically Induced Magnetization in a Dilute Magnetic Semiconductor: $Hg_{1-x}Mn_xTe$, *Phys. Rev. Lett.* **55**, 1510(1985).
52. Subodha Mishra, Gouri Shankar Tripathi and Sashi Satpathy, Theory of photoinduced ferromagnetism in dilute magnetic semiconductors, *Phys. Rev.* **B 77**, 125216 (2008).

53. A.V. Kimel, G.V. Astakhov, G.M. Schott, A. Kirilyuk, D. R.Yakovlev, G. Karczewski, W. Ossau, G. Schmidt, L.W. Molenkamp, and Th. Rasing, Picosecond Dynamics of the Photoinduced Spin Polarization in Epitaxial (Ga,Mn)As Films, *Phys. Rev Lett.* **92**, 237203(2004)
54. Y. Mitsumori, A. Oiwa, T. Slupinski, H. Maruki, Y. Kashimura, F. Minami, and H. Munekata, Photo-induced spin dynamics in ferromagnetic semiconductor p-(Ga,Mn)As, *Phys. Rev.* **B 69**, 033203(2004).
55. J. Wang, I. Cotoros, K. M. Dani, X. Liu, J. K. Furdyna, and D. S. Chemla, Ultrafast Enhancement of Ferromagnetism via Photoexcited Holes in GaMnAs, *Phys. Rev. Lett.* **98**, 217401 (2007).
56. C. Piermarocchi, Pochung Chen, and L. J. Sham and D.G. Steel, Optical RKKY Interaction between Charged Semiconductor Quantum Dots, *Phys. Rev. Lett.* **89**, 167402(2002)
57. Subodha Mishra, Gouri Shankar Tripathi and Sashi Satpathy, Theory of photoinduced ferromagnetism in dilute magnetic semiconductors, *Phys. Rev.* **B 77**, 125216 (2008).
58. Y. Mitsumori, A. Oiwa, T. Slupinski, H. Maruki, Y. Kashimura, F. Minami, and H. Munekata, Photo-induced spin dynamics in ferromagnetic semiconductor p-(Ga,Mn)As, *Phys. Rev.* **B 69**, 033203(2004).
59. J. Wang, I. Cotoros, K. M. Dani, X. Liu, J. K. Furdyna, and D. S. Chemla, Ultrafast Enhancement of Ferromagnetism via Photoexcited Holes in GaMnAs, *Phys. Rev. Lett.* **98**, 217401 (2007).
60. C. Piermarocchi, Pochung Chen, and L. J. Sham and D.G. Steel, Optical RKKY Interaction between Charged Semiconductor Quantum Dots, *Phys. Rev. Lett.* **89**, 167402(2002)
61. F. Bassani and G. P. Parravicini, Electronic states and optical transitions in solids, *Pergamon New York*, 151, (1975).
62. T. Jungwirth, K. Y. Wang, J. Maˇsek, K. W. Edmonds, J¨urgen K¨onig, Jairo Sinova, M. Polini, N. A. Goncharuk, A. H. MacDonald, M. Sawicki, A. W. Rushforth, R. P. Campion, L. X. Zhao, C. T. Foxon, and B. L. Gallagher, Prospects for high temperature ferromagnetism in (Ga,Mn)As semiconductors, *Phys. Rev.* **B 72**, 165204 (2005)
63. L. Bergqvist, P. A. Korzhavyi, B. Sanyal, S. Mirbt, I. A. Abrikosov, L. Nordstr¨om, E. A. Smirnova, P. Mohn, P. Svedlindh, and O. Eriksson, Magnetic and electronic structure of $Ga_{1-x}Mn_xAs$, *Phys. Rev.* **B 67**, 205201 (2003).

64. K. M. Yu, W. Walukiewicz, T. Wojtowicz, I. Kuryliszyn, X. Liu, Y. Sasaki, and J. K. Furdyna, Effect of the location of Mn sites in ferromagnetic $Ga_{1-x}Mn_xAs$ on its Curie temperature, *Phys. Rev.* **B 65**, 201303 (2002).
65. Fekadu Gochole, *Photo Induced Ferromagnetism and Mechanism of Ferromagnetism in Diluted Magnetic Semiconductor*, Addis Ababa University,2010.
66. Subodh Mishra, *Theory of Photo-Induced Ferro-Magnetism in Dilute Magnetic Semiconductors*, University of Missouri-Columbia, 2006.
67. S. Das Sarma, Spintronics, *American Scientist Vol.*-**89**, 561 (2001).
68. N. N. Bogoliubov, V. V. Tolmachov, and D. V. Sirkov, The theory of Superconductivity, *Fortschritte der Physik*, **6**, 605 (1958).
69. J. Fernandez-Rossier, C. Piermarocchi, P. Chen, A. H. MacDonald, and L. J. Sham, Coherently Photoinduced Ferromagnetism in Diluted Magnetic Semiconductors, *Phys. Rev. Lett.* **93**, 127201(2004)
70. H. Krenn, W. Zawadzki, and G. Bauer, Optically Induced Magnetization in a Dilute Magnetic Semiconductor: Hg1-xMnxTe, Phys. Rev. Lett. 55, 1510(1985).
71. K. M. Yu, W. Walukiewicz, T. Wojtowicz, I. Kuryliszyn, X. Liu, Y. Sasaki, and J. K. Furdyna, Effect of the location of Mn sites in ferromagnetic Ga1−xMnxAs on its Curie temperature, Phys. Rev. B 65, 201303 (2002).
72. K. SATO and H. KATAYAMA-YOSHIDA, Japan. J. Appl. Phys. 40 (2001) L334.
73. K. SATO and H. KATAYAMA-YOSHIDA, Semiconductor Science & Technology 17 (2002) 367.
74. P . SHARMA, A. GUPTA, K. V. RAO, F . J . OWENS, R. SHARMA, R.AHUJA, J . M. OSORIO GUILLEN, B. JOHANSSON and G. A. GEHRING, Nat. Mater. 2 (2003) 673.
75. E. -C. LEE and K. J . CHANG, Phys. Rev. B 69 (2004) 085205.
76. Q. WANG and P . JENA, Appl. Phys. Lett. 84 (2004) 4170.
77. Q. WANG, Q. SUN, B. K. RAO and P . JENA, Phys. Rev. B 69 (2004) 233310.
78. Y. Abdollahi, A. Abdullah, Z. Zainal, and N. Yusof, International Journal of Basic and Applied Sciences, 11 (2011) 62–69.
79. Parmanand Sharmaa, Amita Gupta b, Frank J. Owensc,Akhisha Inoued, K.V. Rao b, Journal of Magnetism and Magnetic Materials 282 (2004) 115–121.

80. J. L. Costa-Krämer, F. Briones, J. F. Fernández, A. C. Caballero, M. Villegas, M.Díaz, M. A. García, A. Hernando, Nanotechnology 16 (2005) 214.
81. M. A. García, M. L. Ruiz-González, A. Quesada, J. L. Costa-Krämer, J. F.Fernández, S. J. Khatib, A. Wennberg, A. C. Caballero, M. S. Martín-González, M.Villegas, F. Briones, J. M. González-Calbet, A. Hernando, Phys. Rev. Lell. 94(2005) 217206.
82. Kittilstved K. R, Norberg N. S, Gamelin D. R, Phys. Rev.Lett. 94 (2005), 147209.
83. Sharma P, Gupta. A, Rao KV, Owens FJ, Sharma R, Ahuja R, Guillen JM, Johansson B, Gehring GA, Nature Materials,2,(2003), 673-677.
84. C. Klingshirn, ZnO: From basics towards applications, Phys. Stat. Sol. (b) 244 No. 9, 3027-3073 (2007).
85. C. Klingshirn, ZnO: Material, physics and applications, ChemPhysChem 8, 782-803 (2007).
86. Ü. Özgür, Ya. I. Alivov, C. Liu, A. Teke, M. A. Reshchikov, S. Doan, V. Avrutin, S. J. Cho, and H. Morkoç, A comprehensive review of ZnO materials and devices, Journal of Applied Physics 98, 041301 (2005).
87. H. Morkoc and U. Ozgur, General properties of ZnO, Zinc Oxide: Fundamentals, materials and device technology, WILEY-VCH Verlag (2009) p.1-2.
88. A. B. Djurisic, and Y. H. Leung, Optical properties of ZnO nanostructures, Small 2, No. 8-9, 944-961 (2006).
89. M. Willander et al, Zinc oxide nanorod based photonic devices: recent progress in growth, light emitting diodes and lasers, Nanotechnology 20, 332001(40page) (2009).
90. Ohring, Milton. Materials Science of Thin Films. Academic Press. p. 215.
91. S. Ghosh, G. G. Khan and K. Mandal, ACS Appl. Mater. Interfaces, 4, 2048 (2012).
92. Pulsed Laser Deposition of Thin Films, edited by Douglas B. Chrisey and Graham K. Hubler, John Wiley & Sons, 1994.
93. Shaban, Z.; Ara, M.H.M.; Falahatdoost, S.; Ghazyani, N. Optimization of ZnO thin film through spray pyrolysis technique and its application as a blocking layer to improving dye sensitized solar cell efficiency.Curr. Appl. Phys. 2016, 16, 131–134
94. Mahadik, M.A.; Hunge, Y.M.; Shinde, S.S.; Rajpure, K.Y.; Bhosale, C.H. Semiconducting properties of aluminum-doped ZnO thin films grown by spray pyrolysis technique. J. Semicond. 2015, 36, 033002.

95. Michaelis, E.;Wohrle, D.; Rathousky, J.;Wark, M. Electrodeposition of porous zinc oxide electrodes in the presence of sodium laurylsulfate. Thin Solid Films 2006, 497, 163–169.
96. Kim, Y.K.; Hwang, S.H.; Kim, S.; Park, H.; Lim, S.K. ZnO nanostructure electrodeposited on flexible conductive fabric: A flexible photo-sensor. Sens. Actuators B Chem. 2017, 240, 1106–1113.
97. R. Karmakar, S. K. Neogi, A. Banerjee, and S. Bandyopadhyay, "Structural; morphological; optical and magnetic properties of Mn doped ferromagnetic ZnO thin film," Applied Surface Science, vol. 263, pp. 671–677, 2012.
98. S. Yang and Y. Zhang, "Structural, optical and magnetic properties of Mn-doped ZnO thin films prepared by sol–gel method," Journal of Magnetism and Magnetic Materials, vol. 334, pp. 52–58, 2013.
99. M. Guglielmi, G. Carturan, J. Non-Cryst. Solids 100 16–30, (1988).
100. L. Armelao, M. Fabrizio, S. Gialanella, F. Zordan, Thin Solid Films 394, 90–96 (2001).
101. D. Meyerhofer, J. Appl. Phys., 49 (7), 3993 (1978).
102. Huang, Yuhong Zheng, Haixing; and Forsyth, Ian, Ultrafine and Nano Powders, Oct. 29-31, Montreal, Canada (2000).
103. David E.Skinner, Philip Colombo Jr. D.Joseph J.Cavaleri, Robert M.Bowman,The Journal of Physical Chemistry, 7853–7856, (1995) 99.
104. K.L.Chopra, P.D.Paulson and V.Dutta, Progress in Photovoltaic, Research and Applications, 12 (2004) 69.
105. Mark Bachman, Glass substrates cleaning, INRF application note, (1999)
106. M. Guglielmi, G. Carturan, J. Non-Cryst. Solids 100 16–30, (1988).
107. L. Armelao, M. Fabrizio, S. Gialanella, F. Zordan, Thin Solid Films 394, 90–96 (2001).
108. http://www.absoluteastronomy.com/topics/X-ray_crystallography, 10 October 2014.
109. http://prism.mit.edu/xray/oldsite/training.htm#chronological, 10 October 2014.
110. M. Birkholz, Principles of X-ray Diffraction, Thin film analysis by X-ray scattering, WILEY-VCH Verlag GmbH & Co. KGaA, Weinheim, (2006) pp.10-11.
111. B.D.Cullity and S.R Stock, Elements of X- ray diffraction, third edition, Prentice Hall, New Jersey (2001).

112. H Gunther Rudenberg and Paul G Rudenberg (2010). "Origin and Background of the Invention of the Electron Microscope: Commentary". Advances in Imaging and Electron Physics (Elsevier) 160.
113. C. D. Wagner, W. M. Riggs, L. E. Davis, J. F. Moulder, G. E. Muilenberg, in Handbook of X-ray Photoelectron Spectroscopy, edited by G. E. Muilenburg (Perkin Elmer, Eden Prairie, 1979).
114. http://www.physicsforums.com/showthread.php
115. J.K.Furdyna, Diluted Magnetic Semiconductors, J. Appl. Phys. 64 (1988) R29.
116. S. Ghosh, G. G. Khan and K. Mandal, EPJ Web of Conferences 40, 03001 (2013)
117. J. Clarke and A. I. Braginski (Eds.) (2004). The SQUID handbook 1. Wiley-Vch.
118. R. C. Jaklevic, J. Lambe, A. H. Silver, and J. E. Mercereau (1964). "Quantum Interference Effects in Josephson Tunneling". Phys. Rev. Letters 12 (7): 159–160
119. Ohyama M, Kozuka H, Yoko T: Sol–gel preparation of transparent and conductive aluminum-doped zinc oxide films with highly preferential crystal orientation. J Am Ceram Soc 1998, 81: 1622.
120. Sub ES, Kang HS, Kang JS, Kim JH, Lee SY: Effect of the variation of film thickness on the structural and optical properties of ZnO thin films deposited on sapphire substrate using PLD. Appl Surf Sci 2002, 186: 474.
121. Luna-Arredondo E.J., Maldonado A., Asomoza R., Acosta D.R., Meléndez-Lira M.A. and Olvera. M. de la L. (2005). Indium-doped ZnO thin films deposited by the sol–gel technique. Thin Solid Films 490, 132.
122. Li H., Wang J., Liu H., Yang C., Xu H., Li X. and Cui H. (2004). Sol–gel preparation of transparent zinc oxide films with highly preferential crystal orientation. Vacuum 77, 57
123. Liu J, Wang K, Yu M, Zhou W: Room-temperature ferromagnetism of Mn doped ZnO aligned nanowire arrays with temperature dependent growth. J Appl Phys 2007, 102:024301-024306.
124. Cheng X, Chien C: Magnetic properties of epitaxial Mn-doped ZnO thin films. J Appl Phys 2003, 93:7876-7878.
125. Yoon S, Cho S, We S, Yoon S, Suh B, Song H, Shin Y: Magnetic properties of ZnO-based diluted magnetic semiconductors. J Appl Phys 2003, 93:7879-7881.
126. P. Singh, A. Kaushal, D. Kaur, J. Alloys and Compounds 471, 11 (2009).

127. R.B. Bylsma, W.M. Becker, J. Kossut, U. Debsta, Phys. Rev B 33, 8207 (1986).
128. Jayakumar O, Sudakar C, Vinu A, Asthana A, Tyagi A: Effect of surfactant treatment on the magnetic properties of Mn-doped ZnO bulk and nanoparticles. J Phys Chem C 2009, 113:4814-4819.
129. Venkatesan M, Fitzgerald C, Lunney J, Coey J: Anisotropic ferromagnetism in substituted zinc oxide. Phys Rev Lett 2004, 93:177206.
130. Lin X, Zhu Y, Shen W: Synthesis and optical and magnetic properties of diluted magnetic semiconductor $Zn_{1-x}Mn_xO$ hollow spherical structures. J Phys Chem C 2009, 113:1812-1817.
131. Lijuan Zhao, Bei Zhang, and Qi Pang et al., Appl. Phys. Lett. 89, 092111 (2006).
132. T. Story, in Proc. Intl. Workshop on Dluted Magnetic Semiconductors (Linz 1994).
133. Y. Matsumoto, M. Murakami, T. Shono et al., Science 291 854 (2001).
134. H.J.Lee and S.Y.Jeong, C.R.Cho, C.H.Park, Appl. Phys. Lett. 81 (2002) 4020.
135. K.Ando, H.Saito, Zhengwu Jin, T.Fukumura, M.Kawasaki, .Matsumoto, H.Koinuma, Appl. Phys. Lett. Vol. 78 (2001) 2700.
136. Z.Jin, T.Fukumura, M.Kawasaki, K.Ando, H.Saito, T.Sekiguchi, Y.Z.Yoo, M.Murakami, Y.Matsumoto, T.Hasegawa, H.Koinuma, Appl. Phys. Lett. 78 (2001) 3824.
137. H.Saeki, H.Tabata and T.Kawai, Solid State Commun. 120 (2001) 439.
138. D.A.Schwartz, K.R.Kittilstved and D.R.Gamelin, Appl. Phys. Lett. 85 (2004) 1395.
139. S.J.Han, J.W.Song, C.H.Yang, S.H.Park, J.H.Park, Y.H.Jeong and K.W. Rhie, Appl. Phys. Lett. 81 (2002) 4212.
140. J.Shim, T.Hwang, S.Lee, J.H.Park, S.J.Han and Y.H.Jeong, Appl. Phys. Lett. 86 (2005) 082503.
141. Yen-Fa Liaoa, Tzu-Wen Huanga, journal of magnetism and materials 818-820 (2007) 310.
142. Yi Wang, Lei Sun, Ling-Kon, Journal of Alloys and Compounds 256-259 (2006) 423.
143. T.Fukumura, Z.Jin, M.Kawasaki, T.Shono, T.Hasegawa, S.Koshihara, Appl. Phys. Lett, 78 (2001) 958.
144. K.Sato, H.K.Yoshida, Material Design for Transparent Ferro magnets with ZnOBased Magnetic Semiconductors, Japan. J. Appl. Phys. 39 (2000) 555.

145. S.W.Jung, S.J.An, G.C.Yi, C.U.Jung, S.I.Lee, S.Cho, Appl. Physic. Letters, 80 (2002) 4561.
146. E. Della Gaspera, M. Guglielm , G. Perotto, S. Agnoli, G. Granozzi, M.L. Post, A. Martucci , CO optical sensing properties of nanocrystalline ZnO–Au films: Effect of doping with transition metal ions, Sensors and Actuators B: Chemical , Volume 161, Issue 1, Pages 675–683 , (2012).
147. Ekaterina Badaeva, Joseph W. May, Jiao Ma, Daniel R. Gamelin, and XiaosongLi ,Characterization of Excited-State Magnetic Exchange in Mn2+-Doped ZnO Quantum Dots Using Time-Dependent Density Functional Theory ,*J. Phys. Chem. C*, *115* , pp 20986–20991 , (2011).
148. Lin-Juan Zhang ,Jian-Qiang Wang , Jiong Li , Jing Zhou , Wu-Peng Cai, Jie Cheng , Wei Xu , Guangzhi Yin , Xiang Wu , Zheng Jiang , Shuo Zhang and Zi-Yu Wu ,High-Tc ferromagnetism in a Co-doped ZnO system dominated by the formation of a zinc-blende type Co-rich ZnCoO phase , Chem. Commun., 48, pages 91-93, (2012).
149. S. Yılmaz, E. McGlynn, E. Bacaksız, J. Cullen, R.K. Chellappan ,Structural,optical and magnetic properties of Ni-doped ZnO micro-rods grown by the spray pyrolysis method, Chemical Physics Letters,Volumes 525–526, 72-76, (2012).
150. C. LIU, F. YUN, H. MORKOC¸Ferromagnetism of ZnO and GaN: A review, journal of materials science: materials in electronics 16 (2005).
151. J W XU, H WANG, M H JIANG and X Y LIU , Properties of Nb-doped ZnO transparent conductive thin films deposited by rf magnetron sputtering using a high quality ceramic target, Indian Academy of Sciences 119-122 , (2010).
152. D. P. Joseph, Analysis of 3d transition elements doped ZnO, CuO and Cu-Zn-Se diluted magnetic semiconductors, Ph.D. thesis, University of Madras, Chennai, India, (2009).
153. D. P. Joseph, G. S. Kumar, and C. Venkateswaran, “Structural, magnetic and optical studies of Zn0.95Mn0.05O DMS,” Materials Letters, vol. 59, no. 21, pp. 2720–2724, (2005).